

PhD thesis

**Formation and properties of metastable
defects induced by pulsed laser irradiation
in hydrogenated amorphous Silicon**

Nikos Kopidakis

Physics Department
University of Crete

May 1998

Διδακτορική διατριβή

**Δημιουργία και ιδιότητες των μετασταθών
ατελειών στο άμορφο Υδρογονωμένο
Πυρίτιο: μελέτη με ισχυρό παλμικό laser**

Νίκος Κοπιδάκης

Φυσικό Τμήμα
Πανεπιστήμιο Κρήτης

Μάιος 1998

Ευχαριστίες

Θα ήθελα να ευχαριστήσω τον επιβλέποντα καθηγητή μου Πάνο Τζανετάκη για την πολύτιμη καθοδήγηση και βοήθεια στην διάρκεια της εργασίας αυτής.

Μεγάλη και πολύ σημαντική ήταν η συνεισφορά του καθηγητή Hellmut Fritzsche από το Πανεπιστήμιο του Σικάγου, με τον οποίο είχα την τύχη να συνεργαστώ αρκετές φορές στη διάρκεια των τεσσάρων χρόνων της δουλειάς αποκομίζοντας ανεκτίμητες γνώσεις και εμπειρίες σε πειραματικό αλλά και θεωρητικό επίπεδο. Θέλω να ευχαριστήσω την ομάδα Αμόρφων Ημιαγωγών του Πανεπιστημίου του Σικάγου και ιδιαίτερα τον Paul Stradins για τη συνεργασία και για τα δείγματα που μας παρείχαν.

Επίσης, ευχαριστώ τον Howard Branz για τις συζητήσεις και τις ιδέες που μου πρόσφερε και τους συναδέλφους στο εργαστήριο Μανόλη Στρατάκη, Μανόλη Σπανάκη και Μαρία Ανδρουλιδάκη για τη άψογη συνεργασία.

Μεγάλο μέρος των μετρήσεων πραγματοποιήθηκε στα εργαστήρια laser του ΙΤΕ. Θέλω να ευχαριστήσω την ομάδα των laser για τη φιλοξενία και τη βοήθειά τους, και ιδιαίτερα τους Δημήτρη Χαραλαμπίδη, Στέλιο Κουρή, Κώστα Μπάλα, Ναταλία Καραπαναγιώτη, Γιάννη Πετράκη, Αποστόλη Εγγλέζη τη Μαρία Τζατζαδάκη.

Από την ομάδα Μικροηλεκτρονικής του ΙΤΕ ευχαριστώ τον Ηλία Απεραθίτη και Γιώργο Κωνσταντινίδη για τη βοήθεια σε εναποθέσεις επαφών.

Τέλος, θέλω να ευχαριστήσω τους εργαζόμενους στο μηχανουργείο του ΙΤΕ και στην ομάδα κατασκευών, Γιώργο Παπαδάκη, Αργύρη Κασσωτάκη, Μάκη Κουτάντο, Μιχάλη Βισκαδουράκη, Μιχάλη Σμυρνάκη και Γιάννη Στρογγυλό.

Σημείωση: Όπως προανέφερα, σε όλη τη διάρκεια της δουλειάς υπήρξε στενή συνεργασία με τον καθηγητή Hellmut Fritzsche. Ήταν κατά συνέπεια σημαντικό το

να είναι εκείνος σε θέση να διαβάσει τη διατριβή αυτή. Για το λόγο αυτό η διατριβή γράφτηκε στα Αγγλικά.

Acknowledgments

During the four years of this work I had the great fortune of collaborating with prof. Hellmut Fritzsche of the University of Chicago, gaining invaluable experience in experimental research as well as in understanding of the physics of amorphous materials. I am grateful to him for his help and guidance. I also thank his group at the University of Chicago for the samples they provided and especially Paul Stradins for his assistance and cooperation.

I wish to thank Howard Branz from the National Renewable Energy Laboratory in Colorado, for many stimulating discussions and ideas during the four months he spent in the University of Crete.

Table of contents

Chapter 1. Introduction	1
1.1 Defects in amorphous solids.....	1
1.2 Density of states of Hydrogenated Amorphous Silicon	3
1.3 Photoconductivity in a-Si:H	7
1.4 Photocarrier recombination	9
1.5 Dependence of photoconductivity on temperature-Thermal quenching...11	
1.6 Experimental methods	14
Chapter 2. The Staebler-Wronski effect in a-Si:H	19
2.1 Introduction	19
2.2 Models for the SW effect	20
2.2.1. The SJT model	21
2.2.2 The H-collision model	23
2.3 Defect creation with laser pulses.....	26
2.3.1 Laser pulses versus CW illumination	26
2.3.2 The models of defect creation with laser pulses	27
2.4 Earlier work on pulse degradation	29
Chapter 3. Creation of light-induced defects with laser pulses	31
3.1 Introduction	31
3.2 Undoped samples	33
3.2.1 Light soaking at room temperature	33
3.2.2 Laser pulse light soaking at 77K	37
3.2.3 Annealing of metastable defects	38
3.3 Compensated samples	43
3.4 p-type sample	46
3.5 Discussion	49

Chapter 4. Photoconductivity under pulsed laser light	53
4.1 Introduction	53
4.2 Laser pulse photoconductivity during light degradation	55
4.3 Dependence of pulse photoconductivity on doping and light generation rate	59
4.4 Discussion	64
4.4.1 Universality of laser pulse photoconductivity	64
4.4.2 Recombination at very high photocarrier densities	65
4.4.3 Consequences of these experimental observations on defect creation models	67
4.4.4 Photoconductivity over a wide range of generation rates in a-Si:H	70
4.4.5 Energy dissipation under high photocarrier densities- an open problem	71
 Chapter 5. Space charge effects in photoconducting a-Si:H	73
5.1 Introduction	74
5.1.1 Photoconductivity in a-Si:H	74
5.1.2 Thermal and Infra-red quenching of photoconductivity.....	75
5.1.3 Metal-semiconductor transport	76
5.2 Appearance of space charge in photoconducting a-Si:H	78
5.2.1 Potential profile across the photocurrent path	78
5.2.2 Effect of space charge on the temperature dependence of photoconductivity	81
5.2.3 Origin of SC near cathode	84
5.3 Effects of cathode SC on the transport properties	86
5.3.1 I-V curves	86
5.3.2 Effects of IR illumination	88
5.3.3 Effects of space charge on photoconductivity at various light wavelengths	91
5.3.4 Light degradation effects	93
5.4 Modelling of space charge near the cathode	96
5.4.1 The model.....	96

5.4.2 Results of the model.....	98
5.4.3 Discussion.....	102

Appendix A: Sample characteristics.....	109
Appendix B: Photoconductivity during 30ns pulses: measurement set-up.....	111
Appendix C: Potential profile measurement set-up.....	113
References	117

Chapter 1. Introduction

1.1. Defects in amorphous solids

The difference between amorphous and crystalline solids is that the former exhibit long range order in the position of the atoms in the lattice, while in the latter the atoms are arranged in such a way that there is only short range order. This means that in both crystalline and amorphous Silicon (hereafter denoted c-Si and a-Si respectively), the atoms are 4-fold coordinated and the average bond lengths and bond angles in a-Si are the same as those of c-Si. However, in amorphous solids in contrast to the crystalline ones, as we move to second or further nearest neighbors, the correlation between the atomic positions disappears. A comparison between the ordered structure of crystalline material and the disordered structure of amorphous material is presented in two dimensions in Figure 1.1. The bonding arrangement in the crystalline material is the same in each atom, while disorder exists in the amorphous material.

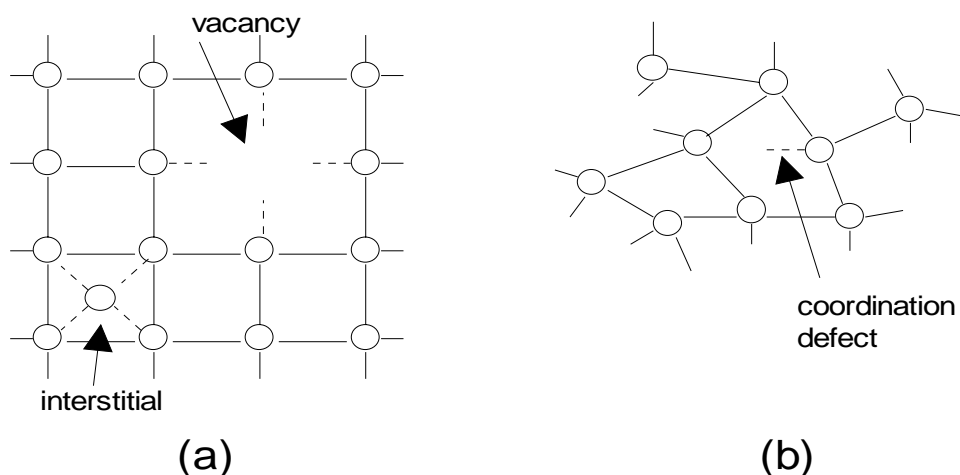


Figure 1.1. Defects in crystalline (a) and amorphous (b) solids.

The simplest defects in crystalline materials are vacancies and interstitials, shown in Fig.1.1a. In amorphous solids, the only specific feature of the lattice structure is the bonding configuration of an atom to its nearest neighbors. It has been shown that a random network with each atom to be four-fold coordinated, has very high internal stresses, which are relieved by the presence of three-fold coordinated atoms [Phillips, 1979]. This coordination defect, i.e. the Si dangling bond, is the dominant defect in a-Si, shown in Fig.1.1b. It has been proposed by Pantelides [Pantelides 1986] that the floating bond, i.e. 5-fold coordinated atom is also an important defect in the material.

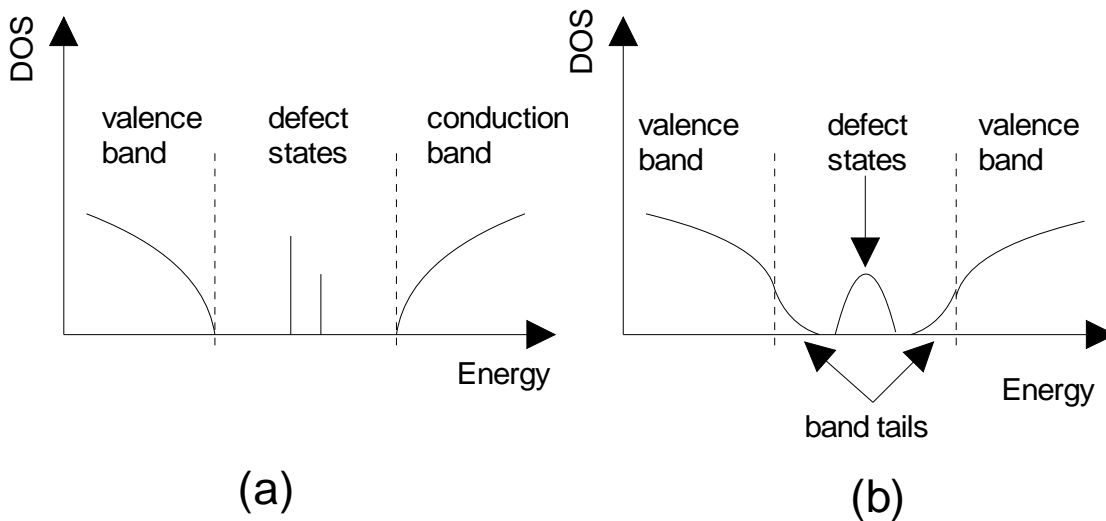


Figure 1.2. Comparison of the densities of states of c-Si (a) and a-Si (b).

In Figure 1.2 we compare the density of states (DOS) of amorphous and crystalline Si. The difference in the DOS can be understood in terms of the difference in structure, discussed above. The nearest neighbor bonding determines the gap between bonding states which form the valence band, and anti-bonding states which form the conduction band, in both crystalline and amorphous material. However, in amorphous materials there are no sharp band edges. The disorder in bond length and angles is responsible for the appearance of a continuous distribution of states, the conduction and valence band tails. The extended states in the valence and conduction bands are

separated from the localized states of the band tails by the respective mobility edges. The coordination defects in amorphous Silicon are represented by a distribution of states near midgap, see Fig.1.2b.

One should always keep in mind that in amorphous materials the band structure theory based on Bloch's theorem is not applicable, since there is no periodicity in the amorphous lattice. This means that the density of states in amorphous solids represents an average number of states over the disordered lattice and cannot be parametrised with inverse lattice vector \mathbf{k} .

1.2. Density of states of Hydrogenated Amorphous Silicon

The density of states of Hydrogenated Amorphous Silicon (a-Si:H) is shown in Fig.1.3. E_c and E_v denote the conduction and valence band mobility edges respectively, i.e. the energies which separate the bands from the band tails. The states in the band tails are localized, while those in the bands are extended. In a-Si the band tails can be described accurately with exponential functions. The slopes of the tails are different, reflecting the fact that the p-like states of the top of the valence band are influenced by disorder in Si-Si bond angles, more than the spherically symmetric s-like states of the bottom of the conduction band. The slopes of the exponential tails in high quality a-Si:H are about 25meV for the conduction band tail and 45meV for the valence band tail, see Fig.1.3.

The dangling bond states are represented with the distribution near midgap. In the first attempts for deposition of a-Si, with the sputtering technique, the produced material had a very high density of defects, 10^{18}cm^{-3} or higher. This material showed no

significant photoconductivity. The development of the plasma assisted CVD method, in which the film is deposited after glow discharge decomposition of Silane (SiH_4), led to Hydrogenated material. High quality Hydrogenated a-Si (a-Si:H) usually contains 8-10 at. % Hydrogen, which passivates dangling bonds, and reduces the defect density to $(1-5)\times 10^{15}\text{cm}^{-3}$. However, even with the incorporation of H, the defect density cannot be reduced to values lower than about 10^{15}cm^{-3} . Still, the reduction of dangling bond density made the Hydrogenated material highly photoconductive. This fact, together with the observation that a-Si:H can be effectively doped by incorporation of Boron or Phosphorous [Spear *et al.* 1975] was a critical step in the use of a-Si:H in device applications.

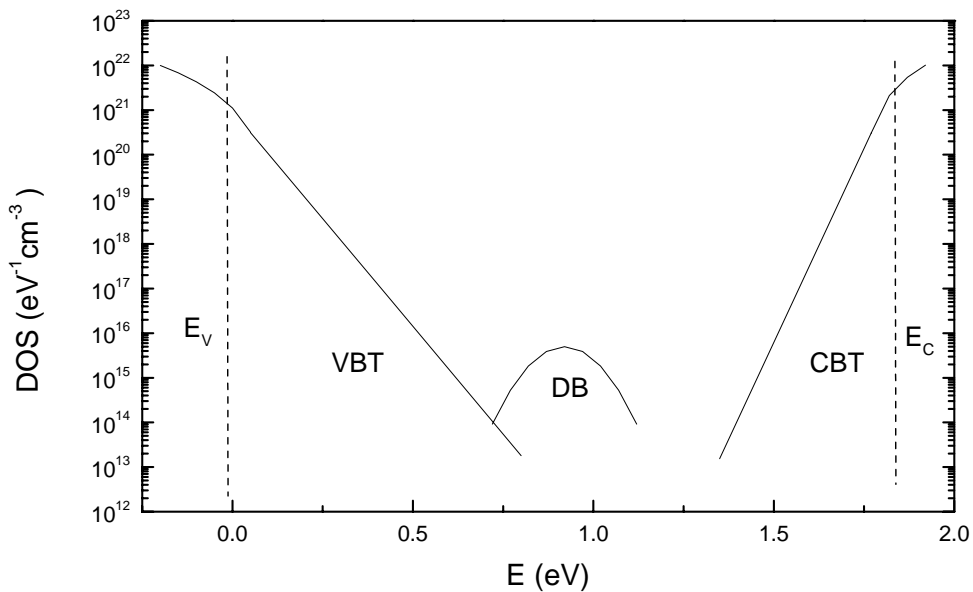
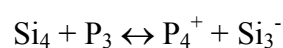


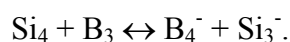
Figure 1.3. Density of states of a-Si:H. E_C and E_V denote the conduction and valence band edges, CBT and VBT are the Conduction and Valence band tails and DB is the dangling defect bond density. The vertical dashed lines indicate roughly the mobility edges, i.e. the separation between extended and localized states.

The doping mechanism in a-Si:H is very different than that in c-Si. As already mentioned, three fold coordinated atoms can be incorporated in the amorphous network. Thus, strictly speaking, substitutional doping of a-Si:H by P or B atoms is not possible, because these dopants can retain their preferred three-fold coordination when incorporated in the material. However, a small percentage of the incorporated dopants will have four-fold coordination, forced by their local surroundings in the amorphous lattice. Thus, doping can be achieved in a-Si:H but with small efficiency. An additional reason for the small doping efficiency in a-Si:H is the difficulty in shifting the Fermi level of the material, because of the presence of a significant density of states near midgap.

The large number of P or B atoms incorporated in the material, in order for significant effective doping to occur, causes two important effects. The first is that doped a-Si:H has higher native defect density than undoped material. The second effect is the presence of strong potential fluctuations in doped samples, which reduce the carrier mobility.

The increased defect density in doped a-Si:H can be understood as follows [Street, 1985]. As already mentioned, three fold coordinated atoms can be incorporated in the amorphous lattice. Thus, neutral P or B atoms can retain their preferred 3-fold coordination when incorporated in the material and hence will not be active dopants. However, P^+ and B^- are 4-fold coordinated and will act as dopants in a-Si:H. The charge state of the dopants is compensated by charged dangling bond states, according to the reactions





In the above reactions the subscript denotes the coordination number. Si_3^- is a three-fold coordinated Si atom, i.e. one dangling bond is created for each active dopant and thus the defect density in doped material is higher.

One of the most important effects observed in a-Si:H is the increase in defect density after prolonged exposure to bandgap light [Staebler *et al.* 1977]. One can reach defect densities as high as 10^{17}cm^{-3} by illuminating the sample, reducing accordingly the photocarrier lifetime and the photoconductivity, as will be discussed in Chapter 2. The effect is reversible, i.e. one can eliminate the defects induced by light, and reach the minimum defect density of the annealed sample. This is achieved by annealing the sample at sufficiently high temperature, usually around 190°C , for about 2h. This means that no permanent damage is done in the material.

The general topic of the work presented in this thesis is the creation of metastable defects by light in a-Si:H, usually called the Staebler-Wronski (SW) effect after the researchers who observed it first [Staebler *et al.* 1977], a phenomenon with serious consequences in all device applications of a-Si:H, and especially in solar cells. Despite the twenty years of research on the SW effect, it is still poorly understood [Fritzsche, 1997].

At this point it is helpful to introduce some terminology, which will be useful in later discussion. Prolonged, intense illumination of the sample in order to create defects is usually referred to as light soaking. The minimum defect density in the annealed sample is called native defect density, while the additional defects created by light are

called light-induced defects. The state of minimum defect density of the sample is usually called state A. The light-induced defects are metastable, meaning that one can eliminate them and bring the sample to state A, by annealing at high temperature. For this reason, state A is also called fully annealed state of the sample.

1.3. Photoconductivity in a-Si:H

All measurement techniques employed in this work are based on the photoconductivity of a-Si:H. In general the conductivity σ of a semiconductor can be written as

$$\sigma = e(n\mu_e + p\mu_h)$$

where n, p denote the free electron and free hole densities, and μ_e, μ_h is the electron and hole mobility. e is the absolute value of the electron charge.

In a-Si:H the extended state hole mobility is about one order of magnitude smaller than the electron mobility. Thus, in undoped a-Si:H electrons dominate the current transport.

In the dark, at room temperature, the conductivity of undoped a-Si:H is as low as 10^{-10} ($\Omega^{-1}\text{cm}^{-1}$). The Fermi level in the dark, usually called the dark-Fermi level, is located near the middle of the gap in undoped material. When the sample is illuminated with photons having energy larger than the band gap, electron-hole pairs are generated. Under steady state conditions, thermal equilibrium is established between free carriers in the bands and trapped carriers in the band tails. The occupancy of the tail states is determined by Fermi-like functions with chemical potential the so-called trap

quasi-Fermi level. The occupancy of the localized tail states lying in energy deeper than the trap quasi-Fermi level E_t , is less than one and drops rapidly around E_t .

The conduction mechanism in a-Si:H is strongly influenced by the presence of the tail states. Electron transport proceeds according to a multiple trapping mechanism in which a carrier gets trapped in shallow tail states and thermally re-emitted during transport, presented schematically in Fig.1.4.

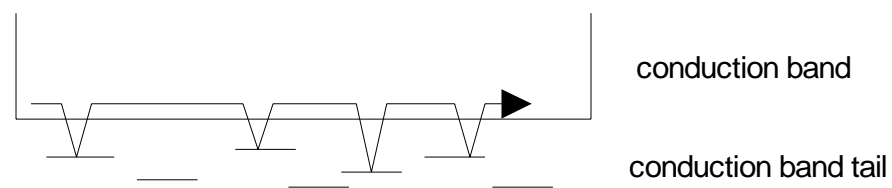


Figure 1.4. Multiple trapping mechanism of conduction in a-Si:H.

There are two alternative ways to describe the conduction in a-Si:H, according to the above discussion. The first is to use the free electron density, i.e. the electron density in the conduction band, with the respective free carrier mobility. The second is to use the total electron density, i.e. the density of electrons in the conduction band plus the density of electrons in the multiple trapping regime of the conduction band tail, with the respective drift carrier mobility. The multiple trapping regime can be understood as follows. The characteristic time for thermal emission of a carrier trapped in a tail state becomes longer as we move away from the respective band edge. Thus, a carrier trapped in a tail state near the conduction band edge will be re-emitted to the band, while a carrier trapped deep in the tail will remain there for a sufficiently long time for a carrier of opposite sign to be captured in the same state, resulting in the loss of

both carriers in a recombination event. Thus, the shallow tail states participate in the multiple-trapping mechanism, while deep tail states act as recombination centers.

The two equivalent ways of describing the photoconductivity, σ_p in a-Si:H can be written as follows:

$$\sigma_p = en_f \mu_0 = en_{tot} \mu_d .$$

In the above equation n_f is the free carrier density, i.e. the carrier density in the conduction band, and μ_0 is the free electron mobility. Alternatively, n_{tot} is the total electron density in the band and in the multiple trapping regime of the tail, and μ_d is

the, so-called, drift mobility, defined by $\mu_d = \mu_0 \frac{n_f}{n_{tot}}$.

1.4. Photocarrier recombination

Under steady state conditions, the photocarrier generation rate G is equal to the recombination rate R . Let us distinguish between two dominant recombination paths in a-Si:H.

- I. **Band-to-tail recombination.** In a-Si:H the densities of carriers trapped in the tails are higher than the densities of free carriers in the respective bands, i.e. $n > n_t$ and $p > p_t$, where n, p are the free electron and hole densities respectively and n_t, p_t the densities of trapped electrons in the conduction band tail and trapped holes in the valence band tail. Thus, if we neglect tunneling between localized states, the dominant terms in the recombination rate of free carriers and carriers trapped in the band tails will be np_t and pn_t . The drift mobility, i.e. the ratio of free to the total carrier density in a-Si:H (see §1.3), is roughly constant under reasonable light intensities, thus we have $n_t \propto n$ and $p_t \propto p$. The recombination rate in this

case is $R \propto np \propto n^2$. This means that $G \propto n^2$ and consequently $n \propto G^{1/2}$ and $\sigma_p \propto G^{1/2}$. This recombination path involves simultaneously two carriers, and is thus called “bimolecular” recombination. It is evident that when the quasi-Fermi levels lie closer to the band edges, which happens at high photocarrier generation rates, the energy released by bimolecular recombination will be higher.

II. **Recombination at defects**, i.e. trapping of a carrier at a defect state and subsequent trapping of a carrier of opposite sign in the same state, resulting in the loss of both carriers. Let us denote the defect density by N_D , and let us assume for simplicity that the defect states are not completely filled with electrons or not completely empty of electrons, and thus can capture carriers of either sign. In this case $G=R=c'nN_D$, i.e. $n \propto G/N_D$ and consequently $\sigma_p \propto G/N_D$. The electron lifetime τ can be defined in steady state as $G=n/\tau$. In the case of recombination at defects we see that $\tau \propto 1/N_D$. This is the simplest dependence of photoconductivity and of photocarrier lifetime on defect density. One expects that, when the defect density of the sample is increased by light soaking, the photoconductivity will drop in proportion, if one assumes dominant recombination at defects. This issue will be extensively discussed in Chapter 3. The recombination at defects is a two-step process, each step involving a single carrier, and is thus called “monomolecular” recombination. The occupation state –or in other words the charge state- of the defect states complicates the above picture of recombination at defects, as discussed in the next section.

In a-Si:H a relation $\sigma_p \propto G^\gamma$ holds, where the exponent γ depends on temperature and on the range of generation rates involved, as we will discuss in Chapter 4.

1.5. Dependence of photoconductivity on Temperature- Thermal Quenching

In this section we discuss the temperature dependence of the photoconductivity σ_p in a-Si:H. This provides some insight in the recombination of photocarriers at various temperatures T , and the role of occupation, i.e. charge state, of defects.

A typical $\sigma_p(T)$ curve of an undoped a-Si:H samples in state A is shown in Fig.1.5, from 77K to 400K. One striking feature of this curve is the decrease of σ_p with T at temperatures between 250K and 300K. This anomaly is called Thermal Quenching (TQ) of photoconductivity. As we will see, it is closely related to recombination through tail and defect states.

It was shown by Tran [Tran, 1995] that the form of the density of states of a-Si:H is the cause of TQ of photoconductivity. This is justified as follows [Tran, 1995]. The equation of charge neutrality in the material is

$$p-n+p_t-n_t+N_{D^+}-N_{D^-}=Q \quad (1.1)$$

where n, p denote the densities of free electrons and holes in the respective bands and n_t, p_t are the densities of trapped electrons in the conduction band tail (CBT) and holes in the valence band tail (VBT) respectively. N_{D^-}, N_{D^+} are the densities on negatively and positively charged dangling bond states. Q denotes the charge which results from ionization of donors in n-type samples ($Q < 0$) or acceptors in p-type samples ($Q > 0$).

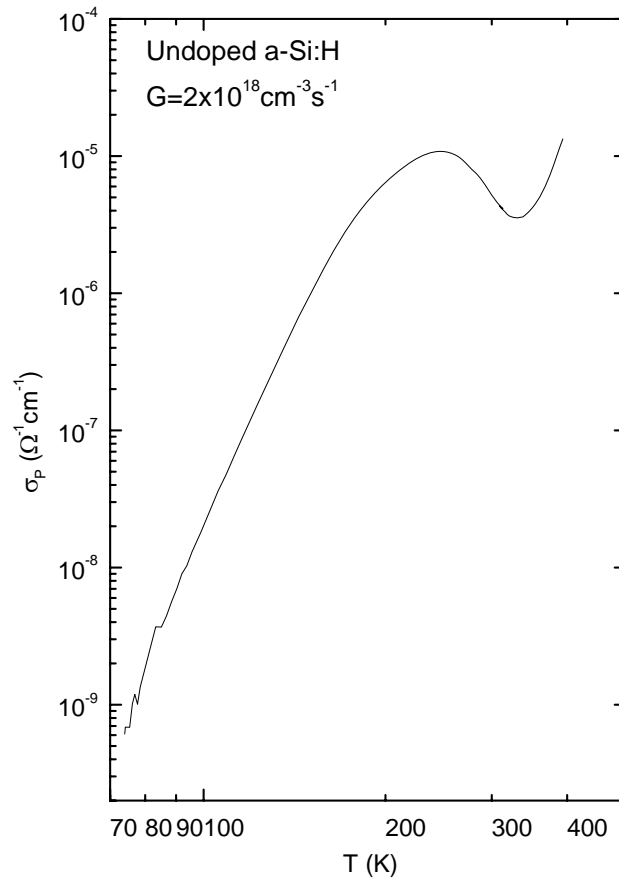


Figure 1.5. Photoconductivity versus temperature, of a high quality undoped a-Si:H sample in well annealed state, measured with photocarrier generation rate $G=2 \times 10^{18} \text{ cm}^{-3} \text{ s}^{-1}$.

Under illumination with bandgap light, steady state between trapped carriers in band tails and free carriers in the respective bands is established. Electrons and holes are generated by light in pairs, but more holes are captured in the wider VBT than electrons in the narrower CBT. This means that the free electron density will be higher than the free hole density, i.e. $n > p$. The higher electron density causes more electrons than holes to get captured by dangling bonds, and thus most dangling bonds will be filled with electrons, i.e. $N_D \gg N_{D^+}$.

Since the densities of trapped carriers are larger than the densities of free carriers, one can reduce equation (1.1) to

$$p_t \approx n_t + N_D + Q . \quad (1.2)$$

At low temperatures the quasi-Fermi level of holes E_{Fp} lies close to the valence band, and thus there is a high density of trapped holes relative to N_D at these temperatures. This suggests that the main recombination path for electrons at these temperatures will be the recombination of free electrons with trapped holes^{*}. This recombination rate R is written as

$$R = cnp_t .$$

In steady state at low temperatures, the rate G of generation of carriers by light equals the rate of recombination, if one neglects thermal re-emission. This means that

$$G = cnp_t , \quad (1.3)$$

taking into account only the dominant recombination path as mentioned above. Equation (1.3) suggests that the product np_t remains constant as long as recombination proceeds only through the VBT holes. The defect states can not act as recombination centers for electrons, because they are filled, i.e. most of them are negatively charged. This phenomenon of the presence of an alternative recombination path (realized here as the recombination through defects), which however is inactive, is in the case of a-Si:H the manifestation of a the more general effect called “sensitization” [Rose 1963].

The trapped carrier densities n_t and p_t decrease with increasing temperature T by thermal detrapping. This means that in eq. (1.3), as the temperature T increases, $n(T)$

^{*} One assumes that there is no tunneling between localized states, i.e. no direct recombination of trapped electrons with trapped holes. Only free-to-trapped carrier transitions are considered.

rises as fast as $p_t(T)$ decreases. This decrease of n_t and p_t can proceed up to the point where n_t becomes equal to N_D , in which case eq.(1.2) becomes

$$p_t = 2N_D + Q. \quad (1.4)$$

As T increases further, n_t continues to decrease, but now p_t must stay constant for charge neutrality, eq.(1.4), to be maintained. The dominant recombination path is still the one through VBT states, since the electrons cannot recombine through the negatively charged dangling bond states. This means that eq.(1.3) still holds, and thus n does no longer increase with T and remains constant, initiating TQ.

From eq.(1.4) one can see that the defect density N_D is the critical material parameter which determines the onset temperature of TQ in undoped samples where $Q=0$. When the defect density is increased, the onset of TQ is shifted to lower temperatures, as can be seen from eq.(1.4).

After TQ is initiated, the trapped hole density is equal to the defect density. The density of neutral and positive defect states is enhanced by thermal detrapping, and recombination through defects becomes important, causing the decrease in $\sigma_p(T)$. Now, the sample is said to be desensitized, because recombination at defects comes into play. Further increase in temperature enhances thermal free carrier generation. The conductivity rises with T above 400K, because the thermal carriers begin to dominate the current transport.

1.6. Experimental methods

Hydrogenated Amorphous Silicon is deposited in the form of a thin film on various substrates. The samples used in our study are about 1 μ m thick, deposited on Corning-

7059 glass substrates. NiCr and Cr metal contacts are evaporated on the free surface of the film, for conductivity measurements. The spacing between metal contacts was 0.2 to 2mm.

In order to measure photoconductivity, various light sources were employed. The bandgap light wavelength used was 650nm. This particular wavelength was chosen because the corresponding photon energy is 1.9eV, higher than the band gap, but still the absorption coefficient at this wavelength is of the order of 10^4cm^{-1} , low enough to ensure that the light is more or less uniformly absorbed in the $1\mu\text{m}$ thick sample, and not only in a thin surface layer.

The light source most commonly used in our measurements of steady state photoconductivity was Light Emitting Diodes (LED) at 650nm. The photocarrier generation rates achieved with this light were around $10^{18}\text{cm}^{-3}\text{s}^{-1}$.

For light soaking we have used nanosecond light pulses from an excimer-pumped dye laser at 650nm. The reasons for using pulsed light for sample degradation will be discussed in Chapter 2. In Chapter 3 we present results of laser pulse degradation of undoped, compensated and p-type a-Si:H samples. In Chapter 4 we present results on the photoconductivity induced in the sample by the laser pulse, in nanosecond time scale.

In order to measure the increase of defect density during light soaking, the Constant Photocurrent Method (CPM) was employed. This method is based on the relation $\sigma_p \propto G'$. When the sample is illuminated with monochromatic light, for uniform

absorption, i.e. $\alpha d \ll 1$, one has $G = \alpha F$, where α is the absorption coefficient at the wavelength of incident light, d is the sample thickness, and F is the photon flux. The main assumption of CPM is that the exponent γ is independent of wavelength. Thus, if we choose two different wavelengths λ_1 and λ_2 , and adjust the corresponding fluxes in order to have the same photoconductivity under illumination with either wavelength, we have $\frac{\alpha(\lambda_1)}{\alpha(\lambda_2)} = \frac{F(\lambda_2)}{F(\lambda_1)}$. This relation allows one to measure the photon fluxes and deduce the ratio of absorption coefficients.

At this point it is useful to give the dependence of absorption coefficient in a-Si:H, as a function of photon energy, Figure 1.6. We see that if we allow λ_1 to be broadband infra-red light at photon energies lower than 1.44 eV, we average over the whole defect absorption band. We denote this infra-red light as IR. We then choose λ_2 to be 650nm, and thus have $\frac{\alpha(IR)}{\alpha(650nm)} = \frac{F(650nm)}{F(IR)}$. If we keep the IR flux constant and vary the 650nm flux to achieve the constant photocurrent, in which the above relation is based, we finally get $\alpha(IR) \propto F(650nm)$. With the last relation we can measure the increase in subgap absorption during a light soaking experiment. We set a constant IR flux at wavelengths $\lambda \geq 850nm$, and measure the photocurrent induced in the sample by this light, when the sample is in state A. We then adjust the flux of the 650nm LED light in order to get the same photocurrent as that with IR light. After some increase in defect density by light soaking, when the sample is in some other state B, we measure again the photocurrent induced by the IR light, and again adjust the LED light flux to get the same photocurrent as with the IR in this state B. The ratio of the absorption coefficients in the two states of the sample, $\frac{\alpha_B(IR)}{\alpha_A(IR)}$ is equal to the ratio of

the fluxes of the 650nm light in each case, which can be easily determined by measuring the current through the LED which emits the 650nm light. This way, we measure the absorption, relative to state A of minimum defect density. The subgap absorption coefficient at the wavelengths of the particular IR light chosen, corresponds to absorption of light from defect states (as shown in fig.1.6) and is thus proportional to the density of defect states in the gap of the semiconductor.

An important point to be emphasized here is that CPM is applicable at room temperature and at very low temperatures (liquid Helium, 4.2K), but is not applicable at liquid Nitrogen temperature, 77K [Stradins *et al.* 1995].

The effect of metastable defect creation in a-Si:H by intense illumination is discussed in more detail in the next Chapter.

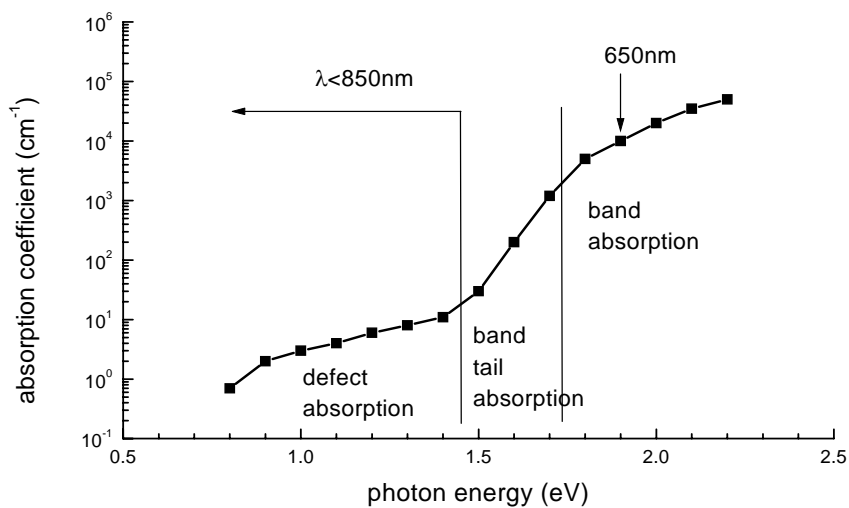


Figure 1.6. Absorption coefficient of a-Si:H, versus photon energy. The range of photon energies used in our CPM measurements is shown.

Chapter 2: The Staebler-Wronski effect in a-Si:H

2.1. Introduction

As discussed briefly in the previous Chapter, the defect density in a-Si:H is increased, when the material is illuminated with intense bandgap light. The first observation by Staebler and Wronski [Staebler and Wronski 1977], was that both the photoconductivity and the dark conductivity of a-Si:H samples decrease after exposure of the sample to intense illumination with bandgap light. The effect was attributed to an increase in the density of gap states, which act as recombination centers. Staebler and Wronski concluded that these light-induced states shift the dark Fermi level towards midgap, thus decreasing the dark conductivity, and act as recombination centers, thus decreasing the photocarrier lifetime and the photoconductivity. The light-induced effects are metastable, and the state of the sample before illumination can be reached by annealing at high temperatures ($\geq 150^{\circ}\text{C}$) for 2h.

Subsequent studies, employing various experimental techniques, CPM, Electron Spin Resonance, (ESR) or Photothermal Deflection Spectroscopy (PDS), showed that, under intense illumination, the dangling bond defect density increases, reaching saturation at a value that can be as high as two orders of magnitude higher than the native defect density. The increase in defect density, and thus in the concentration of recombination centers, decreases the photoconductivity and degrades the performance of devices based on a-Si:H.

Excess defect concentration in a-Si:H can also be created by charge injection [den Boer *et al.* 1984, Pfeleiderer *et al.* 1984], or by bombardment with keV electrons [Wagner *et al.* 1987]. In all cases, the state of the sample after degradation is metastable, and state A of minimum defect density is achieved after annealing at sufficiently high temperature.

The creation of excess defect density is an effect intrinsic to a-Si:H, and is not related to impurities in the material [Stutzmann *et al.* 1985, Kamei *et al.* 1996], as was previously suggested. Kamei *et al.* succeeded in creating by light two orders of magnitude higher defect density than the density of C,N and O impurities in very high purity a-Si:H.

Before proceeding to the presentation in Chapters 3 and 4, of our study of Light-Induced-Defects (LIDs) creation with intense pulsed laser irradiation in undoped and doped a-Si:H, it is helpful to review the existing models for the creation of Staebler-Wronski (SW) defects by intense illumination. For simplicity we first present the models for defect creation with Continuous Wave (CW) illumination. We then show how the effect can be accelerated by using short, intense laser pulses, and how the models are modified to account for pulsed illumination.

2.2. Models for the SWE

Several models for the explanation of the Staebler-Wronski effect (SWE) have been proposed. These make specific predictions regarding the time evolution of defect creation in a-Si:H. Our study of the SWE is focused on two subjects: a) the kinetics, i.e. the time evolution, of light degradation, b) the recombination of photocarriers

after light soaking. As we shall see in the models presented in the next paragraphs, recombination of photocarriers is central to the SWE.

One of the basic experimental findings concerning the kinetics of the SWE, is that under illumination with CW light the defect density N_D increases with time t as $N_D(t) \propto G^{0.6} t^{0.3}$ [Stutzmann *et al.* 1985], G being the photocarrier generation rate of the soaking light. We will present two models, which account for this power law dependence, but are based in very different assumptions on the microscopic origin of the light-induced defect creation. These models will be further discussed in Chapters 3 and 4 in connection to our experimental findings.

2.2.1. The SJT model: A widely accepted model of the SWE is the model proposed by Stutzmann, Jackson and Tsai [Stutzmann *et al.* 1985]. We will hereafter refer to it as the SJT model.

There are two main assumptions in this model:

1. The lifetime of photocarriers generated by the soaking light is determined by recombination through defect states, i.e. monomolecular recombination.
2. Excess defect creation is driven by band-to-band, i.e. bimolecular, recombination, which releases enough energy to break weak Si-Si bonds and create dangling bonds. This bimolecular recombination path is present although the dominant recombination channel is the one through defects, as stated in assumption 1.

According to our discussion of §1.4, under steady-state illumination with generation rate G , if the dominant recombination path is that through defects, the electron and hole concentrations will be proportional to

$$n \propto p \propto G/N_D \quad (2.1)$$

where N_D is the defect density. The first assumption of the SJT model, stated above, is formally written as

$$\frac{dN_D}{dt} = c_{SW}np, \quad (2.2)$$

where t is the illumination time and c_{SW} a constant which determines the efficiency of defect creation via bimolecular recombination. Substituting the photocarrier densities from eq.(2.1) in eq.(2.2), we get for the rate of defect creation

$$\frac{dN_D}{dt} \propto \frac{G^2}{N_D^2},$$

which can be solved to give

$$N_D(t)^3 - N_D(0)^3 \propto G^2 t.$$

For sufficiently long illumination, in which $N_D(t) \gg N_D(0)$, the last equation is simplified to

$$N_D(t) \propto G^{2/3} t^{1/3} \quad (2.3).$$

Equation (2.3) is the prediction of the SJT model for the time evolution of defect density under CW illumination in a-Si:H, which is in agreement to experimental observations [Stutzmann *et al.* 1985] on the kinetics of the SW effect. The SJT model was the first model to account for the observed time evolution of light-induced defect creation.

At this point, we must note that the rate of defect creation decreases with time. This is due to the fact that the increase in defect density causes a decrease in photocarrier

lifetime, and consequently a decrease in photocarrier densities, which in turn causes a decrease in the rate of defect creation, see eq.(2.2).

According to the SJT model, the microscopic mechanism of the creation of an additional dangling bond by breaking a weak Si-Si bond is shown in Fig.2.1. The weak bond is presented by the dashed line. The energy released by a bimolecular recombination event, which takes place in the neighborhood of the weak bond, causes the breaking of this bond in two dangling bonds. After breaking, the bond is prevented from recombining, by a Hydrogen atom, as shown in Fig.2.1. Hydrogen is not involved in the rate equations presented above, but is needed in order to stabilize the two newly formed dangling bonds, and prevent them from reforming the Si-Si bond.

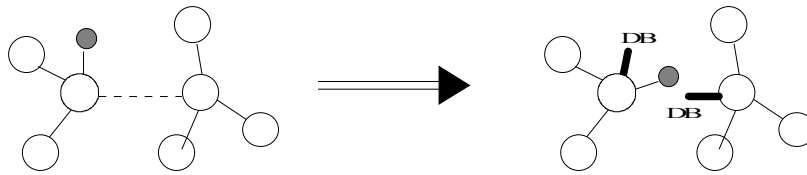


Figure 2.1. The microscopic mechanism of the SW effect in the SJT model: breaking of weak Si-Si bond (indicated by the dashed line) and stabilization of the DBs created. The H atom is presented as a gray sphere.

2.2.2. H-collision model: The H-collision model [Branz, 1997] assumes that H atoms are excited from Si-H bonds to a mobile state. This excitation, which leaves behind a dangling bond (DB), is driven by photocarrier recombination. The mobile state of H can be viewed as a Si-H/DB complex, as shown in Fig.2.2. This complex travels through the material, its diffusion being enhanced by photocarrier recombination. When this complex meets a DB, the two DBs recombine, the H atom is immobilized in the Si-H bond. This series of processes does not result in net creation of new DBs.

However, when two mobile Si-H/DB complexes meet, the DBs annihilate forming a Si-Si bond, the H atoms are again immobilized in Si-H bonds, but now two DBs are left behind in the bonds from which H was excited.

The main *ansatz* of the H-collision model is that the creation rate R_m of mobile-H density N_m , from a H-density in the sample N_H is

$$R_m = k_H N_H G$$

where G is the generation rate, and k_H is a proportionality constant.

The rate equation for creation and loss of mobile-H concentration is

$$\frac{dN_m}{dt} = k_H N_H G - k_{db} N_m N_D - 2k_c N_m^2 \quad (2.4).$$

The first term represents mobile-H creation as mentioned above, the second term represents loss of mobile-H when the Si-H/DB complex meets a DB, and the third term loss of mobile-H by collision of two Si-H/DB complexes. In the above equation N_D stands for the dangling bond density. Under CW illumination, steady state of N_m is reached, i.e. $dN_m/dt=0$. At the low H excitation limit, the density of dangling bonds is higher than the density of mobile-H, thus the dominant process for loss of mobile-H is that through an isolated DB and not the collision of two complexes, i.e. $2k_c N_m \ll k_{db} N_D$. For more details see Branz, 1997.

Equation (2.4) can now be simplified to

$$N_m = \frac{k_H N_H G}{k_{db} N_D} \quad (2.5).$$

As discussed above, net DB density is created when two mobile-H collide, i.e. the rate of creation of light-induced DBs, within the framework of this model, is

$$\frac{dN_D}{dt} \propto N_m^2 \quad (2.6).$$

Substituting (2.5) in (2.6) and solving gives again $N_D(t) \propto G^{2/3} t^{1/3}$, as in the SJT model.

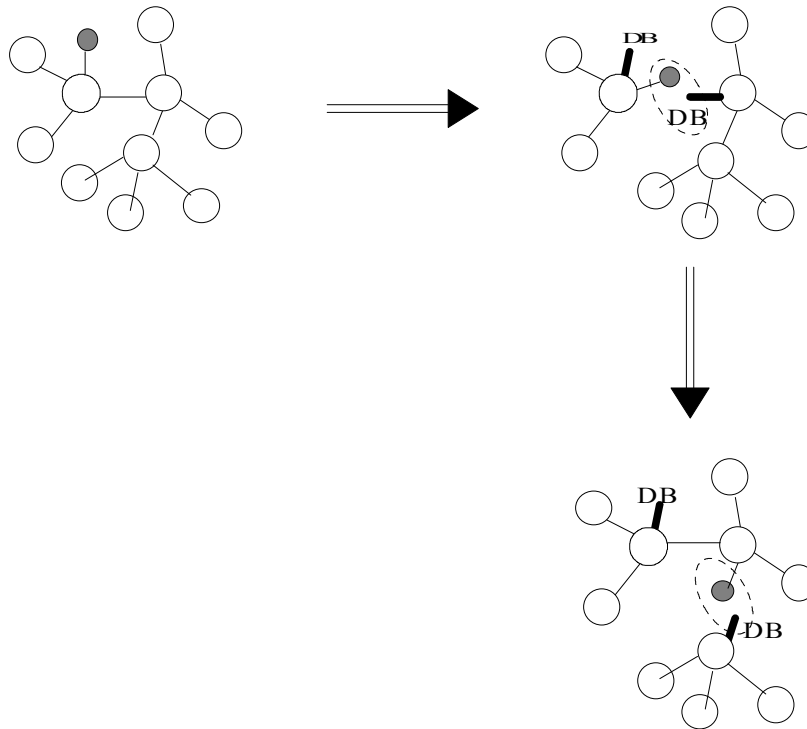


Figure 2.2. The mechanism of transfer of the Si-H/DB complex, which originated from a Si-H bond, in the H-collision model. The H atom is represented by a gray sphere.

As one can see from eqs.(2.5) and (2.6), the rate of creation of light-induced DBs is again decreased as the DB density increases, but now for a reason different than that in the SJT model. In the Branz model, it is the mobile-H density and not the photocarrier density that determines the rate of defect creation,. In the H-collision model the recombination of photocarriers is responsible for excitation of H atoms in the mobile state, and also for the enhancement of diffusion of the mobile-H in the material. In the H-collision model, the photocarrier lifetime is not crucial to the rate of light-induced defect creation, as in the SJT model.

2.3. Defect creation with laser pulses

2.3.1. Laser pulses versus CW illumination:

Within the framework of the bond-breaking (SJT) model presented in section 2.2.1, the rate of LID creation with CW light appears to be proportional to the bimolecular recombination rate, i.e. $\frac{dN_D}{dt} \propto np \propto n^2$. This non-linear dependence suggests that the kinetics of the SWE will drastically change with a change of photocarrier density, n .

Light soaking with continuous light cannot be performed with very high light intensity because the sample gets heated by the soaking light. Thus, there is an upper limit to the photocarrier densities achieved during CW light degradation. Typical values of light intensities in experiments of intense CW light soaking are around 0.5 W/cm².

The use of short, intense laser pulses allows one to overcome the heating problems and reach high photocarrier generation rates, and thus high photocarrier densities, during the laser pulse. This will alter the kinetics of the SWE, not only because of non-linear dependence of defect creation on photocarrier density, but also because at such high photocarrier densities the quasi-Fermi levels are shifted much closer to the respective bands and consequently higher energy is released from the recombination of a carrier in an extended state with a carrier of opposite sign in the tail. Furthermore, a state in the tail close to the respective band represents a stronger bond than a state deep in the tail. Thus, recombination at stronger bonds occurs under high photocarrier densities, which might also result in the breaking, under intense laser light, of bonds not as weak as in the CW illumination case.

The use of laser pulses has made possible our study of recombination at very high photocarrier densities. Our experiments did not validate the SJT model and provided the basis for a very good understanding of recombination in a-Si:H in a generation rate range of more than 10 orders of magnitude, as presented in Chapter 4 of this thesis.

Stutzmann *et al.* were the first to perform light soaking with intense laser pulses instead of continuous light [Stutzmann *et al.* 1991]. The use of laser pulses was observed to accelerate the effect, altering the time evolution to $N_D(t) \propto G^1 t^{0.5}$, where t is the illumination time and G the photocarrier generation rate during the light pulse.

In the next section we show how the SJT and H-collision models are modified to account for short pulse irradiation.

2.3.2. The models of defect creation with laser pulses

SJT model: The two assumptions of the SJT model remain the same also in the case of laser pulse soaking. This means that within the framework of the SJT model, one assumes that a (high) photocarrier density is created by the laser pulse, and the decay of this density after the end of the pulse is determined by recombination at defects, i.e. monomolecular recombination. This means that the decay time τ of the photocarrier density after the pulse will be inversely proportional to the defect density, $\tau \propto 1/N_D$. The photocarrier lifetime τ is assumed to be much larger than the pulse duration τ_{pulse} .

Still, a small percentage of the recombination traffic is bimolecular, i.e. recombination of a carrier in a band with a carrier of opposite sign in the band tail.

This recombination path is again assumed to be responsible for defect creation, i.e.

$$\frac{dN_D}{dt} \propto n^2$$

where n is the photocarrier density, as in the case of CW illumination.

Under these assumptions, a photocarrier density $n(0)=G\tau_{\text{pulse}}$ is created during the pulse, which decays after the light pulse is over as $n(t)=n(0)e^{-t/\tau}$. One assumes that the time between pulses is long enough that the photocarrier density will have completely decayed, before the next light pulse. The average bimolecular recombination rate during the decay of the photocarrier density is proportional to

$$\int_0^{\infty} [n(t)]^2 dt = [n(0)]^2 \frac{\tau}{2} \propto \frac{G^2}{N_D}.$$

The rate of defect creation is proportional to the bimolecular recombination rate, i.e.

$$\frac{dN_D}{dt} \propto \frac{G^2}{N_D}.$$

Solving the last equation gives, for sufficiently long times t ,

$$N_D(t) \propto Gt^{1/2},$$

in agreement with experimental observations [Stutzmann *et al.* 1991].

It must be noted that a crucial assumption of the model is that the photocarrier density decays after the end of the laser pulse, and the decay time, i.e. the lifetime, is determined by monomolecular recombination through defects. This lifetime is assumed to be of the order $\tau \approx 10^{-6}$ s. The creation of LIDs in the SJT model, occurs during the photocarrier decay.

H-collision model: The H-collision model can also account for the kinetics of defect creation with short laser pulses. The central idea of mobile-H, created by the photocarrier recombination remains the same. This mobile-H density is created during the laser pulse, and decays after the pulse is over, creating DBs, exactly as in the CW illumination case. In the same manner as in equation (2.5), the decay time τ_r of the mobile-H density is $\tau_r \propto 1/N_D$. If one assumes, as in the CW case, that the rate of creation of mobile-H density N_m by light is proportional to G , one gets a time dependence of mobile-H density to be proportional to $G \exp\left(-\frac{t}{\tau_r}\right)$. As in the CW case, the rate of defect creation is proportional to the square of the mobile-H density. This leads exactly to the same algebra as in the SJT model for pulses, resulting on the observed time dependence of defect density. However, as already mentioned, the H-collision model is not based on specific assumptions on the dominant photocarrier recombination path and photocarrier lifetime. In the H-collision model, the decay of mobile-H concentration after the pulse is responsible for LID creation. The decay of photocarrier density is not directly related to the SWE, according to this model.

2.4. Earlier work on laser pulse degradation

Earlier work on degradation of a-Si:H with laser pulses [Stutzmann *et al.* 1991], [Hata *et al.* 1992, 1993], [Meaudre *et al.* 1993] had indeed shown the usefulness of laser pulses for the study of the SWE.

Stutzmann *et al.* [Stutzmann *et al.* 1991] observed a time evolution $N_D(t) \propto t^{0.55}$, by measuring the photoconductivity at various stages of light soaking, i.e. at various t , and assuming $\sigma_p \propto 1/N_D$.

Hata *et al.* and Meaudre *et al.* observed saturation of defect density after light soaking with 10^4 laser pulses. Meaudre *et al.* observed that the saturation value of the defect density increases in proportion to the laser intensity used for light soaking.

All the above experiments were performed at room temperature.

Earlier work in the SWE with laser pulses did not include systematic comparison of laser pulse and CW light soaking in undoped and doped samples. Furthermore, there was no experimental test of the validity of many important assumptions related to the models for the SWE, presented in this Chapter. In the next Chapters we deal with some of these open problems related to defect creation.

Chapter 3. Creation of light induced defects with laser pulses

3.1. Introduction

In this Chapter we present our study of the kinetics of creation of Light-Induced-Defects (LID) with laser pulses, in undoped and doped a-Si:H samples. For each sample we compare the degradation with laser pulses of wavelength 650nm, to that under continuous light (CW) illumination of the same wavelength. The CW degradation data presented in this Chapter were taken in the laboratory of prof. H.Fritzsche in the University of Chicago.

Before each degradation run, the sample was annealed at 460K in the cryostat, in order to establish state A of minimum defect density.

During degradation the steady state photoconductivity, σ_p , was measured under illumination from an LED at 650nm. The photocarrier generation rate G of the LED light used was around $10^{18} \text{ cm}^{-3}\text{s}^{-1}$, orders of magnitude lower than the generation rate of the laser pulse. Hereafter the photoconductivity measured with low- G light will be referred to as low-light photoconductivity. Of course, during a low-light photoconductivity measurement the laser beam was switched off.

The subgap absorption at wavelengths $\lambda \geq 850\text{nm}$ was also measured, during degradation at room temperature, by the Constant Photocurrent Method (CPM), as described in §1.6. The subgap absorption coefficient α is proportional to the defect density of the sample, and is measured relative to the absorption α_0 in the annealed state. The *relative change* in subgap absorption $\frac{\Delta\alpha}{\alpha_0} = \frac{\alpha - \alpha_0}{\alpha_0}$ is proportional to the

light induced (and not the total) defect density. Subgap absorption coefficient was only measured at room temperature, because CPM cannot be applied at liquid Nitrogen temperature, 77K, as stated in §1.6.

The laser pulses used for sample degradation came from an Excimer-pumped dye laser. The dye solution used was Rhodamin 101 and the resonance cavity of the dye laser was tuned at 650nm. The pulse duration was 17ns or 30ns, depending on the specific laser used, and the pulse repetition rate did not exceed 14 Hz. The maximum laser fluence used for light soaking was $6 \text{ mJ/cm}^2/\text{pulse}$, in order to avoid significant increase in sample temperature due to the absorbed light. Lower intensities were attained by attenuating the laser beam with a series of neutral density filters, calibrated at the wavelength of the laser light, 650nm.

Each degradation run included 10^5 pulses of constant intensity. Hereafter it will be convenient to refer to a sample irradiated with 10^5 pulses as fully degraded.

After degradation, the temperature dependence of low light photoconductivity σ_p was measured. This measurement gives a more complete picture of the dependence of σ_p on the defect density present in the sample, as discussed in §1.5.

In all degradation measurements, no permanent damage was induced by the soaking light and the sample could always be brought to state A of minimum defect density after annealing at 460K for 30min.

3.2. Undoped samples

In this section we present the results of photodegradation of undoped sample i1, at room temperature and at liquid Nitrogen temperature, 77K. The sample characteristics can be found in Appendix A.

3.2.1. Light soaking at room temperature: Photodegradation with laser pulses in sample i1 at room temperature is shown in Fig.3.1. In this Figure the low light photoconductivity is plotted, during irradiation with laser pulses of three different fluences. The low light generation rate was $G=2 \times 10^{18} \text{ cm}^{-3} \text{ s}^{-1}$.

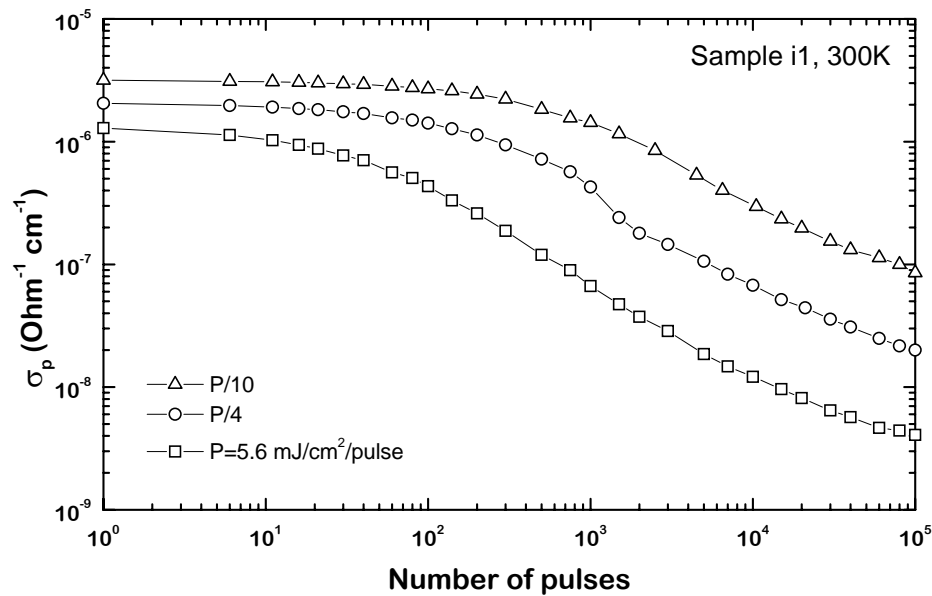
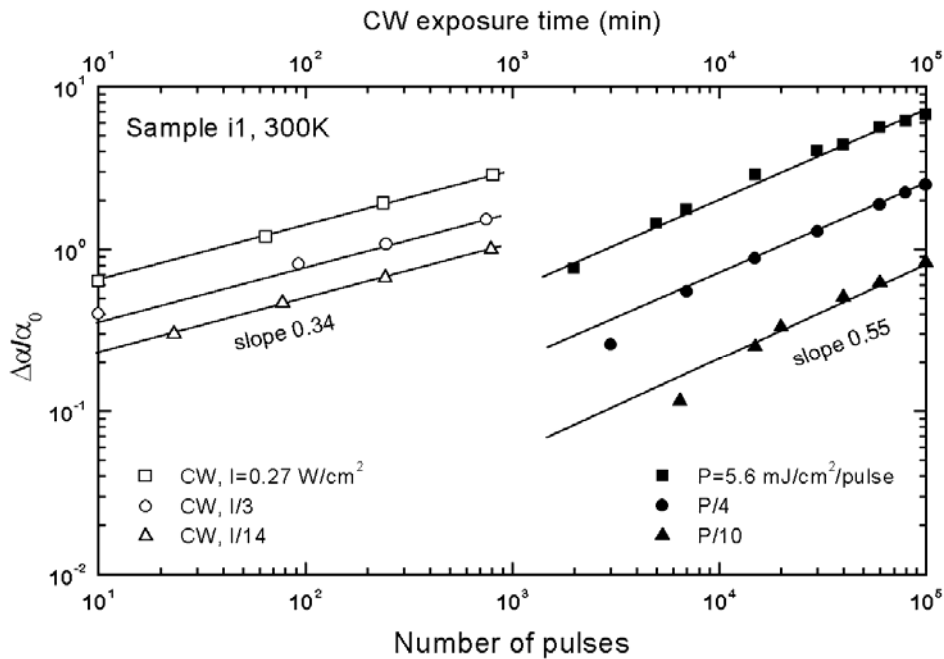


Figure 3.1. Low-light photoconductivity σ_p of undoped sample i1, during degradation with laser pulses at 300K. The generation rate of the low light was $G=1.8 \times 10^{18} \text{ cm}^{-3} \text{ s}^{-1}$. The laser pulse fluence P for each degradation run is shown in the graph. Solid lines are drawn as guide to the eye.

The photoconductivity of the sample in the beginning of each degradation run was not precisely identical for all runs. The reason is that after degradation, we could only anneal the sample in situ at 460K for short time, which was insufficient to completely



restore the photoconductivity to its value in the fully annealed state. However, as one can see in Fig.3.1, this is a minor effect compared to the light-induced changes with laser degradation.

Figure 3.2. Relative change in subgap absorption for sample i1 during laser degradation (solid symbols, bottom axis) and during CW degradation (open symbols, top axis), both at 300K. The lines indicate the slope.

The corresponding relative change in subgap absorption of sample i1 during irradiation at room temperature with the three laser intensities is shown in Fig.3.2. Open symbols represent CW light soaking of the same sample at room temperature, performed by the Chicago group. The points for laser pulse light soaking are plotted

against the Number of pulses, bottom axis of Fig.3.2, while the points for CW light soaking are plotted against light soaking time, top axis in Fig.3.2. The top and bottom axes should only have the same ratio of initial and final value, for comparison of the corresponding measurements. The relative position of the top and bottom axis is arbitrary.

The relative change in subgap absorption for laser pulse light soaking follows a

relation $\frac{\Delta\alpha}{\alpha_0} \propto P^1 N^{0.55}$, where P is the laser pulse power and N the number of pulses,

which is proportional to soaking time. We find that the last relation holds even for small values of $\Delta\alpha/\alpha_0$. Under CW illumination, the time evolution shown in Fig.2 is

$\frac{\Delta\alpha}{\alpha_0} \propto P^{0.4} t^{0.34}$. These relations for the time evolution of relative change in subgap

absorption, and hence of relative change in defect density, during light soaking, both CW and pulsed, are the same as those deduced by the SJT model of §2.2.1 and the H-collision model of §2.2.2. However, the relations deduced by the models of §2.2 hold only for $N_D(t) \gg N_D(0)$, i.e. $\Delta\alpha/\alpha_0 \gg 1$, whereas our measurements of $\Delta\alpha/\alpha_0$ follow the predicted time evolution even for small $\Delta\alpha/\alpha_0$, Fig.3.2.

Saturation of photoconductivity or defect density was not reached after 10^5 pulses in sample i1 at room temperature. This finding disagrees with previous measurements on undoped samples [Hata *et al.* 1992, 1993], [Meaudre *et al.* 1993]. Meaudre *et al.* and Hata *et al.* observed saturation of defect density after 10^4 laser pulses at room temperature. However, they measured very few CPM points during degradation, which makes their argument subject to experimental errors.

The low light photoconductivity plotted as a function of subgap absorption, during pulsed and CW light soaking, is shown in Fig.3.3. The points for the three laser pulse fluences show the same behavior in the region in which they overlap. The measurements for CW light soaking follow similar dependence, but lie at higher photoconductivity values, most probably because of calibration errors between the two laboratories.

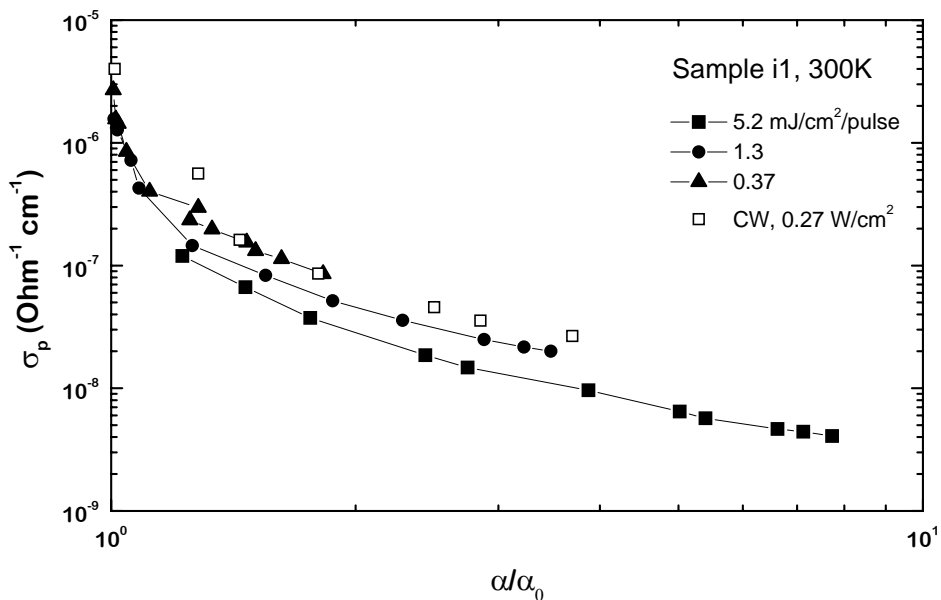


Figure 3.3. Low-light photoconductivity as a function of subgap absorption during degradation with laser pulses (solid symbols) and CW light (open symbols), both at 300K. The lines are plotted as guide to the eye.

One can see that the photoconductivity does not follow the $\sigma_p \propto \frac{1}{N_D}$ relation (see §1.4). An increase in subgap absorption, indicating a corresponding increase in sample defect density, by a factor 7 causes a drop in σ_p by more than two orders of magnitude.

In Fig.3.4 we plot the low light photoconductivity during light soaking as a function of the relative change in subgap absorption, $\Delta\alpha/\alpha_0$, which is proportional to the light induced defect density and not the total defect density. It is surprising to find that the photoconductivity appears to be inversely proportional to the *light induced* defect density rather than to the total defect density.

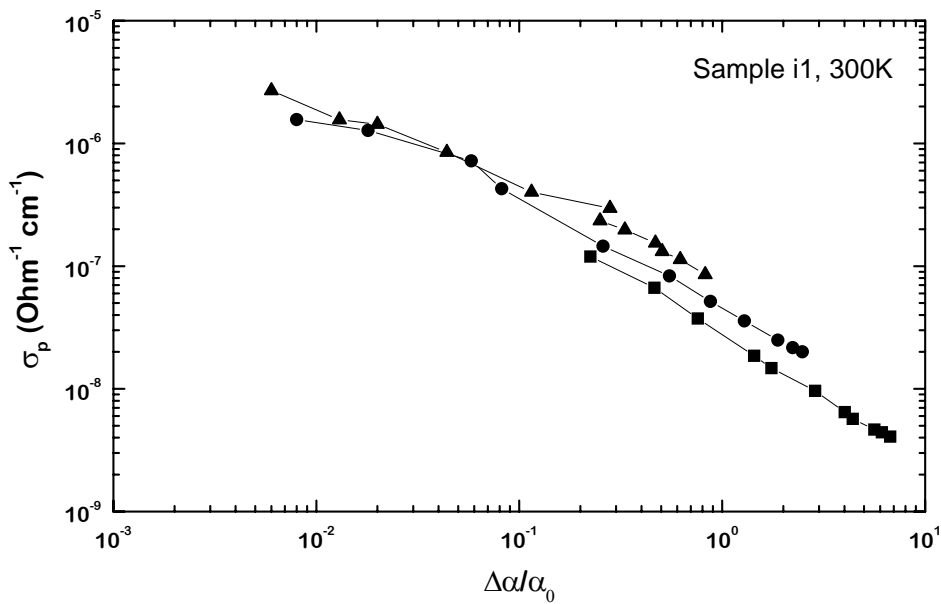


Figure 3.4. Same data as that for pulse degradation in Fig.3.3, plotted as a function of the relative change in subgap absorption

In section 2.2 we discussed that a crucial assumption of the SJT model is that the photocarrier lifetime, and hence the photoconductivity, is inversely proportional to the defect density. We find that the assumption on the dependence of lifetime on the total defect density is not correct. We will discuss this issue further in a following section.

3.2.2. Laser pulse light soaking at 77K: Degradation with laser pulses at liquid

Nitrogen temperature, studied for the first time, is presented here for sample i1.

Sample degradation was only monitored by measuring the low light

photoconductivity at the soaking temperature, 77K, since, as was stated in §1.6, the constant photocurrent method for determining subgap absorption is not valid at 77K. The low light photoconductivity of sample i1 at 77K during light soaking with laser pulses is shown in Fig.3.5.

In order to compare degradation at high (300K) and low (77K) temperature, we compare the dependence of low light photoconductivity on temperature T for states of the sample degraded at high and low T. This is done in the next paragraph.

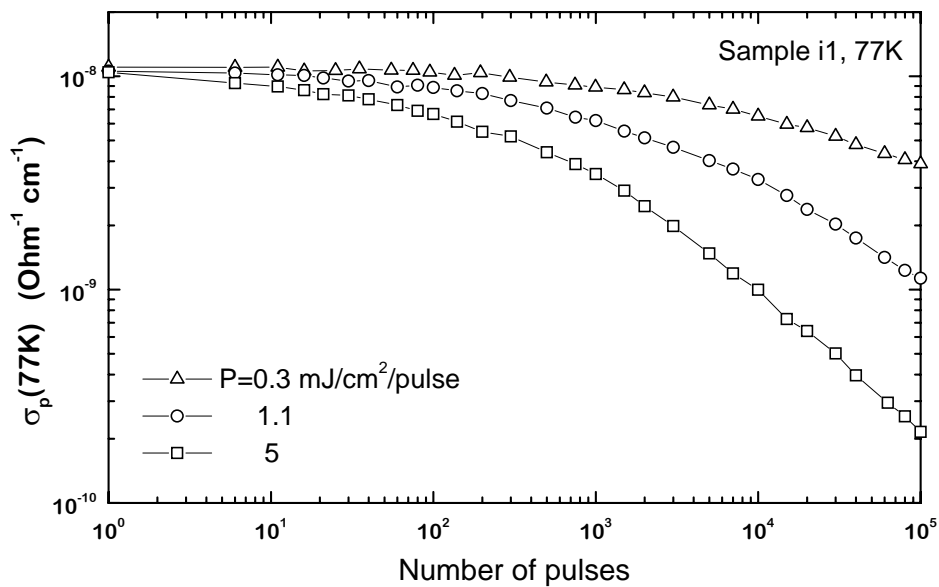


Figure 3.5. Low light photoconductivity of sample i1 at 77K, during light soaking with laser pulses at 77K. The low light generation rate was $1.8 \times 10^{18} \text{ cm}^{-3} \text{ s}^{-1}$. The laser pulse fluence for each run is shown in the graph. The lines are guides to the eye.

3.2.3. Annealing of metastable defects: After degradation with 10^5 laser pulses, the photoconductivity of the sample was measured from 77K to 300K. Since annealing of metastable defects created at 77K starts above 250K, and defects created at 300K can not be annealed by cooling the sample to lower temperatures, one can compare states

of the sample degraded at room temperature and at 77K, with the same laser power, by measuring the temperature dependence of photoconductivity from 77K to 250K. The comparison is shown in Fig.3.6. The photoconductivity of the sample in state A is included in the Figure. One can see that after 77K degradation with 10^5 laser pulses the photoconductivity is somewhat smaller than that after 300K pulse degradation. The same is true for CW degradation at 77K [Stradins *et al.* 1994], namely that for the same illumination time, light soaking at 77K degrades the photoconductivity as much as 300K soaking. Stradins *et al.* also measured the defect density created at 77K by lowering the sample temperature to 4.2K, measuring subgap absorption at 4.2K where CPM is valid, and then continuing degradation at 77K. Since we were not able to cool the sample below 77K, we could only measure reliable subgap absorption by CPM at temperatures higher than 200K. However, at these temperatures we would probably anneal a significant percentage of the light induced defects, which means that we would not measure the total light induced defect density.

In Fig.3.7 we plot the dependence of photoconductivity on T after laser pulse light soaking with 10^5 at 77K. One can see that the temperature of the onset of Thermal Quenching of photoconductivity drops as the defect density increases, in agreement with the discussion of §1.5. on the thermal behavior of photoconductivity in a-Si:H.

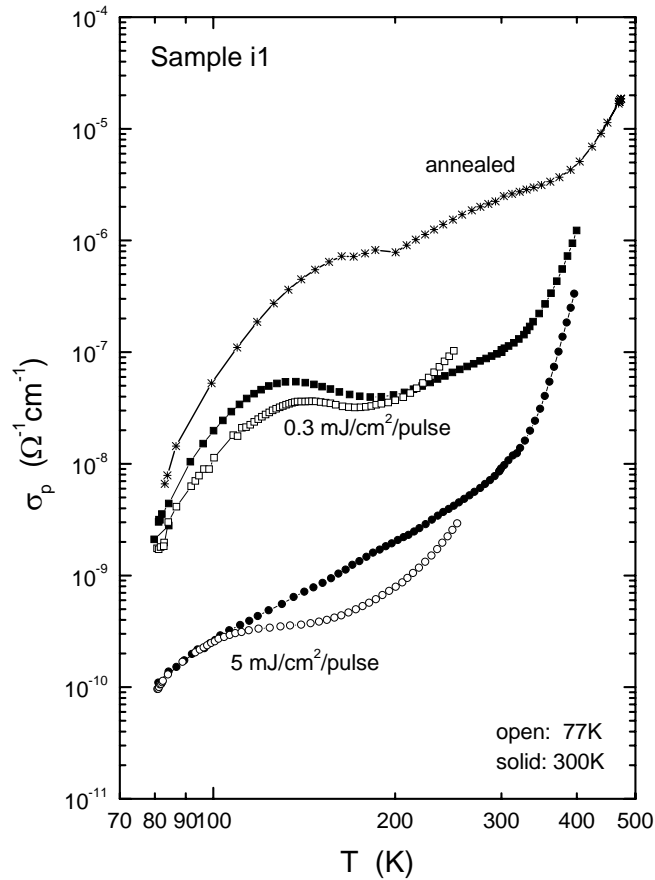


Figure 3.6. Low-light photoconductivity of sample i1 as a function of temperature, after degradation with laser pulses at 300K (solid symbols) and at 77K (open symbols), with comparable laser power shown in the graph. The photoconductivity in the annealed state is also plotted (stars). All curves were measured with $G=2 \times 10^{18} \text{ cm}^{-3} \text{ s}^{-1}$.

In Figs.3.8 we compare $\sigma_p(T)$ in the state fully degraded at 300K, with $\sigma_p(T)$ after degradation with 10^5 pulses at 300K and subsequent partial annealing at 400K and 420K. The result for degradation with the three laser powers is shown in Figs.3.8a, 3.8b, 3.8c. Once again, one can see the drop in the temperature of Thermal Quenching as the defect density increases. For the highest defect density reached, lower curve of Fig.8c, Thermal Quenching is not observed.

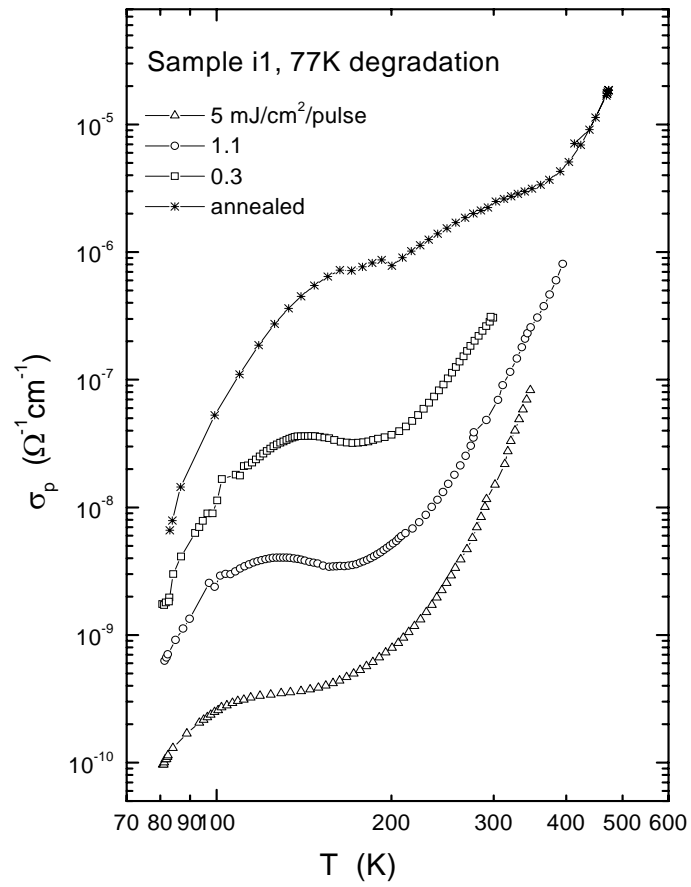


Figure 3.7. Low-light photoconductivity of sample i1, after degradation at 77K with 10^5 pulses of fluence shown in the graph. The annealed state photoconductivity is also plotted.

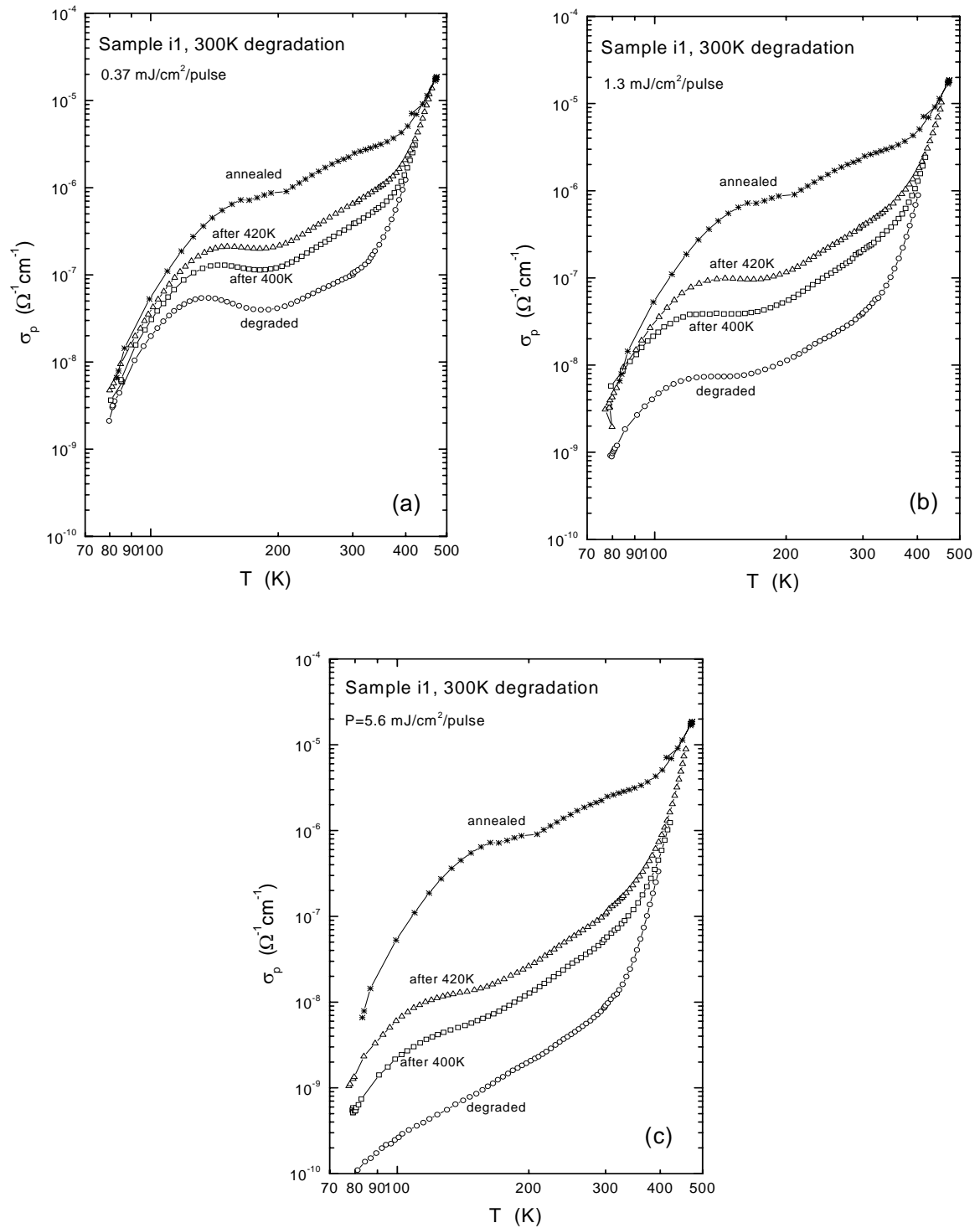


Figure 3.8. Low-light photoconductivity of sample i1, after degradation with 10^5 pulses of three different fluences (circles), and after partial annealing to 400K (squares) and to 420K (triangles). The photoconductivity of the annealed state is also plotted (stars). Graphs (a),(b),(c) correspond to degradation with the three different laser fluences P , shown in each graph.

In Fig.3.8a we observe that in the temperature region below thermal quenching the photoconductivity is almost identical for fully degraded and partially annealed states of the sample. As the temperature is increased and thermal quenching is initiated, the different defect density present in the degraded and in the partially annealed states causes splitting of the corresponding $\sigma_p(T)$ curves. However, as the light induced defect density becomes higher, Fig.3.8b, 3.8c, the low-light photoconductivity at temperatures below thermal quenching becomes sensitive to the defect density. One extreme case is the lower curve of Fig.3.8c, in which there is no sensitized state and thermal quenching is not observed.

3.3. Compensated samples

In this section we discuss the kinetics of light-induced defect creation in compensated samples. The interest in samples with compensated doping arises from the fact that the position of the dark Fermi level is the same as in undoped samples, but the native defect density is higher. This alters the degradation kinetics, as we will discuss in this section.

The characteristics of the samples c-20, c-100, used in this study, can be found in Appendix A.

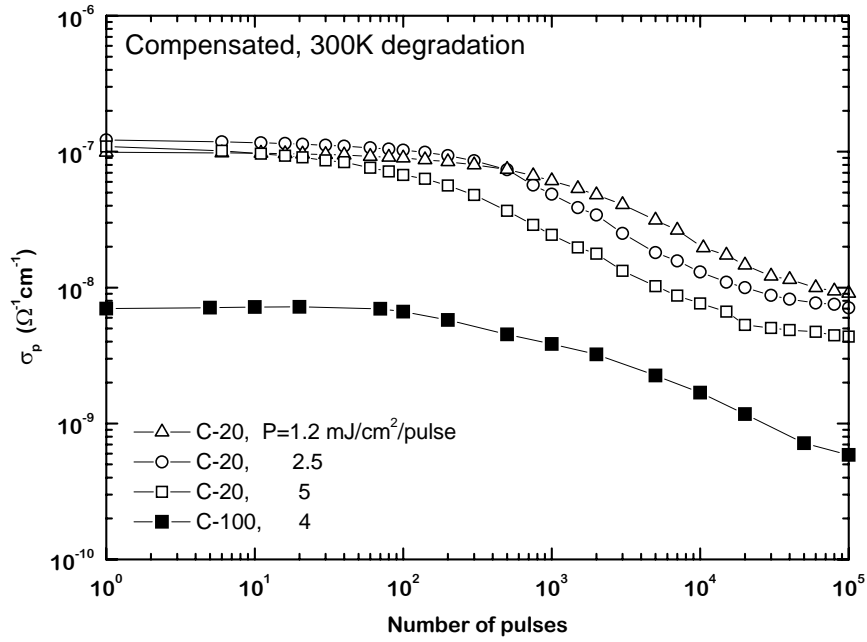


Figure 3.9. Low-light photoconductivity of compensated samples c-20, c-100, during light soaking with laser pulses at room temperature. Low light generation rate $G=2 \times 10^{18} \text{ cm}^{-3} \text{ s}^{-1}$.

In Fig.3.9 we plot the low light photoconductivity during laser pulse light soaking for the two compensated samples. The drop in photoconductivity after degradation with 10^5 pulses of comparable intensity is almost the same in the two samples. However, the evolution of the relative change in subgap absorption, $\Delta\alpha/\alpha_0$, is different for the

two samples, as shown in Fig.3.10. Sample c-20 follows a relation $\frac{\Delta\alpha}{\alpha_0} \propto P^1 N^{0.5}$,

similar to undoped samples. Sample c-100 behaves differently, showing $\frac{\Delta\alpha}{\alpha_0} \propto N^{0.2}$.

In sample c-100 the dependence of $\Delta\alpha$ on P can not be deduced from our measurements, because we only used a single laser intensity for light soaking.

Thus, we find that as compensated doping increases, the kinetics of the SW effect changes.

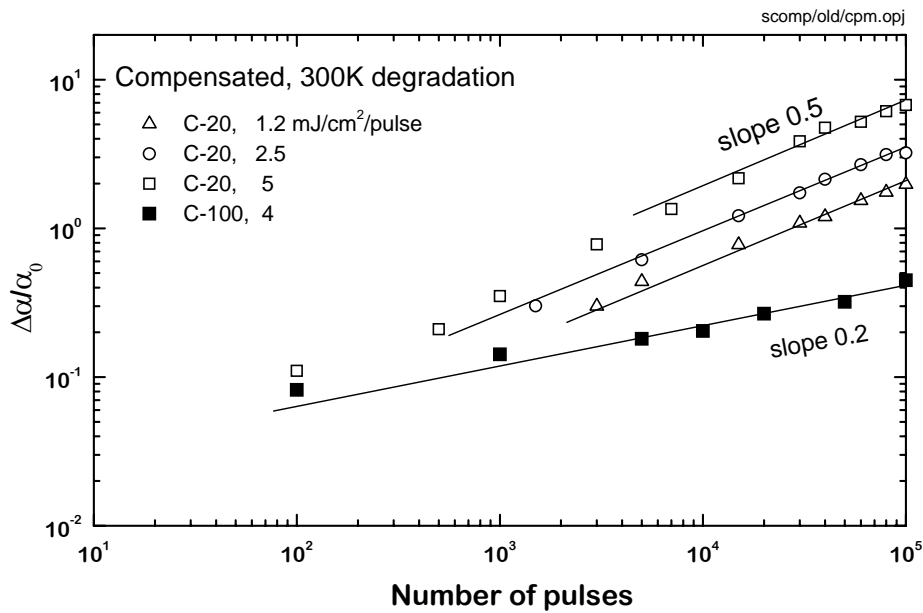


Figure 3.10. Relative change of subgap absorption of compensated sample c-20, c-100, during light degradation with laser pulses at room temperature.

Another important effect is shown in Fig.3.11, where the low light photoconductivity during pulsed and CW light soaking is plotted as a function of the subgap absorption.

One can see that in compensated samples too, the relation $\sigma_p \propto \frac{1}{N_D}$ is not observed.

In contrast to undoped sample i1, in compensated samples the low-light photoconductivity does not appear to be inversely proportional to the *light induced* defect density. Furthermore, the function $\sigma_p(N_D)$ is not a single-valued function, because for the same defect concentration, i.e. same subgap absorption, the low light photoconductivity is different for laser pulse and CW light soaking. Defects created with laser pulses degrade the low-light photoconductivity more than CW light-induced defects.

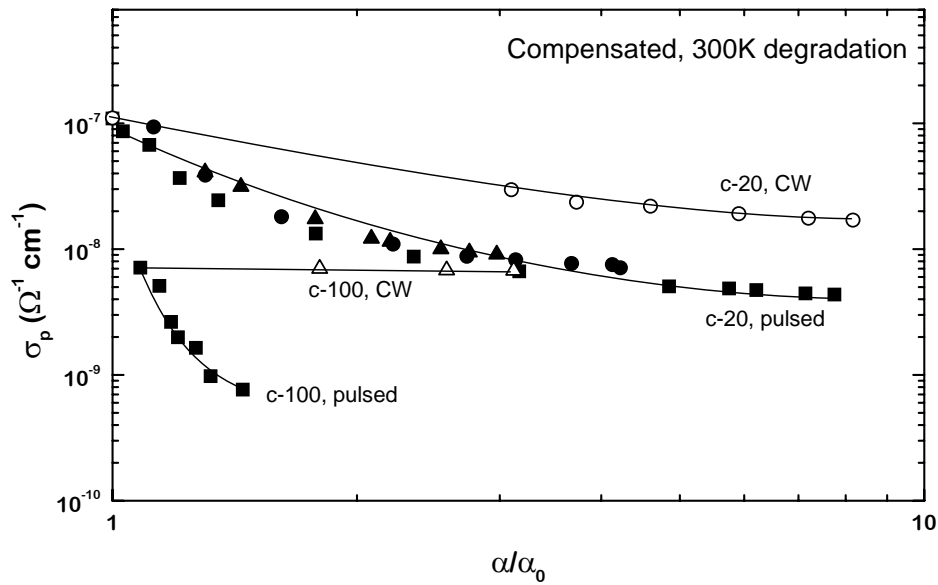


Figure 3.11. Low-light photoconductivity of compensated sample c-20, c-100, as a function of subgap absorption, during light soaking with laser pulses (solid symbols) and CW light (open symbols) at room temperature. The different solid symbols for c-20 correspond to the three laser intensities used. The lines are plotted as guide to the eye.

3.4. p-type sample

In the previous section we have shown that laser pulse light soaking has stronger effect on the photoconductivity than CW light soaking for the same change in subgap absorption in compensated samples. This is also true for p-type sample, p-20. The characteristics of sample p-20 used here can be found in Appendix A.

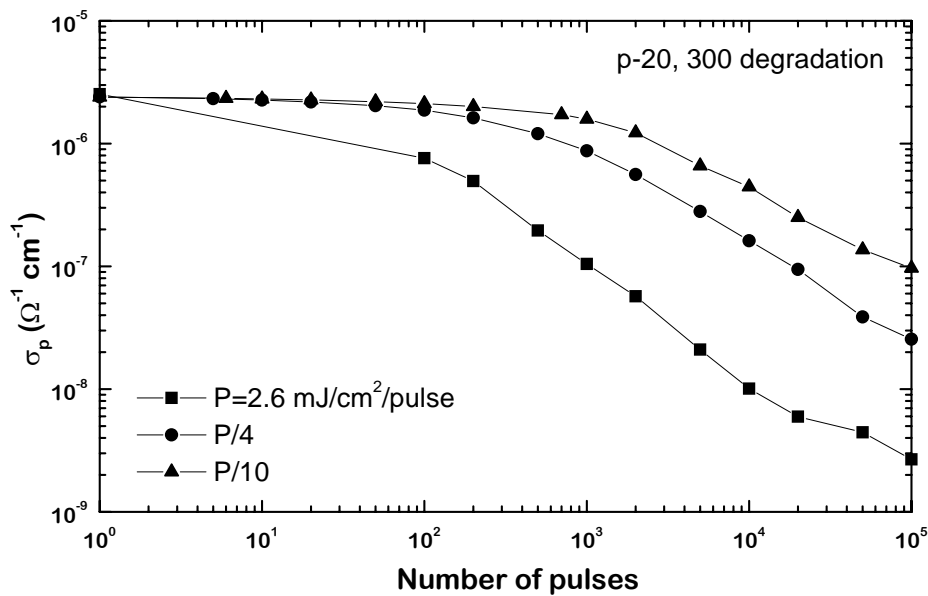


Figure 3.12. Low-light photoconductivity of p-type sample p-20 during degradation with laser pulses at room temperature.

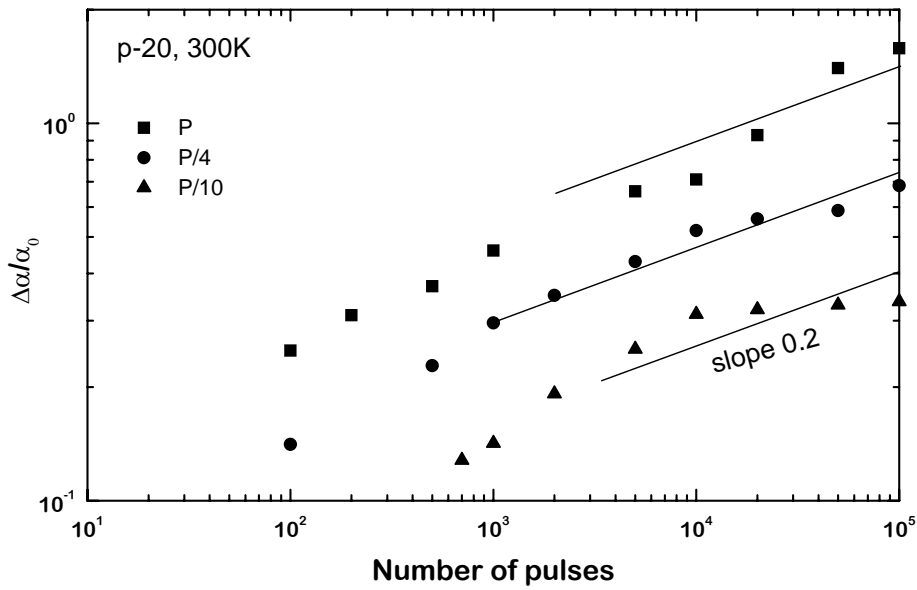
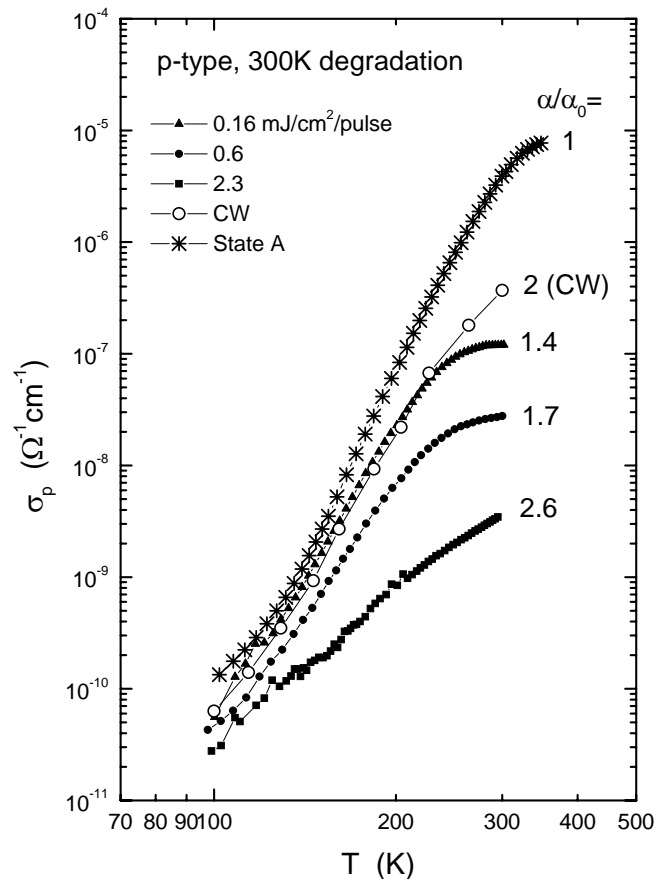


Figure 3.13. Relative change of subgap absorption of p-type sample p-20, during degradation with laser pulses at room temperature. The lines indicate the relation $\Delta\alpha/\alpha_0 \propto N^{0.2}$.

The light degradation of sample p-20 by laser pulses at room temperature is shown in Figs.3.12, 3.13. The relative change in subgap absorption follows a relation $\frac{\Delta\alpha}{\alpha_0} \propto P^{0.5} N^{0.2}$, again different than undoped samples.

Figure 3.14. Low-light photoconductivity of p-type sample p-20 after degradation with 10^5 pulses of different power (solid symbols) and after degradation with CW light (open symbols). The subgap absorption at each degraded state is shown. The annealed state photoconductivity is also plotted (stars).



The lines are plotted as guide to the eye.

Figure 3.14 demonstrates once again the different effect of CW and laser pulse light soaking on the low light photoconductivity, this time on sample p-20. The solid symbols represent $\sigma_p(T)$ after degradation with 10^5 laser pulses of fluence 2.3, 0.6 and 0.16 mJ/cm²/pulse. The change in subgap absorption reached after the three pulse degradation runs is shown in the Figure. The open symbols correspond to $\sigma_p(T)$ after CW degradation which increases α/α_0 by a factor 2. The photoconductivity in the annealed state is plotted for comparison. One can see that a state with $\alpha/\alpha_0 = 1.7$ reached with laser pulse light soaking has lower photoconductivity than a state with $\alpha/\alpha_0 = 2$ attained with CW light soaking* .

3.5. Discussion

An important result of this Chapter is that the low-light photoconductivity σ_p is not a single-valued function of the total defect density. We find that the effect of light induced defects (LIDs) on σ_p depends on the light soaking conditions. LIDs created with laser pulses degrade σ_p more than defects created with CW light, for the same total defect density. This may be understood as follows. Under illumination with laser light, the quasi-Fermi levels of electrons and holes lie much closer to the respective bands than under CW light. This means that the energy released in the material by recombination of photocarriers will be higher in the case of laser irradiation. As we discussed in Chapter 2, the energy released by recombination is related to the creation of defects. Thus, there is more available energy for defect creation under laser light than under CW light, suggesting that the overall structural change occurring when a defect is created, will be different under illumination with CW or laser light. Defects created with laser soaking may have larger capture cross section for photocarriers, and thus have a significant effect on the photoconductivity. This is seen in compensated samples, in which CW light soaking creates LIDs but little decrease in photoconductivity is observed, in contrast to laser degradation which reduces significantly the photoconductivity. Also in the p-type sample, defects created with laser light degrade the photoconductivity more than equal density of defects created by CW light soaking.

Another effect of laser irradiation on compensated samples might be the screening of potential fluctuations, i.e. internal electric fields, in these samples at the high densities of photocarriers reached with the laser [Tzanetakakis *et al.* 1996]. It is suggested [Stradins *et al.* 1996] that these internal fields are responsible for the low efficiency of defect creation with CW light in these samples. This however will not affect LID creation with laser pulses, because of screening at high photocarrier densities.

We observe that degradation kinetics of undoped sample i1 and compensated sample c-20 are similar. As already discussed, the quasi-Fermi levels under illumination with laser light lie very close to the bands. For undoped samples, this means that the tail states are filled up to an energy close to the band edge. The very high density of photocarriers under the laser, in addition to the tail states, also fills the dopant states in compensated samples, making the quasi-Fermi levels in undoped and compensated samples the same. For this reason, the recombination kinetics in these samples will be

* Of course the low light photoconductivity in each case was measured with the same low light intensity.

similar and the defect creation kinetics with laser pulses will also be similar. This argument holds for lightly compensated sample, c-20. In sample c-100 we find different kinetics of LID creation. This sample has higher native defect density, which alters the recombination kinetics, as we will discuss in the next Chapter.

So far we discuss recombination-driven LID creation, based on commonly used assumptions on the mechanism of recombination under laser pulse illumination. In the next Chapter we will present the first study of recombination in Hydrogenated amorphous Silicon, at very high densities of photocarriers. As we will see, this study will give us important information and insight on the creation of defects by laser pulses.

Chapter 4. Photoconductivity under pulsed laser light

4.1. Introduction

All models presented in Chapter 2 for the interpretation of the Staebler-Wronski effect, assume that light-induced defect creation in a-Si:H is driven by the recombination of photocarriers. In the case of degradation by short, intense laser pulses, all previous studies are based on a generally accepted assumption concerning the recombination of the very high density of photocarriers generated by the laser pulse. This is, in brief, [Stutzmann *et al.* 1985], [Meudre *et al.* 1993] that the photocarrier lifetime τ is much larger than the pulse duration τ_{pulse} . Consequently, the photocarrier density generated during the pulse is proportional to $I_{\text{pulse}}\tau_{\text{pulse}}$, where I_{pulse} is the intensity of the pulse. This photocarrier density decays, after the end of the pulse, with lifetime $\tau \propto 1/N_D$, N_D being the total defect density of the material. τ is assumed to be of the order of 10^{-6} s.

One can measure the time dependence of the photocarrier density $n(t)$ by measuring the photoconductivity $\sigma_{\text{LP}}(t)$ of the sample during the laser pulse. The photocarrier density is related to σ_{LP} with the known relation $\sigma_{\text{LP}}(t) = en(t)\mu_0$, where e is the absolute value of the electron charge, and μ_0 the electron microscopic mobility in a-Si:H. As usually, we assume that electrons dominate the photocurrent in undoped material. However, a photocurrent measurement in nanosecond time scale requires GHz response of the photocurrent detection system. Such a high frequency imposes severe gain limitations and the measurement has never been performed.

We measured σ_{LP} in undoped and compensated samples. The samples used were i1, c-20, c-100, same as the ones in Chapter 3, and an additional undoped sample i2. Their characteristics can be found in Appendix A.

The photocurrent during the laser pulse was measured by the voltage drop across a 50Ω resistor and a fast Digital Storage Oscilloscope. The time resolution of the measurement was 2.5ns, enough to cover the 30ns time duration of the laser pulse. The set-up employed is described in Appendix B.

In the first experiment, presented in §4.2, we measured σ_{LP} during laser pulse degradation with 10^5 pulses at room temperature, in order to examine how σ_{LP} is affected by the light-induced defects. At the same time, the low-light steady state photoconductivity and subgap absorption were measured, in the same way as in Chapter 3. The measurement of σ_{LP} is a direct measurement of both the photocarrier density created by the laser pulse and the decay of this density after the pulse is over. This means that one can obtain information about the recombination of photocarriers generated by the soaking light itself, in the course of a laser light soaking experiment. This information is crucial for the understanding of the mechanism of recombination-driven defect creation.

In the second series of σ_{LP} measurements, presented in §4.3, we shielded the sample holder, in order to reduce the pick up of electromagnetic noise, and measure $\sigma_{LP}(t)$ with better accuracy, over a wide range of laser pulse fluences. The shielded set-up is described in more detail in Appendix B.

The laser pulse profile was measured with a fast Metal-Semiconductor-Metal (MSM) photodiode, having response time lower than 1ns.

The various laser pulse intensities, from 35 to 2×10^{-3} mJ/cm²/pulse, used in this study, were obtained with the help of a series of neutral density filters, calibrated at 650nm, the wavelength of the laser light.

4.2. Laser pulse photoconductivity during light degradation

The photoconductivity induced by the laser pulse was measured in sample i1, during light soaking with 5×10^4 pulses of 8 mJ/cm²/pulse. This sample is the same as that used in Chapter 3. We measured the photocurrent induced by the soaking laser light, i.e. photocurrent induced by the 8 mJ/cm² pulses. In order to reduce the noise in the laser pulse photocurrent measurement, we average over 5 laser pulses. Low-light photoconductivity and the change in subgap absorption were also measured, in the same manner as described in Chapter 3.

The results are shown in Fig.4.1. In this Figure we plot the voltage drop created by the sample photocurrent across the 50Ω resistor. The three traces correspond to three different states of the sample during laser light soaking: annealed state (pulse to the left), state after irradiation with 2×10^4 pulses of power 8 mJ/cm²/pulse (medium pulse) and state after irradiation with 5×10^4 pulses of the same power as above (pulse to the right). The number of pulses the sample was irradiated with, is denoted by N, in Fig.4.1. The profile of the laser pulse, measured with the MSM photodiode, is plotted with the line on top of the pulse to the right, in Fig.4.1.

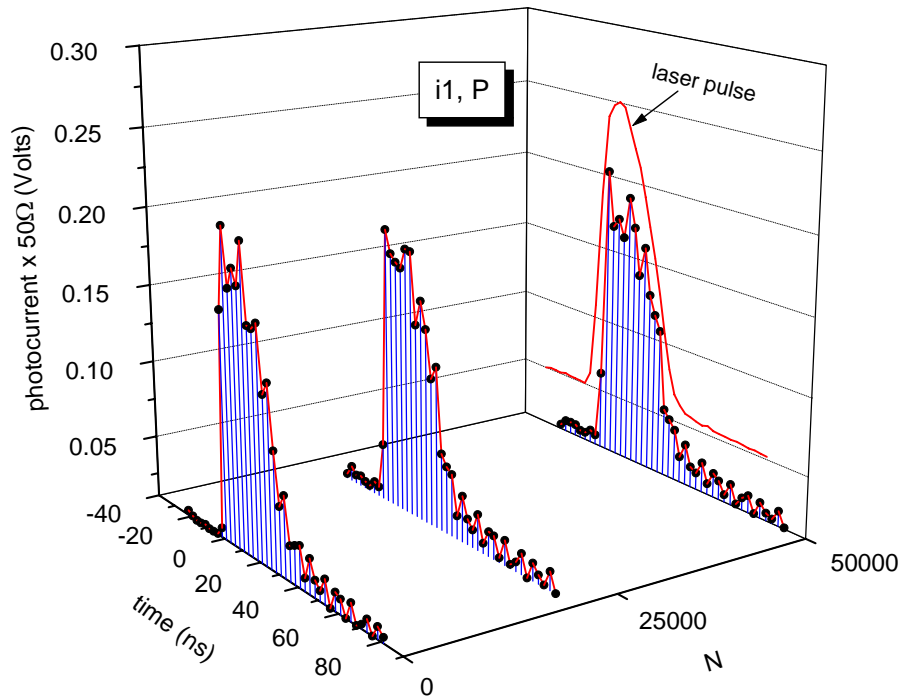


Figure 4.1. Photocurrent of sample i1 under the laser pulse after degradation with N laser pulses. The photocurrent of the sample is measured by the voltage drop across a 50Ω resistor. The laser pulse profile measured with the MSM photodiode, is shown as well. The measurement was performed at room temperature and the laser fluence was $P=8 \text{ mJ/cm}^2/\text{pulse}$ same for measurement and for degradation.

One can see that the rise of the sample photocurrent follows the rise of the laser pulse. This means that the response time of the sample is faster than a few nanoseconds, and a quasi-steady state is reached during the laser pulse.

The decay of photocurrent after the end of the light pulse is also very fast, much faster than the usually assumed 10^{-6} s (see §2.2), as one can see in Fig.4.1.

A surprising fact is that the magnitude and the time evolution of the photocurrent during the laser pulse remains the same after light soaking with 5×10^4 pulses. The contrast of this fact to the strong degradation of low-light photoconductivity during laser pulse irradiation is demonstrated in Fig.4.2. The solid symbols correspond to low-light photoconductivity measured with $G=2 \times 10^{18} \text{ cm}^{-3} \text{ s}^{-1}$, during the degradation run. The open symbols correspond to the peak of photoconductivity, reached during the laser pulse. As discussed above, this peak represents a quasi steady-state of photoconductivity for the very high generation rate of the pulse. Note the break in the vertical axis. One can see in Fig.4.2 that during the whole degradation run, the photoconductivity under by the laser light remains constant, while the subgap absorption α/α_0 is increased by a factor of 7, and the low-light photoconductivity is decreased by a factor of 500.

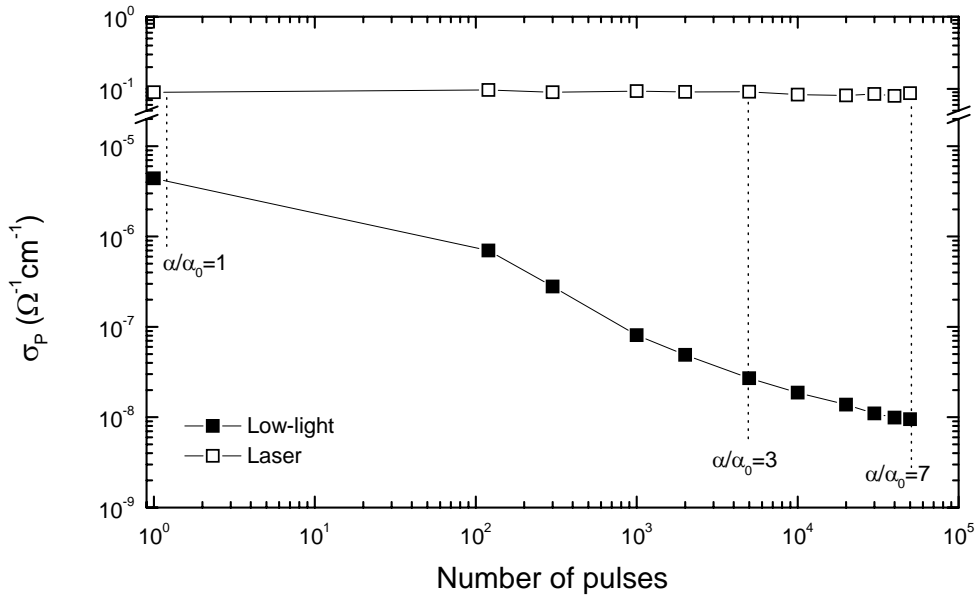


Figure 4.2. Photoconductivity under low-light (solid symbols) and under laser pulse light (open symbols), during degradation with $8\text{mJ}/\text{cm}^2$ pulses at room temperature. Note the break in the σ_P axis. The relative change in subgap absorption is also shown at two stages of degradation. The solid lines are guides to the eye.

The photoconductivity σ_{LP} , during the laser pulse, remains almost constant even for a laser light flux lower than the power used for degradation. This is shown in Fig.4.3, where we plot the photocurrent transients for laser pulse attenuated by a factor of 10 as compared to that used for degradation and for the measurements of Fig.4.1. N in Fig.4.3 again represents the number of $8\text{mJ}/\text{cm}^2$ pulses, as in Fig.4.1, but now the photoconductivity σ_{LP} is measured with pulse power $0.8\text{mJ}/\text{cm}^2$. This measurement shows that σ_{LP} remains constant during a degradation run, even when it is measured with attenuated laser pulse. In §4.3, σ_{LP} under laser light attenuated by a factor of 1000 or higher will be shown, and the effect of defects on σ_{LP} under attenuated laser light will be discussed.

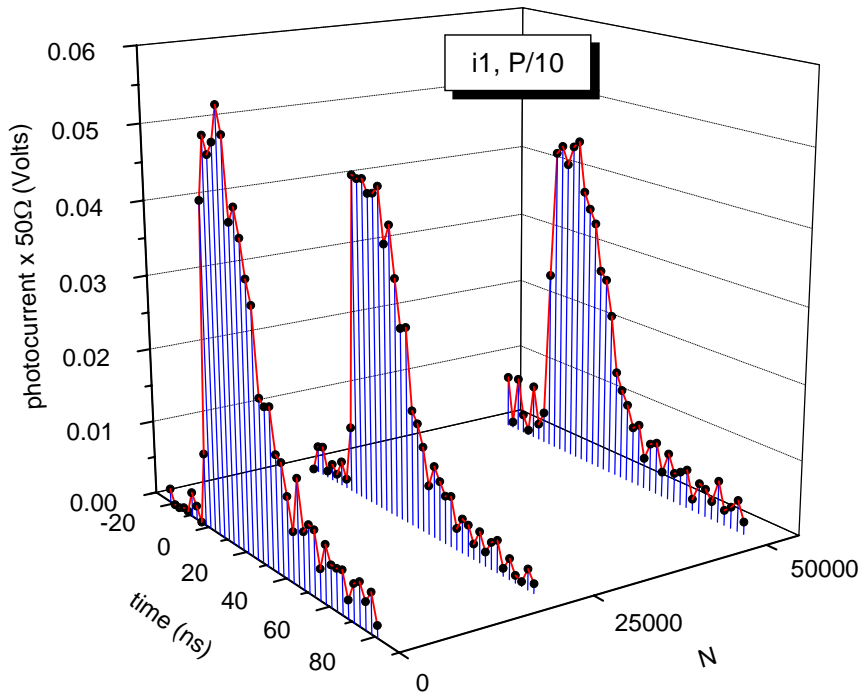


Figure 4.3. Photocurrent of sample i1, under laser pulses of fluence $P/10=0.8\text{mJ}/\text{cm}^2/\text{pulse}$, after degradation with N pulses of $8\text{mJ}/\text{cm}^2$. The measurement was performed at room temperature.

A second surprising observation is that the photocurrent during the laser pulse follows the time evolution of the pulse also in the compensated samples c-20, c-100. In these samples too, quasi-steady state is reached during the 30ns of the laser pulse, and the magnitude and time evolution of the photocurrent are almost unaffected by the light induced defects. This observation is discussed further in §4.4.1.

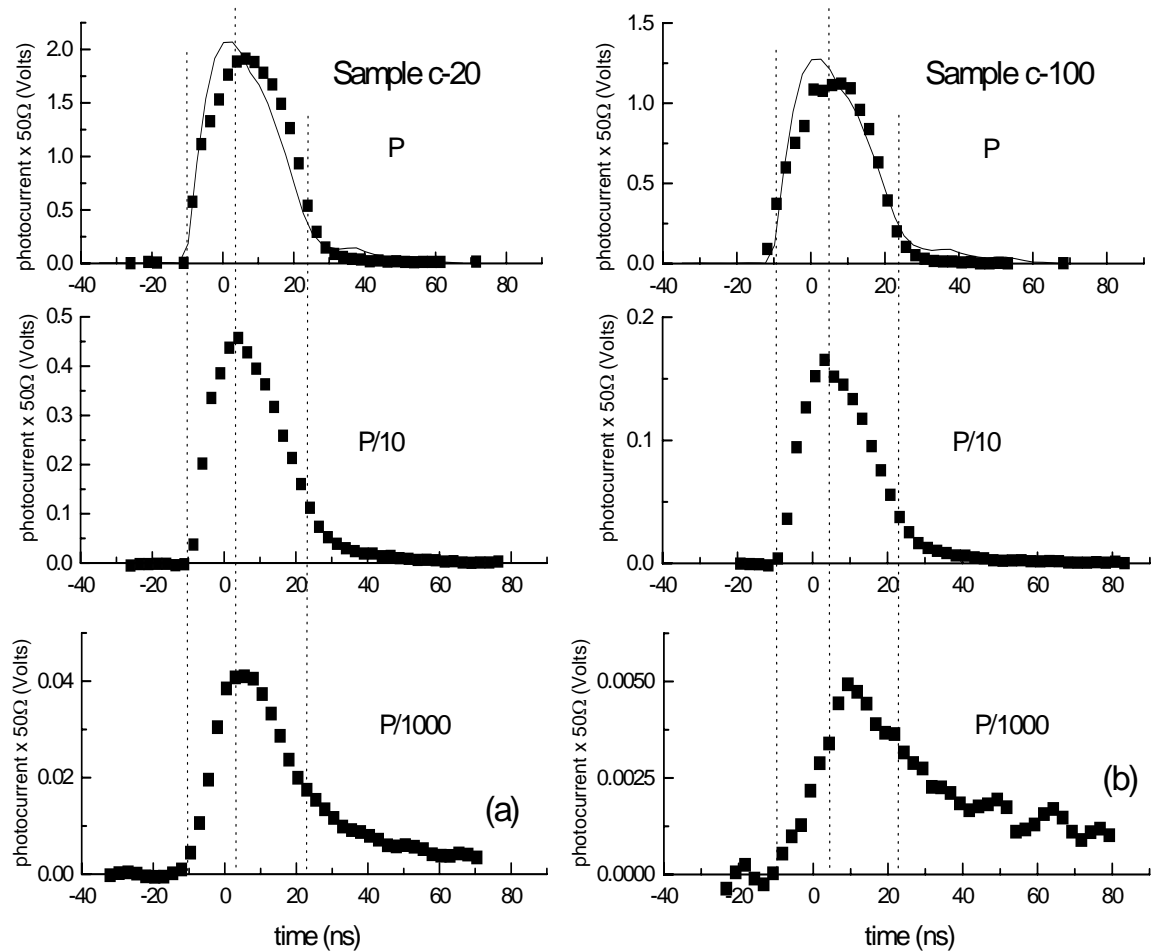
4.3. Dependence of pulse photoconductivity on doping and light generation rate

In the previous section we showed that the photoconductivity σ_{LP} during the 30ns laser pulse changes only slightly with degradation. Quasi steady-state, unaffected by light-induced defects, is reached during the pulse for pulse light flux attenuated by a factor of 10. However, the measurement of photocurrent in nanosecond time scale is subject to electromagnetic interference noise, as one can see in Figs.4.1,4.3 of §4.2. In order to further reduce the laser flux and measure σ_{LP} , reduction of noise is needed. This was accomplished with the use of a shielded sample holder, described in Appendix B. Reduction of the laser light flux is needed in order to study the surprisingly fast time response of σ_{LP} in a wider range of photocarrier generation rates. In this section we present the measurements of the photoconductivity σ_{LP} during laser pulses in samples i1, i2, c-20 and c-100, at room temperature, over a wide range of laser fluxes. The samples were well annealed before the measurement, as a precaution in case there are significant degradation effects in σ_{LP} under attenuated laser light.

We have measured the photocurrent during the pulse for pulse power varied between $P=35\text{ mJ}/\text{cm}^2/\text{pulse}$ and $P/20000=1.7\text{ }\mu\text{J}/\text{cm}^2/\text{pulse}$. The wavelength of the laser light

is 650nm, as usual. The pulse profile was measured with the MSM photodiode, in the same manner as in §4.2. The photocarrier generation rate of the laser pulse is calculated assuming a square pulse of 30ns time width.

Figure 4.4. Photocurrent traces of compensated samples c-20 (a), c-100 (b) for laser fluences



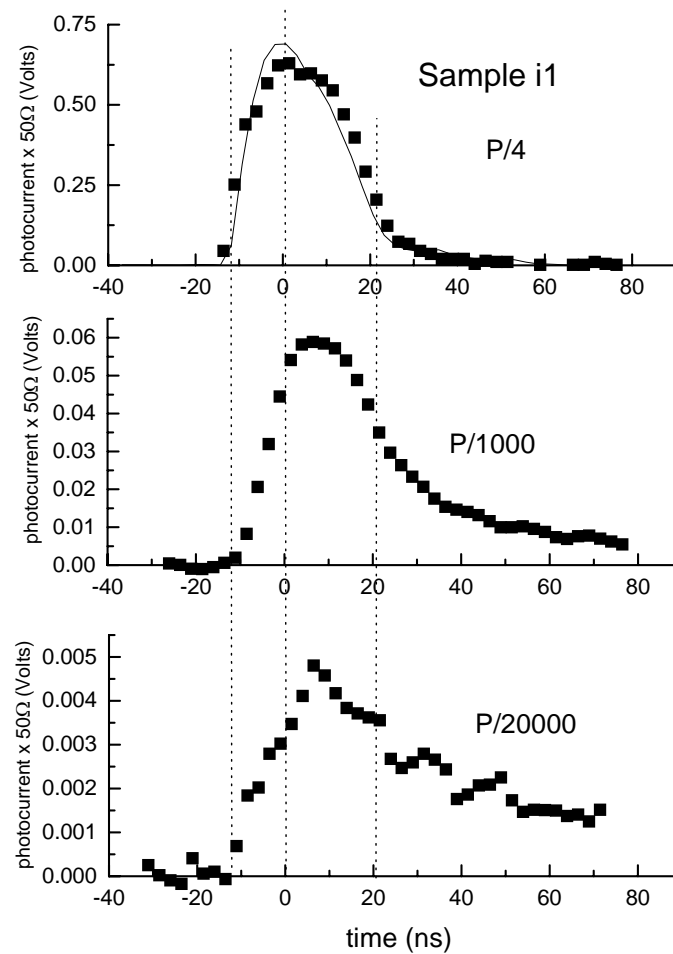
$P=35\text{mJ}/\text{cm}^2/\text{pulse}$, P/10 and P/1000. The measurements were performed at room temperature. The laser pulse profile, measured with the MSM photodiode is shown by the solid line. The vertical dotted lines indicate approximately the beginning, the maximum and the end of the laser pulse.

In Figs.4.4a, 4.4b we show the photocurrent induced by the laser pulse in samples c-20, c-100, for three different laser powers. The laser pulse profile, measured with the MSM photodiode, is plotted as a solid line in the uppermost plot of each Figure.

In Figs.4.4a,4.4b we see that the photocurrent follows the evolution of the laser pulse for the higher laser intensities. After the end of the pulse, the photocurrent in the sample drops to zero.

As the laser intensity is decreased, the rise in photocurrent is almost linear, thus does no longer follow the rise of the light.

Figure 4.5. Photocurrent traces of sample i1, under laser pulse of fluence $P/4$, $P/1000$ and $P/20000$, where $P=35 \text{ mJ/cm}^2/\text{pulse}$. The laser pulse profile is shown as a solid line. Vertical dotted lines indicate



approximately the beginning, the maximum and the end of the laser pulse.

Fig.4.5 shows the same measurement in undoped sample i1, at low laser intensities. The rise in photocurrent is again similar to that of the light pulse for high pulse intensities, and linear for low intensities. After the end of the light pulse, no photocurrent remains for high intensities. For very low intensities (lowest one in Fig.4.5), there is a significant amount of photocurrent left to decay after the light pulse is over.

The photocurrent induced by the laser, was measured from $P=35 \text{ mJ/cm}^2/\text{pulse}$ to $P/20000=1,7 \times 10^{-3} \text{ mJ/cm}^2/\text{pulse}$ in all samples. In the Figures presented so far, we only plotted three photocurrent transients for each sample.

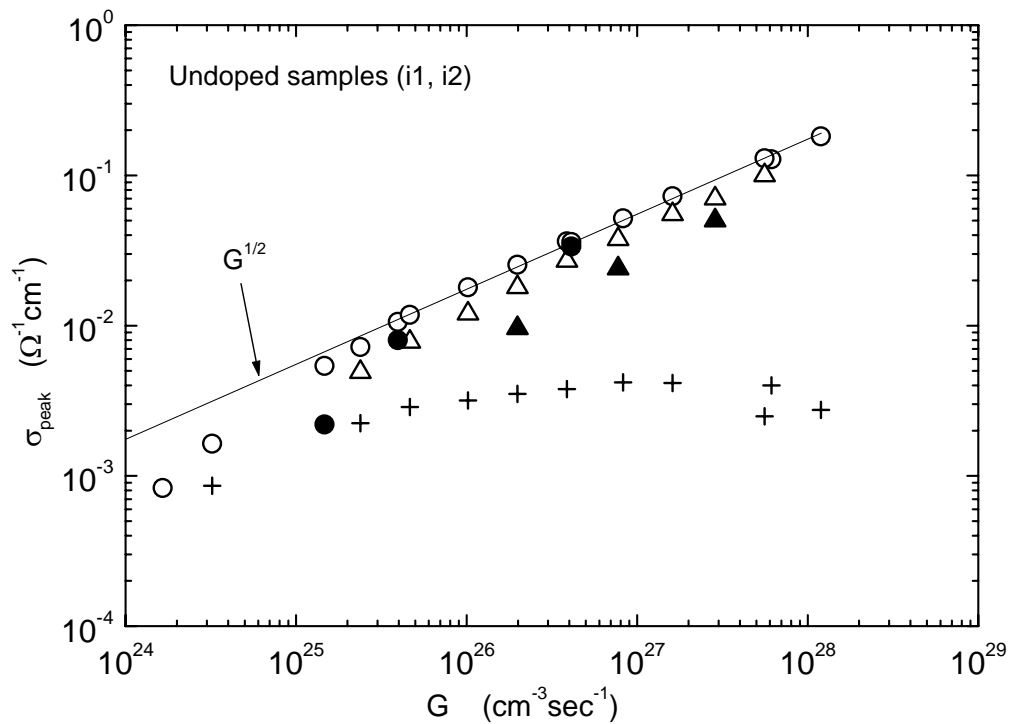


Figure 4.6. Peak of photoconductivity of undoped samples i1 (circles) , i2 (triangles) versus laser pulse photogeneration rate G , in the annealed (open symbols) and degraded state (solid symbols). The crosses represent the photoconductivity at 40ns, i.e. 20ns after the end of the laser pulse. The line indicates $\sigma_{\text{peak}} \propto G^{1/2}$.

In Fig.4.6 we plot the peak of photoconductivity σ_{peak} reached during the light pulse in undoped samples i1, i2, as a function of photocarrier generation rate in the whole range of laser intensities studied. The measurements were performed in annealed and degraded state of the samples. One can see that degradation with 10^5 laser pulses affects σ_{peak} only at very low laser intensities, as discussed in §4.2. The crosses in Fig.4.6 represent the photoconductivity at 40ns, i.e. about 20ns after the end of the light pulse, as one can see in Figs.4.4, 4.5. This represents the photocarrier density left after the end of the pulse, which appears to saturate as the laser intensity is decreased.

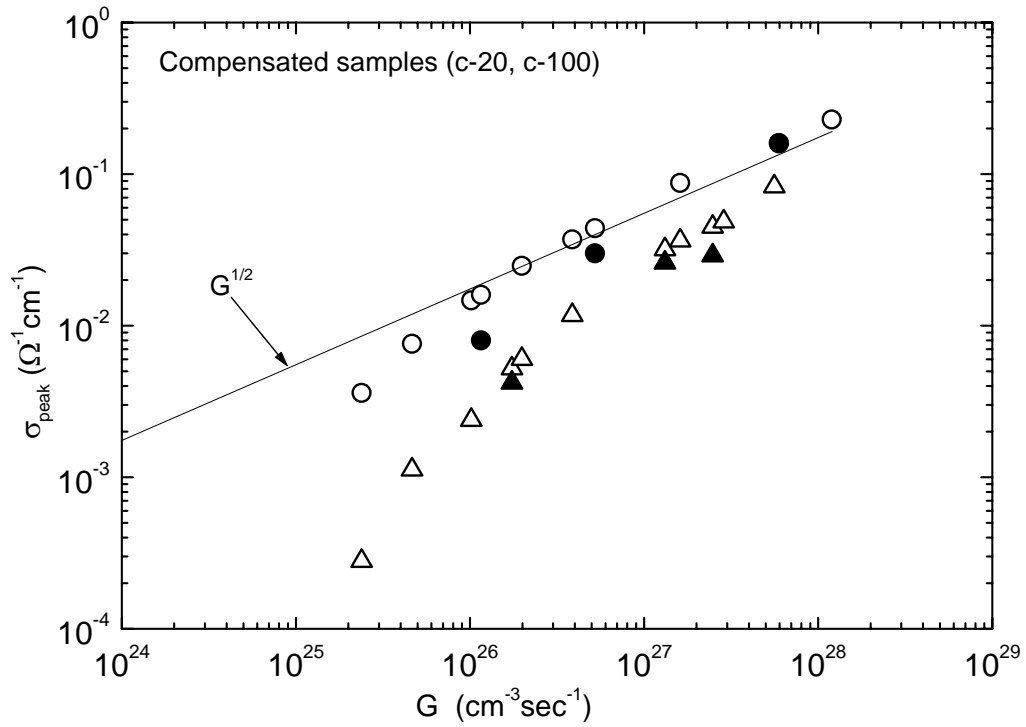


Figure 4.7. Peak of photoconductivity of compensated samples c-20 (circles) and c-100 (triangles), versus laser pulse photogeneration rate G , in the annealed (open symbols) and degraded state (solid symbols). The line is the same as in Fig.4.6. Note also that the scale of figs.4.6 and 4.7 is the same.

For high generation rates the points follow exactly the relation $\sigma_{\text{peak}} \propto G^{1/2}$, both in annealed and degraded state. At low laser intensities, the measurements deviate from the $G^{1/2}$ relation. This deviation occurs at higher generation rates in the degraded state.

In Fig.4.7 we plot σ_{peak} in compensated samples c-20, c-100. Note that the scale in Figs.4.6 and 4.7 is the same. The points again follow a $G^{1/2}$ relation for high laser pulse intensities, and deviate from $G^{1/2}$ at low intensities. The deviation from $G^{1/2}$ occurs at higher G in sample c-100.

4.4. Discussion

4.4.1. Universality of laser pulse photoconductivity: In Figs.4.6, 4.7 we observe that the photoconductivities of all samples reach the same value at $G \geq 5 \times 10^{26} \text{ cm}^{-3} \text{ s}^{-1}$, regardless of native defect density and doping. It is important to note that the photoconductivities of the same samples in the annealed state at low ($\approx 10^{18} \text{ cm}^{-3} \text{ s}^{-1}$) generation rates are different by factors as large as three orders of magnitude. Furthermore, the low-light photoconductivity degrades strongly with light soaking, while the photoconductivity under the high generation rate of the laser pulse is unaffected.

The difference in low-light annealed-state photoconductivities between the undoped and compensated samples studied, occurs mainly for two reasons. One is the difference in native, i.e. minimum, defect density in these samples (see Appendix A) which affects the recombination rate through defects and thus the lifetime of

photocarriers. The second reason is the decrease in the drift mobility of photocarriers in compensated samples, caused by potential fluctuations [Tzanetakis *et al*, 1993]. We find that the photoconductivity σ_{LP} under the laser pulse is insensitive to both defect density and potential fluctuations.

As discussed in §1.4, for bimolecular, i.e. band-to-band, recombination, the photoconductivity σ_P varies with photocarrier generation rate G as $\sigma_P \propto G^{1/2}$. As we see in Figs.4.6, 4.7, the photoconductivity at very high densities of photocarriers indeed shows this $G^{1/2}$ dependence. This means that under the laser pulse, recombination is bimolecular, independent of the defects in the sample. One thus expects that the photoconductivity during the high intensity pulses will not be affected by the native or light induced defect density. This is in agreement to our observations that all samples reach the same photoconductivity σ_{peak} during high intensity laser pulses, and that σ_{peak} is unaffected by light soaking.

The very high densities of photocarriers reached with laser pulses will also screen whatever potential fluctuations are present in compensated samples, diminishing their effects on the transport properties.

4.4.2. Recombination at very high photocarrier densities: The photocurrent transients presented in §4.2 and §4.3 show that the response time of the sample is very fast, faster than the rise time of the laser pulse for the higher intensity pulses. The decay time is also short and the majority of photocarriers recombine during the high intensity laser pulses.

The range of σ_{peak} for which $\sigma_{peak} \propto G^{1/2}$ holds, is approximately from 10^{-2} to 10^{-1} (Ωcm)⁻¹, as can be seen in Figs.4.6, 4.7. We can calculate the corresponding photocarrier densities, n , from $\sigma_{peak} = \mu_0 en$. Taking the widely accepted value for the microscopic mobility in a-Si:H, $\mu_0 = 10 \text{ cm}^2/\text{Vs}$, we find the corresponding density of photocarriers n to be in the range from 6×10^{15} to $6 \times 10^{16} \text{ cm}^{-3}$.

For quasi-steady state under photocarrier generation rate G , one can estimate the photocarrier lifetime τ from $G = n/\tau$. For the above range of photocarrier densities and the corresponding range of G , between 10^{26} and $10^{28} \text{ cm}^{-3} \text{ s}^{-1}$ (see Figs.4.6, 4.7) one finds that τ lies between 6×10^{-12} and $6 \times 10^{-11} \text{ s}$. This estimate for the photocarrier lifetime is in agreement with the observation that there is practically no difference in time scale between laser pulse and sample photocurrent, measured with resolution of a few nanoseconds. In other words, this estimate of photocarrier lifetime indicates that quasi-steady state is reached during the ns light pulse and thus the vast majority of photocarriers recombine during the pulse, by a bimolecular process. This agreement of estimated and observed photocarrier lifetime also justifies our choice of the value of the microscopic mobility μ_0 . We thus speculate that the microscopic mobility in a-Si:H will be the same over a very wide range of photocarrier concentrations.

In the discussion so far we were dealing with $G \geq 10^{26} \text{ cm}^{-3} \text{ s}^{-1}$. As the generation rate is decreased below this value, σ_{peak} in Figs.4.6, 4.7 lies below the $G^{1/2}$ relation. This happens for two reasons. The first is that as G is decreased, the response time of the sample becomes longer than the pulse duration τ_{pulse} and thus steady state is not reached. The photoconductivity in this case rises linearly with time, reaching a value

$\sigma_{\text{peak}} = G\tau_{\text{pulse}}$, lower than the steady state value. This effect is seen in the shape of photocurrent transients of Figs.4.4, 4.5 at low laser intensities.

The second reason is that as the pulse generation rate is lowered, recombination through defects becomes increasingly important. This is manifested by the observation that degradation does affect the laser pulse photoconductivity σ_{peak} , under the lowest intensities. One can also see in Figs. 4.6, 4.7, that σ_{peak} starts to deviate from the $G^{1/2}$ dependence at higher G when the sample is light soaked, another confirmation that recombination through defects becomes important as G is lowered.

4.4.3. Consequences of these experimental observations on defect creation models: The bond breaking models of light-induced defect creation with laser pulses, assume that the response time of the sample is much larger than the pulse duration, and that the decay lifetime of photocarriers after the end of the pulse is of the order of 10^{-6} s. This lifetime τ corresponds to recombination of photocarriers mainly through defects, and so τ decreases as $\tau \propto 1/N_D$, where N_D is the total defect density in the sample. According to these assumptions (discussed in §2.2.1), the photocarrier density cannot reach steady state during the pulse, and the majority of photocarriers recombine after the end of it, with lifetime of the order of 10^{-6} s.

Our measurements do not validate these assumptions. We find that quasi-steady state is reached during the nanosecond laser pulse, and most recombination events happen during the pulse and not after the end of it. These findings hold for laser powers higher than about $P/100 = 0.3 \text{ mJ/cm}^2/\text{pulse}$, which are typical in laser light soaking experiments. The lifetime of photocarriers at these laser intensities is estimated to be less than 10^{-10} s and the dominant recombination path is bimolecular, independent of defects. The density of photogenerated carriers by the laser pulse is the same irrespective of degradation with up to 10^5 pulses of a few $\text{mJ/cm}^2/\text{pulse}$.

One very important question arises naturally from the above discussion: we found in Chapter 3 that the defect density N_D increases with laser light soaking as $N_D \propto N^m$, where N is the number of pulses and $m < 1$ in all samples. However in the above discussion we argue that the density as well as the lifetime of photocarriers remain the same in the course of laser light soaking. This means that one would expect the rate of defect creation to be the same in the beginning and in the end of the degradation run, i.e. $N_D \propto N^1$ in undoped and compensated samples. The experimental observation of $N_D \propto N^m$, where m is always less than unity, and is different in samples with different compensated doping can not be explained with the bond-breaking models, in the light of our new findings concerning the recombination of photocarriers created by laser pulses.

In Chapter 3 we have shown that laser pulse light soaking is more efficient in creating defects than CW light. In view of the findings of this Chapter on the recombination of high densities of photocarriers, we can give another aspect of laser versus CW degradation. This is the following. During CW light soaking with light of generation rate G_{CW} , the recombination rate is equal to the generation rate. Thus, the total number of recombination events per unit volume in a CW light soaking run with time duration t_{ill} is $G_{\text{CW}}t_{\text{ill}}$. Under laser pulse soaking with pulses of generation rate G_{pulse} and duration τ_{pulse} , according to our findings, quasi-steady state is reached during the

pulse and thus the generation rate will again be equal to the recombination rate. Furthermore, there is no photocarrier concentration left after the end of the pulse, thus the total number of recombination events per unit volume in the material is $G_{\text{pulse}}\tau_{\text{pulse}}N_{\text{tot}}$, where N_{tot} is the total number of pulses in the degradation run. Taking the example of Fig.3.2 of Chapter 3, we compare the number of recombination events R_{CW} during light soaking with CW light of power 0.27 W/cm^2 for 1000min, to the number of recombination events R_{pulse} during light soaking with 10^5 , 5 mJ/cm^2 pulses of 30ns. We find $R_{\text{CW}} \approx 2 \times 10^{26}/\text{cm}^3$, while $R_{\text{pulse}} \approx 6 \times 10^{24}/\text{cm}^3$. According to Fig.3.2, CW light soaking with 0.27 W/cm^2 for 1000min, caused an increase in defect density N_{D} by a factor of 3, while irradiation with 10^5 pulses of $5 \text{ mJ/cm}^2/\text{pulse}$ caused an increase in N_{D} by a factor of 7. Thus, we see that the light induced defect creation efficiency per recombination event is higher for laser pulses than for CW light soaking. Recombination events during laser pulses are bimolecular and thus the energy released by recombination is higher than that under CW light, in which there is a significant recombination path through defects.

As we discussed, the results of this Chapter do not agree with the SJT model. In the light of our findings, one can exclude models for light-induced defect creation which are only based on photocarrier recombination. The reason for this, is that it is not possible to relate the rate of light induced defect creation, dN_{D}/dt , with the existing defect density N_{D} , through the lifetime of photocarriers, as in the SJT model.

A valid way of describing the light-induced defect creation might be the H-collision model [Branz 1997], discussed in §2.2.2, in which dN_{D}/dt is related to N_{D} via the mobile Hydrogen density. The decay of this density of mobile-H atoms is responsible for defect creation. The mathematical form describing the kinetics of defect creation in the H-collision model is very similar to that of the SJT model, but based on very a different microscopic mechanism, see §2.2.2, not directly related to photocarrier lifetime and recombination path.

4.4.4. Photoconductivity over a wide range of generation rates in a-Si:H

We already discussed in §4.4.1, that the different a-Si:H samples used in this study reach the same value of photoconductivity σ_{P} under high intensity laser pulses. The values of σ_{P} measured with low generation rate G in the same samples differ by a factor of 10^3 . Furthermore, increase in defect density affects strongly only the photoconductivity under low G and not that under high intensity laser pulses.

The two extremes in the value of G in the above argument are approximately $10^{18} \text{ cm}^{-3}\text{s}^{-1}$, used for low-light photoconductivity measurements, and $10^{28} \text{ cm}^{-3}\text{s}^{-1}$ for 30ns laser pulses. The bridging of the gap of ten orders of magnitude in G was accomplished by using filtered light from a Xe flash lamp. The measurement was performed by the Chicago group. The more complete picture of the function $\sigma_{\text{P}}(G)$, obtained this way, showed the transition from $\sigma_{\text{P}} \propto G^1$ at low G , to $\sigma_{\text{P}} \propto G^{1/2}$ at high G . The generation rate for which this transition occurs was found to increase with G , in agreement to our discussion in §4.4.2.

A numerical simulation, using the same code used by Tran in his work on Thermal Quenching in a-Si:H [Tran 1995], showed that one can fit the entire $\sigma_{\text{P}}(G)$ curve using values for the capture coefficients which were in good agreement with experiment [Stradins *et al.* 1996A, 1996B]. The part of the $\sigma_{\text{P}}(G)$ curve at the high G of laser

pulses could be fit very well even by setting $N_D=0$ in the simulation code, where N_D is the defect density. This once more shows that the photoconductivity at very high G is unaffected by defects.

4.4.5. Energy dissipation under high photocarrier densities – an open problem

We found that the majority of photocarrier density under the high intensity pulses, recombines during the pulse, with lifetime less than 10^{-10} s. A very important issue, related to this observation, is the energy dissipation during this very fast recombination process. One can immediately exclude the emission of radiation, because of the short lifetime observed, and because no photoluminescence is observed in a-Si:H at room temperature. Some possible mechanisms are Auger process, mobile-H excitation or emission of phonons in the amorphous lattice. In the Auger process the energy released in a recombination event is used to excite a carrier in a higher energy state. The released energy could also be used to excite H atoms in mobile states (related to H-collision model) or enhance diffusion of mobile-H in the material. However, this issue needs further investigation.

Chapter 5. Space charge effects in photoconducting a-Si:H

In §3.2.3 we presented how degradation by laser pulses affects the photoconductivity of a-Si:H, from 77K to 350K. We showed that the temperature of the onset of Thermal Quenching is shifted to lower values as the defect density is increased by light soaking.

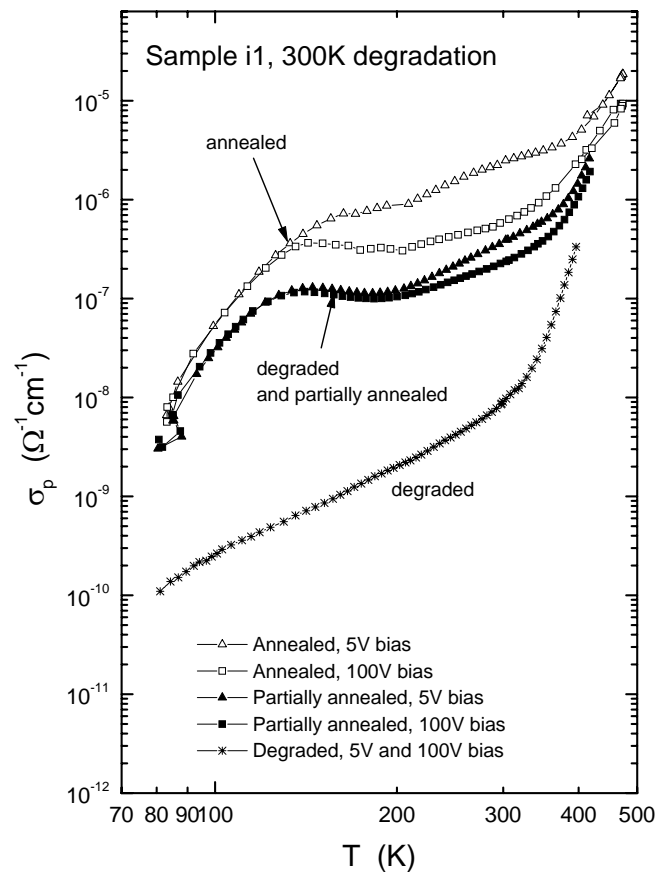


Figure 5.1. Photoconductivity σ_p of undoped sample i1, measured with 5V (triangles) and 100V (squares) bias voltage, in the fully annealed state (open symbols) and in a partially annealed state after degradation (solid symbols). The measurements with 5V and 100V bias coincide in the state degraded with 10^5 laser pulses (stars).

However, if one measures the dependence of photoconductivity σ_P on temperature T , using high bias voltage, one finds the surprising result demonstrated in Fig.5.1. The photoconductivity of sample i1 (see Appendix A for sample characteristics), measured with a bias voltage of 100V is different than that measured with 5V in the annealed state. This difference disappears in the degraded state, as one can see in Fig.5.1, and gradually re-appears in the partially annealed sample. The effect of the dependence of σ_P on bias voltage V_b arises from a non-linear dependence of photocurrent on bias V_b , i.e. non-Ohmic behavior. This non-Ohmic behavior has never before been observed in a-Si:H. One can see in Fig.5.1 that the effect is sensitive to the defect density of the sample.

The study of the effect of non-Ohmicity in a-Si:H is the topic of this Chapter. Section 5.1 provides an introduction related to the quantity of interest, i.e. the photoconductivity of a-Si:H, and its relation to the material parameters as well as the metal contacts used for measurements.

5.1. Introduction

5.1.1 Photoconductivity in a-Si:H: The photoconductivity of Hydrogenated Amorphous Silicon was briefly discussed in §1.3. The basic assumption underlying the discussion and the equations presented there, is that the metal contacts supply carriers of both signs to the material, so that charge neutrality is maintained and the photocurrent is proportional to the applied electric field. This is the so-called secondary photoconductivity, in contrast to the case of primary photoconductivity in which no carriers enter the semiconductor from the metal contacts and one measures

only the carriers generated by the light in the material. An example of primary photoconductivity is the time-of-flight (TOF) experiment.

A large body of experimental work on a-Si:H photoconductivity is based on the assumption of charge neutrality. However, we will show that under conditions frequently met in these experiments, this assumption is not correct, space charge is present in the material and has significant effects on the transport properties.

5.1.2. Thermal and Infra-red quenching of photoconductivity: The temperature dependence of the photoconductivity of a-Si:H was discussed in §1.5. We will now describe the effect of infra-red quenching of photoconductivity in a-Si:H, in the basis of the ideas of Chapter 1 on thermal quenching (TQ).

The basic result on TQ which we will need in later discussion in this Chapter, is the condition for the onset of TQ, namely eq.(1.4). The onset of TQ is shifted to lower temperatures when a positive charge is added in the sample by p-type doping. However, as we shall see, a charge density Q can be present even in undoped samples. The study of the origin of this charge density, and its effect on transport is the object of this Chapter.

Infra red (IR) quenching of photoconductivity is the phenomenon of decrease of photoconductivity caused by bandgap light when infra red light is superimposed on the light incident in the material [Persans 1982] . This phenomenon is readily understood in terms of the above discussion on TQ. IR light enhances transfer of electrons from the N_{D^-} states to the conduction band, thus increasing the densities of N_{D0} , N_{D^+} states and enhancing recombination through these states. This means that when, under photoconductivity conditions, the majority of defects are D^- and the

sample is in a sensitized state [Rose 1963], addition of IR light will cause decrease of the photoconductivity by increasing the densities of D^0 , D^+ states which act as recombination centers for electrons.

5.1.3. Metal-semiconductor transport: In the previous section we briefly discussed the effect of the charge state of dangling bonds on the photoconductivity of a-Si:H. This charge state can change with thermal or optical detrapping of carriers, i.e. thermal and infra red quenching. The charge state and the recombination properties can also change, as we will see later, in regions of the sample, adjacent to contacts, where space charge is induced for any reason. It is helpful to briefly discuss the basic features of metal-semiconductor transport, which we will use in the discussion of space charge creation in a-Si:H.

The basic mechanisms of carrier transport in metal-semiconductor contacts are shown in Fig.5.2. A potential difference is applied between the two metal contacts, in a typical photoconductivity measurement. C denotes the Cathode, i.e. the metal contact kept at lower voltage than the Anode A. The valence and conduction bands of the semiconductor near the contact may or may not bend, depending on the existence or absence of charge at the interface. In Fig.5.2 we assume band bending only at the cathode-semiconductor interface.

The transport mechanisms in the metal-semiconductor interface are

- thermionic emission of carriers from the metal to the semiconductor, process I & VI
- tunneling of carriers through the gap to conducting states, process II & V

- extraction of carriers from the semiconductor to the metal, process III & IV.

At very low temperatures, e.g. liquid Helium 4.2K, only injection is important, i.e. processes III, IV. As the temperature increases, thermionic emission gradually dominates the current.

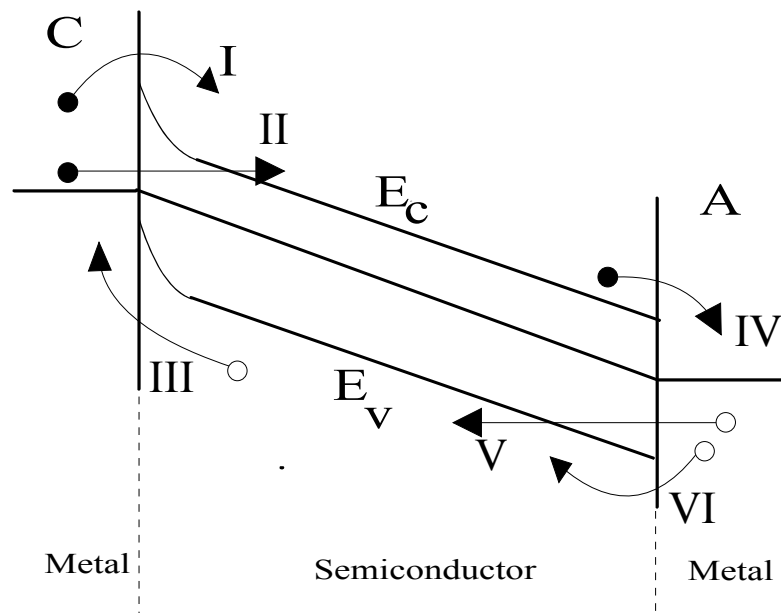


Figure 5.2. Metal-semiconductor carrier transport mechanisms. C denotes the cathode, i.e. metal contact kept at lower voltage than the anode A.

When the current drawn in the semiconductor is less than the current that contacts can supply, the contacts are Ohmic. Ohmic contacts keep the semiconductor neutral i.e. free of space charge. In the case of photoconductors, there is an additional requirement for a contact to be Ohmic, namely that the contact is able to supply the additional current needed when the semiconductor is made more conducting by light.

As mentioned above, thermionic emission is the dominant transport process in contacts at high temperatures. This means that the saturation of this process will determine the upper limit of the current available from the contact, i.e. the limit of Ohmic behavior. As pointed out by Rose [Rose 1963], thermionic emission may actually saturate, in which case the contact becomes effectively blocking. Under saturated thermionic emission the electric field in the sample is enhanced near the contact as compared to the rest of the sample in order to draw in more carriers and supply the photocurrent needed. This, in addition, means that the bands in the semiconductor near the metal contact will bend.

5.2. Appearance of space charge in photoconducting a-Si:H

The effects of thermal and infra-red quenching, described in the previous section, are studied assuming a neutral sample. In this section we will show that this assumption may not be true under certain conditions.

5.2.1. Potential profile across the photocurrent path: In a typical photoconductivity measurement, a voltage difference is applied between the two metal contacts. Thus, there is a variation of the potential V in the sample, in the direction x of photocurrent flow, the total potential difference throughout the sample being the voltage applied on the metal contacts. If this variation is linear with x , the

electric field $E = -\frac{\partial V}{\partial x}$ in the sample is constant, and there is zero charge density

$\rho \propto \frac{\partial^2 V}{\partial x^2} = 0$. If however, $V(x)$ is not linear, one has a non-zero space charge (SC)

density determined by Poisson's equation

$$\rho(x) = -\varepsilon_s \frac{\partial^2 V}{\partial x^2} \quad (5.1)$$

ε_s being the dielectric constant of the material.

We developed an experimental set-up in order to measure the potential profile along the photocurrent path. The measurement is based on the capacitive coupling between a thin insulated wire stretched on top of the sample perpendicular to the direction of photocurrent flow and a narrow strip of the sample just below the wire. With the help of a small AC modulation of the DC bias voltage, we probe the DC potential along the sample by measuring an AC signal picked-up by the wire which is proportional to the DC potential at the position of the wire. The details of the method are described in Appendix C.

The result for sample #1 (see Appendix A for sample characteristics) , illuminated uniformly with 650nm light, is shown in Fig.5.3. The measurement was performed at room temperature and the sample was in a well annealed state. V_{DC} denotes the bias voltage applied on the two metal contacts labeled A and B, see Appendix C.

One can see in Fig.5.3 that as V_{DC} increases above 20V, the voltage drop across the sample deviates from linearity. A large voltage drop develops near the negative electrode, i.e. electrode A for $V_{DC} > 0$ or electrode B for $V_{DC} < 0$. This large drop implies that the region near the cathode is more resistive than the rest (bulk) of the semiconductor. As $|V_{DC}|$ exceeds 20V only a small fraction of $|V_{DC}|$ appears along in the bulk, while the rest drops in the more resistive region near the cathode. Under these conditions one expects a non-linear dependence of photocurrent on applied voltage, i.e. non-Ohmic photocurrent versus bias Voltage curve.

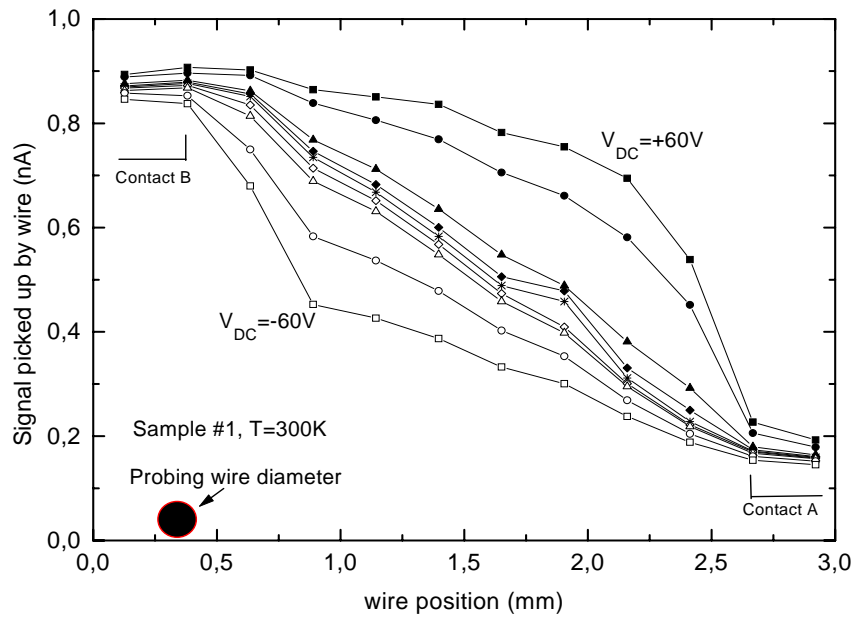


Figure 5.3. Potential profile along the photocurrent path for sample #1 (see Appendix A) at room temperature. Open symbols correspond to $V_{DC} < 0$, while filled symbols to $V_{DC} > 0$. The values of $|V_{DC}|$ were: 60V (squares), 40V (circles), 20V (triangles), 10V (rhombs) and 5V (stars). Light wavelength is 650nm.

The probing wire diameter is also shown in Fig.5.3. It is seen that the resolution of the measurement is not high enough to give accurate potential profile curves. However, the qualitative feature of the curves deviating from linearity in Fig.5.3 is clear.

From the relation of the potential in one dimension to the corresponding charge density, Poisson's eq. (5.1), the shape of the potential curves of Fig.5.3 indicates that there is a region of positive SC near the cathode, when the DC voltage exceeds approximately 20V in sample #1. The origin of this SC density, observed for the first time, will be discussed in a later section. As we will see, SC is always present in photoconducting a-Si:H, but it has significant effect on the transport properties only at the temperature region of Thermal Quenching and at high bias voltages.

5.2.2. Effect of space charge on the temperature dependence of photoconductivity : In the previous paragraph we argued that when the bias voltage,

applied on undoped sample #1, exceeds 20V, a region of positive space charge is observed near the cathode. In §1.5 we discussed how a charge density Q (see eq.(1.4)) affects the thermal behavior of the photoconductivity. One might expect that the charge density Q of eq.(1.4), can be the charge density which is observed near the cathode at high bias voltages, in undoped samples. Thus, one might expect a different thermal behavior of photoconductivity, measured with low and high bias voltage V_b , under the same illumination conditions. In the low V_b case there is no effect of SC on the photoconductivity, while at high V_b the SC manifests itself by the large voltage drop in the region near the cathode.

In Fig.5.4 we show the photoconductivity σ_p of sample #1, measured with different bias voltages. The sample was in a well annealed state, and the photoconductivity was measured under 650nm light illumination with generation rate $G=6 \times 10^{19} \text{ cm}^{-3} \text{ s}^{-1}$.

Dependence of σ_p on bias voltage V_b appears in the T-range between 130K and 320K. In this range, lower values of V_b give higher values of σ_p , which means that the dependence of photocurrent i_p on V_b is sublinear. At temperatures lower than 130K and higher than 320K all curves lie on top of each other, which means that $i_p(V_b)$ is linear.

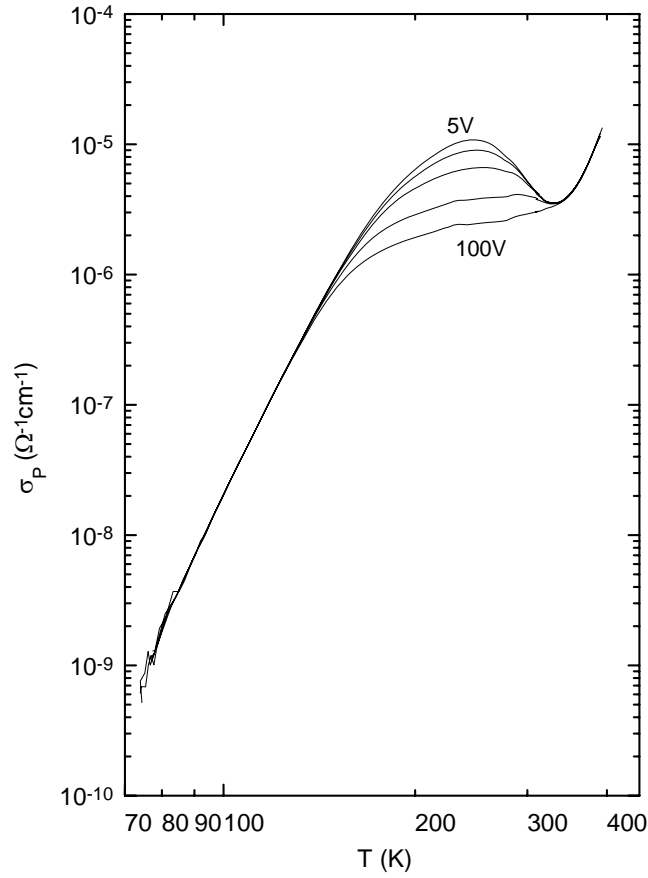


Figure 5.4: Photoconductivity σ_p versus temperature T measured with various bias voltages on sample #1, in well annealed state, under bandgap light illumination with $G=6 \times 10^{19} \text{ cm}^{-3} \text{ s}^{-1}$ (see text).

It is clear that the space charge density near the cathode has significant effect on the photoconductivity of the sample in the temperature region of thermal quenching. As discussed in §1.5, thermal quenching is initiated when the trapped hole density drops to $2N_D + Q$ (eq.(1.4)), N_D being the defect density. For an undoped sample, the charge density added by dopants is zero, but there is a positive charge created near the cathode, as was shown in §5.2.1, which is the density Q in this case. This means that the onset of thermal quenching is shifted to lower temperatures, and thus the

photoconductivity decreases at constant T . This is the origin of the higher resistance of the SC region, relative to the bulk of the semiconductor.

This effect is seen in Fig.5.4, where increase in V_b causes a decrease in photoconductivity in the thermal quenching region.

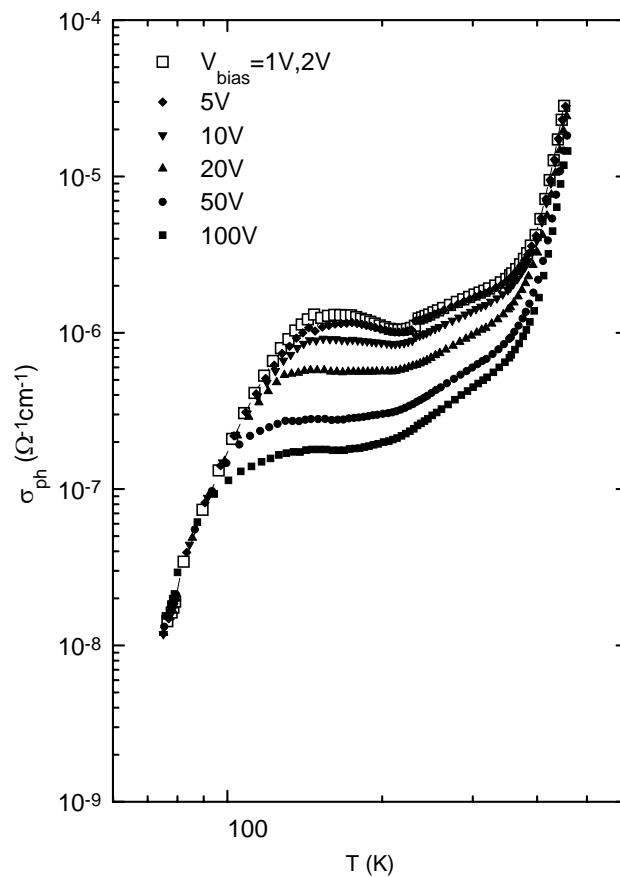


Figure 5.5: Photoconductivity vs temperature of sample #2 (see Appendix A) in a well annealed state, under illumination with bandgap light. $G=2 \times 10^{18} \text{ cm}^{-3} \text{ s}^{-1}$.

Figure 5.5 shows the $\sigma_p(T)$ curves measured at different bias voltages in sample #2 in well annealed state, illuminated with 650nm light with $G=2 \times 10^{18} \text{ cm}^{-3} \text{ s}^{-1}$. The lower

voltages used in this case were 1V, 2V, as shown in the graph. The σ_p curves for $V_b=1V, 2V$ fall on top of each other in the whole T-range of the measurement. Deviation from Ohmicity is clear for $V_b \geq 10V$ and sets in at $T=100K$. The high V_b curves merge at $T \geq 350K$.

5.2.3. Origin of SC near cathode: In this paragraph we present a model for the creation of the positive SC region in photoconducting a-Si:H. We briefly discuss the effects of this SC density on the transport properties. In a later section we present the quantitative features of numeric calculations of non-Ohmic transport, due to the space charge region near the cathode.

Let us consider first very low (liquid Helium) temperature T. As pointed out in §5.1.3, at this T no charges enter the semiconductor from the metal contacts. If one applies an electric field E on the material, current continuity is maintained by an outflow of holes to the cathode and an outflow of electrons to the anode, i.e.

$$\sigma_h E_C = (\sigma_e + \sigma_h) E_B = \sigma_e E_A, \quad (5.2)$$

where E_C, E_B, E_A denote the electric field near the cathode, in the bulk and near the anode respectively and σ_e, σ_h the electron and hole photoconductivities. In a-Si:H one has $\sigma_e > \sigma_h$, which from eq.(5.2) gives $E_C > E_A > E_B$, a situation shown schematically in Fig.5.6. The steepening on the bands near the cathode causes electron depletion and hole accumulation there, which is the origin of positive SC in this region. This argument holds for low T, thus we presume that SC is present at these Temperatures and hides in Ohmic I-Vs. Space charges at 4.2K were indeed observed by Heck *et al.* [Heck *et al.* 1997]. Although SC is present at low T, Ohmicity is not destroyed because at 4.2K the photoconductivity is not changed by the net positive charge

density. However, as T approaches T_Q the occupations of gap states become very sensitive to the appearance of a space charge density Q , as discussed in §1.5. The occupations of gap states determine the transport properties, i.e. as T approaches T_Q the photoconductivity becomes sensitive to SC, and non-Ohmic effects appear. In a following section, we will demonstrate how the sensitivity of photoconductivity to an increase in positive charge will result in non-Ohmic behavior.

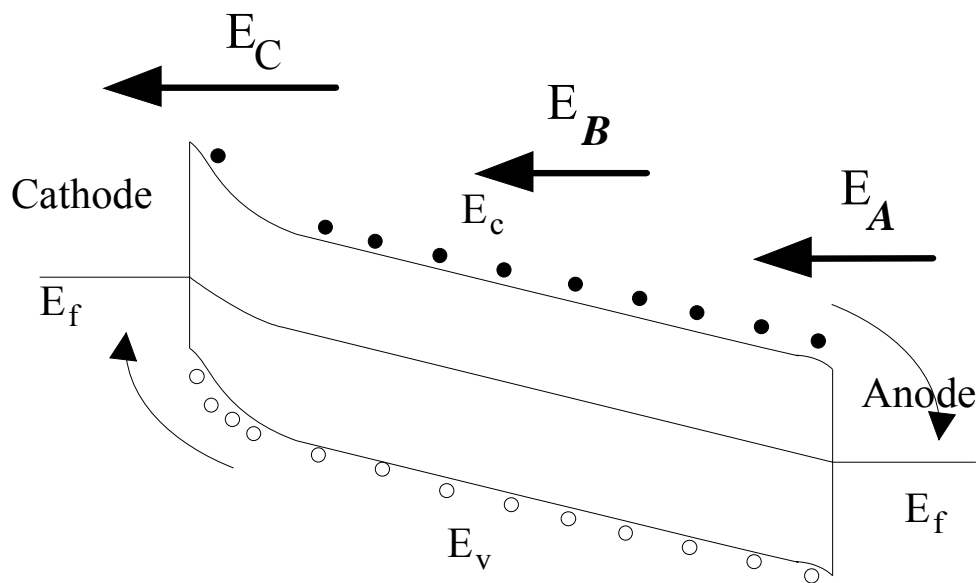


Figure 5.6. Band diagram demonstrating the fields involved in eq.(5.2) of text.

In the discussion so far, thermionic emission of carriers from the metal contacts to the semiconductor (process I, VI of Fig.5.2) is neglected. One can include thermionic emission in the above argument as follows. As pointed out by Rose [Rose 1963], thermionic emission saturates at high electric fields, causing steepening of the bands near the contact, in order to draw the additional current needed under photoconductivity conditions. Taking into account that the photoconductivity of a-Si:H is mainly due to electrons, the steepening will occur near the cathode, and again positive charge will accumulate there. As T increases, thermionic emission can

supply the photocurrent needed. Both charge neutrality and Ohmicity are restored, in agreement with the results of §5.2.2.

We must note here that we did not make any assumption regarding the nature of the states creating the SC, in the gap of a-Si:H. These states may be D^0 or D^+ states, or holes trapped deep in the valence band tail. Both result in decrease in photocarrier lifetime in sensitized a-Si:H.

5.3. Effects of cathode SC on the transport properties

5.3.1. I-V curves: In the previous paragraph we have shown that there is a temperature range in which deviations from Ohmicity appear. We now focus our attention at this particular temperature range. Fig.5.7 shows the dependence of photocurrent i_p of sample #1 on applied voltage V_b at constant temperature $T=190K$. This temperature is in the range of deviation from Ohmicity, as shown in Fig.5.4. The light wavelength is again 650nm.

The curve is linear at low voltages, $-15V < V_b < 15V$, and sublinear at higher $|V_b|$. This means that the corresponding photoconductivity σ_p will be independent of V_b for $|V_b| < 15V$, and will decrease with increasing $|V_b|$ above 15V.

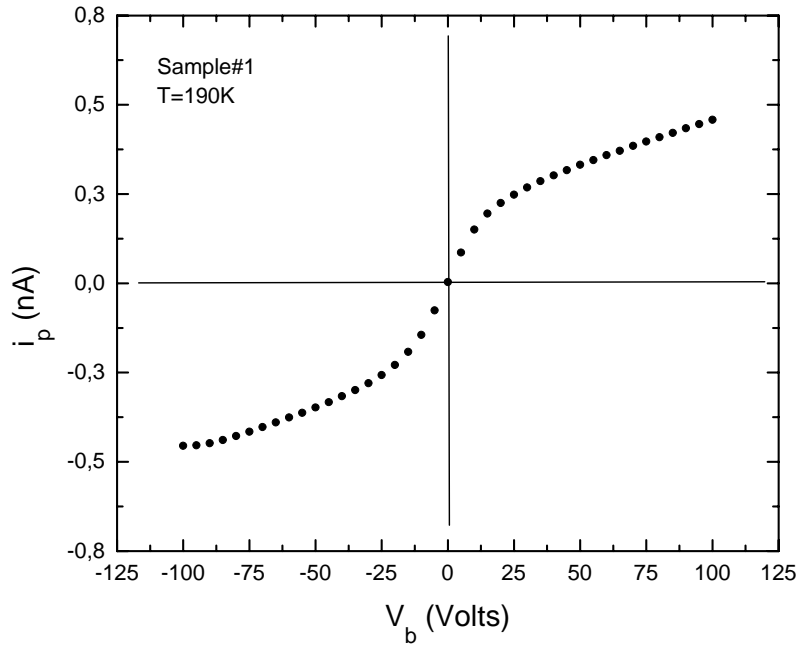


Figure 5.7. Photocurrent i_p of sample #1 vs bias voltage V_b at the constant temperature $T=190\text{K}$ of maximum deviation from Ohmicity.

In order to compare $i_p(V_b)$ curves at different generation rates G it is convenient to use logarithmic axes in the i_p - V_b plot. Fig.5.8 shows photocurrent i_p versus bias voltage V_b curves for sample #1 at $T=190\text{K}$ for various generation rates of bandgap light illumination. The solid lines, drawn for reference with slope 1 in the log-log plot, indicate a linear function i.e. Ohmic behavior. It is surprising to see that, despite the large range of light intensities used, the dependence of the photocurrent on V_b is almost identical at all generation rates. There are clearly two regions: ohmic at low voltage and subohmic at high with a clear transition in between. One can see that the transition voltage, the onset of non-ohmic behavior, increases slightly with increasing G .

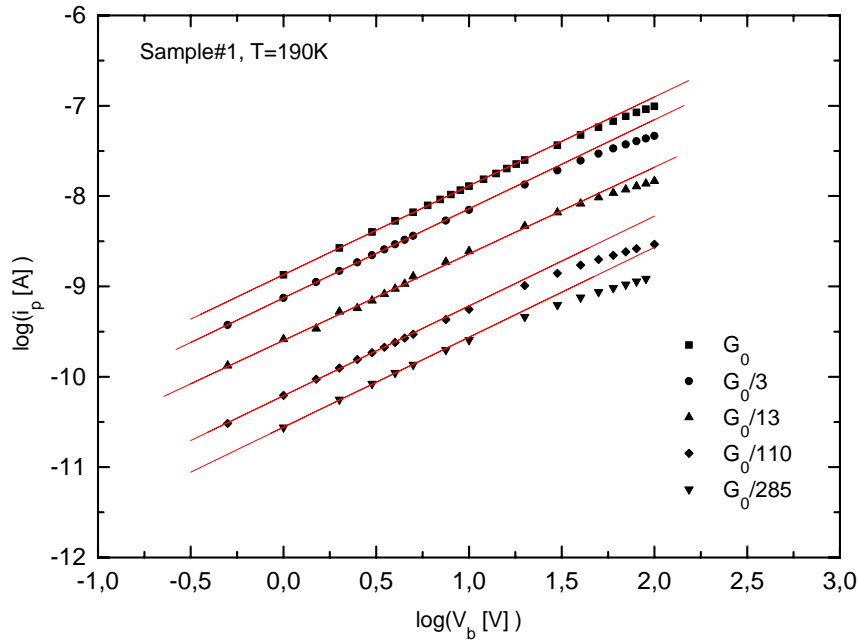


Figure 5.8. I_p vs V_b curves for sample #1 at 190K. The generation rate G_0 of bandgap light is $3.75 \times 10^{17} \text{ cm}^{-3} \text{ s}^{-1}$. The lines indicate slope 1 in the log-log plot.

5.3.2. Effects of IR illumination: In §5.1.2 we briefly discussed the phenomenon of IR quenching. In the state of IR quenching the IR light creates D^0 , D^+ states, by exciting holes from deep valence band tail states and subsequent capture of these holes by D^- or D^0 states. Thus, the sample becomes less sensitive to positive charge density Q , because significant positive charge is already present in the defect band.

According to the above argument, one expects that the SC effects should become weaker if, in addition to the bandgap light, the sample is illuminated with IR light.

In order to test this prediction, we have measured the potential profile across the photocurrent path, using the same sample and under precisely the same conditions as for the measurement described in §5.2.1, with additional IR light at wavelengths $\lambda \geq 850 \text{ nm}$.

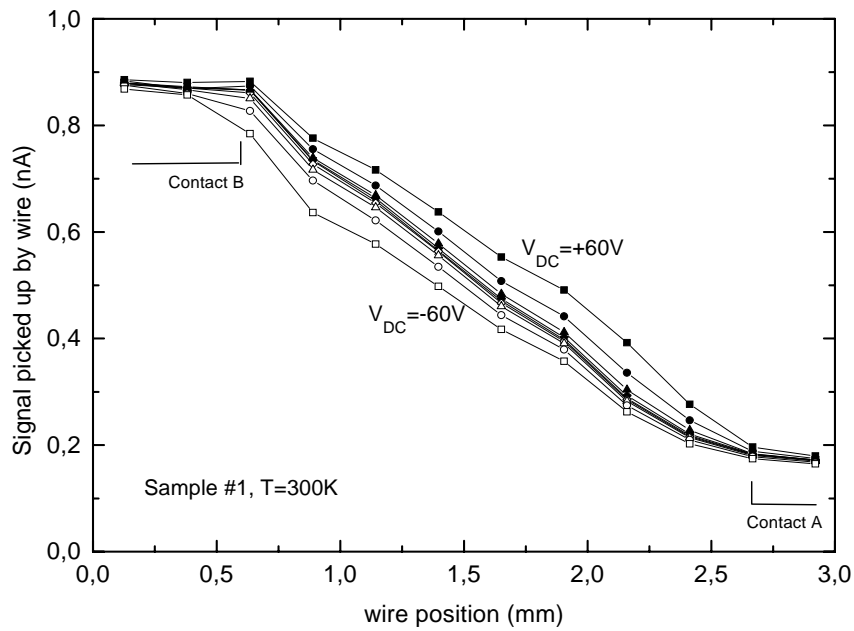


Figure 5.9. Same as Figure 5.3, but now the sample is illuminated with combined 650nm light (same as that of Fig.5.3) and broadband infra red light at wavelengths $> 850\text{nm}$.

The result is shown in Fig.5.9. Comparing this result to that of Fig.5.3 of §5.2.1, one can see that the addition of IR light almost cancels the effects of SC on the potential profile.

We then explored the effect of addition of IR light on the photocurrent dependence on bias voltage. The result for sample #1 is shown in Fig.5.10. One can see that the addition of IR light completely restores Ohmic behavior, for the voltage range studied.

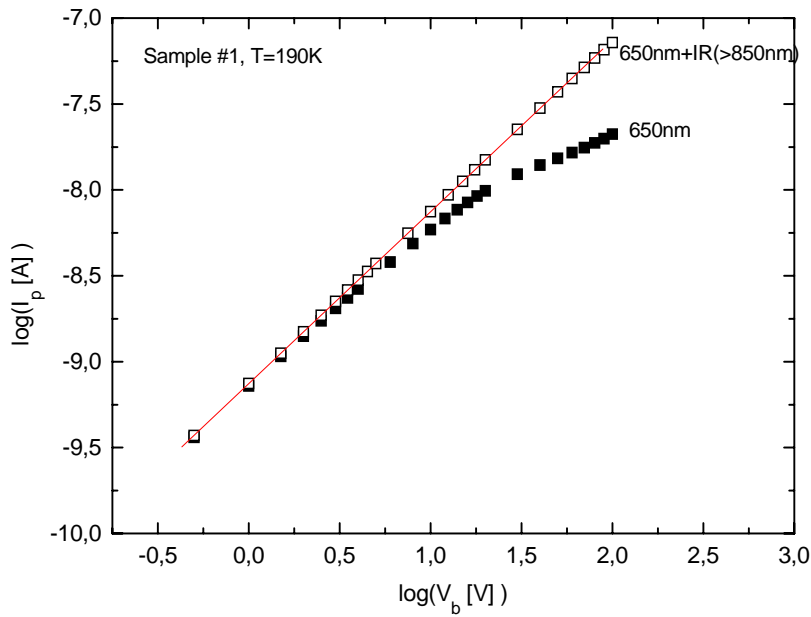


Figure 5.10. I_p vs V_b for sample #1 at 190K. Sample was illuminated with 650nm light (solid symbols) and with the same 650nm light plus infra red light at wavelengths >850 nm (open symbols). Line indicates slope 1.

In all measurements presented in this Chapter so far, the bandgap, subgap or combined light on the sample was uniform. We have also measured I-V curves under uniform bandgap light and superimposed infra-red light illuminating only half of the sample near one of the metal contacts, in order to cross check the finding that the SC is created near one of the contacts, namely the cathode. The measurement was performed on sample #1 at $T=300$ K. The infra red light illuminates the sample near the contact on which the voltage is applied. The result is shown in Figure 5.11. For comparison, we also plot the I-V curve with bandgap light only. One can see that when V_b is positive there is a minor effect on the I-V curve which remains clearly subohmic. If however V_b is negative, proportionality of photocurrent with bias

voltage is restored. This confirms that the SC region, which is largely affected by the IR light, is located near the negative metal contact.

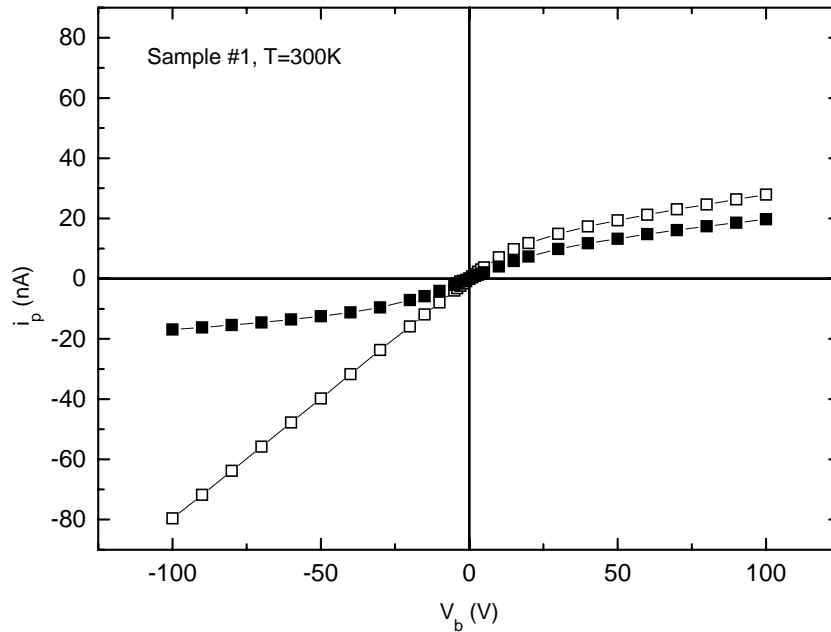


Figure 5.11. I-V measurement on sample #1 at 300K. The filled symbols correspond to uniform 650nm light. Open symbols correspond to the same bandgap light with additional broadband IR ($\lambda \geq 850\text{nm}$) only near the contact on which V_b is applied.

5.3.3. Effects of space charge on photoconductivity at various light wavelengths:

We have presented so far results on SC creation under illumination with bandgap light (650nm), or bandgap light with superimposed subgap (infra-red) light.

Let us examine the appearance of non-Ohmic effects as a function of the wavelength of the light illuminating the sample. The wavelengths used were 650nm (bandgap), 800nm ($h\nu=1.53\text{eV}$, subgap), 900nm ($h\nu=1.36\text{eV}$, subgap).

In order to compare the transport properties under illumination with different wavelengths, we have adjusted the light intensity for each wavelength in order to obtain the same photocurrent at low bias voltage, i.e. same photocurrent in the Ohmic voltage range. This means that, for the three wavelengths used, the free electron density in the conduction band was the same. The difference for the three wavelengths is that under bandgap light illumination, the free carriers originate from electron-hole pair generation in the bands, while under subgap illumination the free carriers originate from localized states inside the gap. This, in turn, means that under subgap light illumination, the occupation of deep gap states is not determined solely by trapping of carriers from extended states. One must also take into account the transitions from localized to extended states with the absorption of a subgap photon. As a consequence, the states inside the gap cannot be fully occupied under subgap light illumination, and the sample will not be as sensitive to positive charge as it is under illumination with bandgap light.

Fig.5.12 shows Photo-IV curves for three wavelengths. Sample #1 in well annealed state at 190K is used. One can see that under subgap illumination, the non-Ohmic effects appear at higher bias voltage than under 650nm illumination.

In order to fully understand these effects, let us assume that the states creating the positive SC are holes trapped deep in the valence band tail. If electrons are transferred from these states to the conduction band with the absorption of subgap photons, one has a state of the sample less sensitive to SC, because many unoccupied, i.e. occupied by holes, states are present. Under illumination with 900nm light, transitions from deeper gap states are enhanced, and the sample becomes less sensitive to SC than in

the state under 800nm illumination. This is seen in Fig.5.12. Under 900nm illumination, sub-Ohmicity is hardly observed at the voltage range studied. Under 800nm illumination, sub-Ohmicity appears, but sets in at higher voltage than that under bandgap, 650nm, illumination.

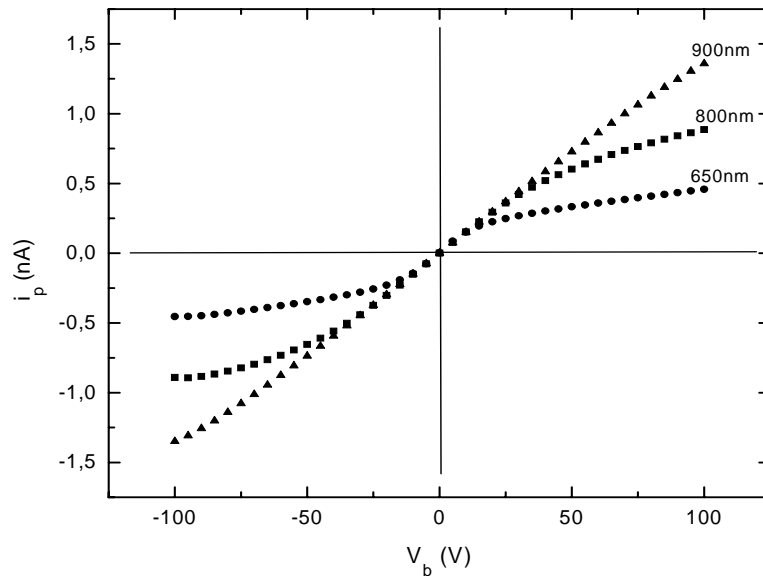


Figure 5.12. I_p vs V_b curves for sample#1 at 190K, under monochromatic light illumination of different wavelengths, 650nm, 800nm and 900nm. The light intensities were chosen to give the same photocurrent at low voltages.

5.3.4. Light degradation effects: When the sample defect density N_D is increased by light soaking, the photoconductivity becomes less sensitive to positive charge, because of the large number of defects present, see eq.(1.4) of §1.5, in which N_D increases and thus the effect of Q becomes weaker.

In Fig.5.13 we plot the photoconductivity of sample #1 in a moderately degraded state, under 650nm illumination, same as that of Fig.5.4 of §5.2.2. For comparison, we also plot the same curves for the annealed state of the sample, i.e. the curves of

Fig.5.4. One can clearly see that in the degraded state, the non-Ohmic effects are weaker, as discussed above.

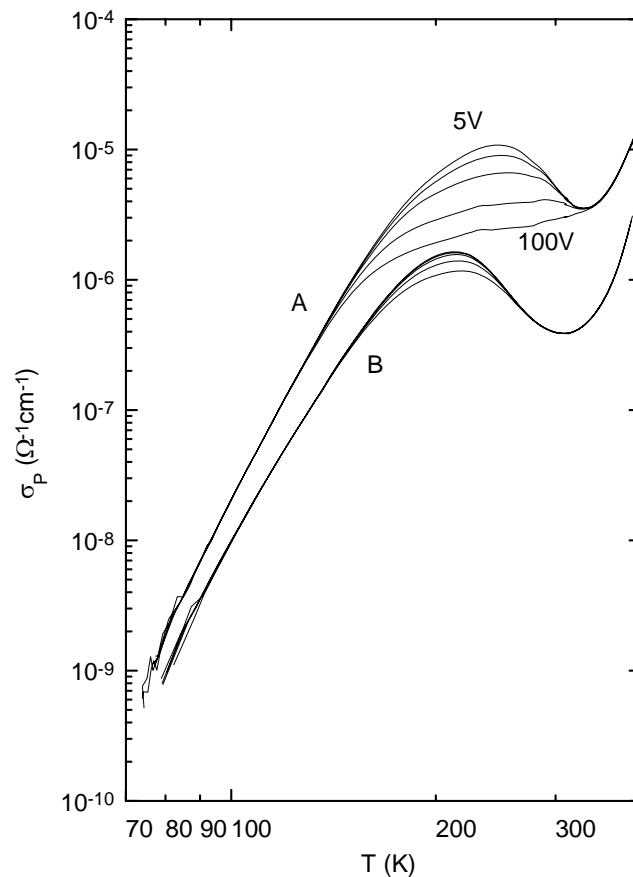


Figure 5.13: Photoconductivity vs Temperature for sample #1, under bandgap light illumination with $G=6 \times 10^{19} \text{cm}^{-3} \text{s}^{-1}$. Annealed state of the sample is denoted A, and moderately degraded is denoted B.

We observed that degradation induced by light soaking shifts the onset of non-Ohmicity to higher bias voltages. Increase in defect density by less than 50% of its native value restores almost completely the linearity in i_p - V_b curve up to $V_b=100\text{V}$. This is shown in Fig.5.14 for sample #1 at 190K. The open symbols designate state A of minimum defect density N_{D0} . Solid symbols correspond to light soaked state with

defect density approximately $1.5N_{D0}$. Defect density of soaked state was measured by CPM, described in Chapter 1.

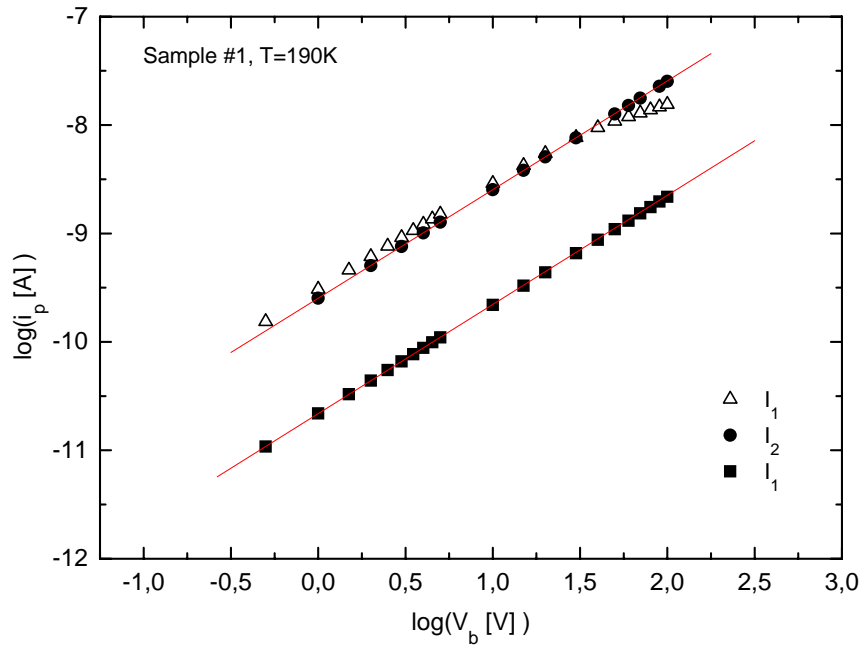


Figure 5.14. I_p vs V_b for sample #1 at 190K. Open symbols correspond to the annealed state of the sample, while solid symbols to a degraded state with 50% more defects. The triangles and squares correspond to the same 650nm light intensity I_1 , before and after degradation. I_2 was chosen for the degraded state to give the same i_p at low voltages as the annealed state. Lines indicate slope 1.

One can see the drop in photocurrent under illumination with light intensity I_1 , from state A to the light soaked state. While subohmicity is apparent in state A, the degraded state is completely ohmic in the whole voltage range, for the same light intensity I_1 . Then, in the degraded state, the 650nm light intensity was increased from I_1 to I_2 , in order to have the same photocurrent at low V_b , as that in the annealed state. One can see that the degraded state does not deviate from Ohmicity even for voltages for which subohmicity is clear in state A.

5.4. Modeling of space charge density near the cathode

In the discussion of §5.2.3 we demonstrated how a SC region is created near the cathode in a-Si:H. An issue which was not discussed in §5.2.3 how the appearance of non-Ohmic effects arise from the sensitivity of photoconductivity to positive charge.

It is helpful to think of the SC creation in a-Si:H in the following way. The difference in electron and hole photoconductivities cause steepening of the bands in the semiconductor near the cathode at low T, as described in eq.(5.2) of §5.2.3. This causes positive charge to accumulate near the cathode. This SC region has higher resistance, thus a large voltage drop appears in it and consequently the positive charge increases. According to this argument, once a small bending of the bands appears, the SC region will be created and will extend in the photoconductor causing non-Ohmic effects. This bending, which in a sense initiates the phenomenon, was described in §5.2.3. In this paragraph we present a model which describes how the sensitivity of photoconductivity on positive charge increases the width of the SC region and creates non-Ohmic effects.

5.4.1. The model:

Let us consider a sample with photoconductivity σ . We use σ for photoconductivity instead of the usual σ_p for simplicity in the equations which will be presented in the following. An electric field E in the x -direction forces a current density J to flow through the sample. Current continuity reads

$J = \sigma E = \text{const}$ (independent of x). Differentiating this one gets:

$$\frac{d\sigma}{dx} E + \sigma \frac{dE}{dx} = 0 \quad (5.3).$$

If we assume a charge density $\rho(x)$ to be present in the sample, Poisson's equation reads

$$\frac{dE}{dx} = \frac{\rho}{\epsilon_s}, \quad (5.4),$$

where ϵ_s is the dielectric constant of the material.

From (5.3) and (5.4) one gets

$$\frac{d\sigma}{dx} E = -\sigma \frac{dE}{dx}. \quad (5.5)$$

At this point we assume that σ varies with x only because there is a charge density ρ which changes with x . This means that the photoconductivity is a function of charge density only. We thus write

$$\frac{d\sigma}{dx} = \frac{d\sigma}{d\rho} \frac{d\rho}{dx} \text{ and eq.(5.5) becomes}$$

$$E \frac{d\sigma}{d\rho} \frac{d\rho}{dx} = -\sigma \frac{dE}{dx} \text{ which, by substituting } \frac{d\rho}{dx} \text{ from Poisson's equation, can also be}$$

written as

$$\left(\epsilon_s \frac{d \ln \sigma}{d\rho} \right) E \frac{d^2 E}{dx^2} = -\frac{dE}{dx}. \quad (5.6)$$

Equation (5.6) can be solved to give $E(x)$ in the sample, provided one assumes a functional dependence of the photoconductivity on positive charge density. If $E(x)$ is known, one can find the charge density $\rho(x)$ from Poisson's equation (5.4). One can then also find the potential $V(x)$ across the direction x of photocurrent flow by a simple integration.

Thus, within the framework of this model, one needs a functional form for $\frac{d \ln \sigma}{d\rho}$.

The simplest choice is to take this derivative to be constant. We write this constant as

$$\frac{d \ln \sigma}{d \rho} = -\frac{1}{q_e N_0},$$

where q_e is the absolute value of the electron charge and the minus sign denotes that the photoconductivity decreases with increasing positive charge density. N_0 denotes the number density of positive charges that cause a decrease in σ by a factor of $e=2.72$. It is obvious that the lower the value of N_0 , the more sensitive the photoconductivity on positive charge. In the following we take two different values for the sensitivity, namely $N_0=10^{13} \text{ cm}^{-3}$ and $N_0=10^{15} \text{ cm}^{-3}$.

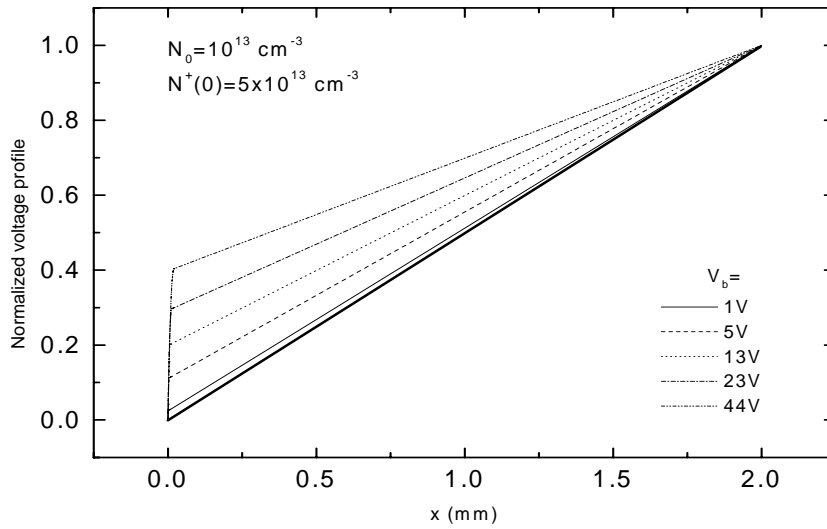


Figure 5.15. Calculated potential in the case of high sensitivity, $N_0=10^{13} \text{ cm}^{-3}$. The curves are normalized to unity, and the total potential drop V_b across the 2mm sample is given separately. The cathode-semiconductor interface is at $x=0$.

5.4.2. Results of the model:

In order to solve eq.(5.6) numerically, we have assumed a space charge (SC) density at $x=0$, which it taken to be the semiconductor-cathode interface. This charge density, denoted $N^+(0)$, serves as a boundary condition for integrating eq.(5.6) across the direction x from $x=0$ to $x=2\text{mm}$. The second condition needed for the integration of eq.(5.6) is the value of the electric field E at $x=0$, which represents the electric field at

the semiconductor-cathode interface. Thus, one starts with $N^+(0)$ and $E(0)$ and integrates eq.(5.6) from $x=0$ to $x=2\text{mm}$, to calculate the SC density $N^+(x)$ and the potential $V(x)$.

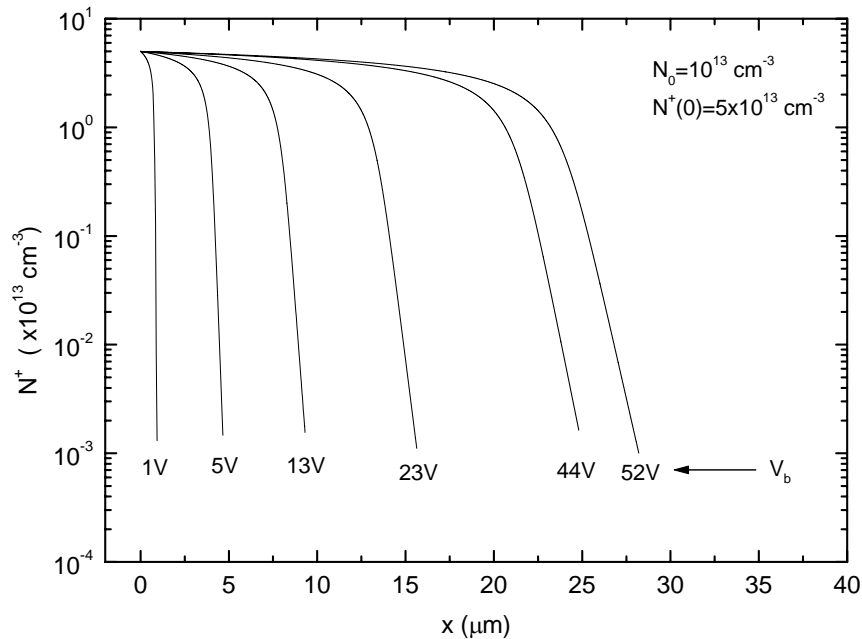


Figure 5.16. Space charge number density N^+ as a function of distance across the photocurrent path, for the low sensitivity case. The values of V_b correspond to the ones presented in fig.5.15. The cathode-semiconductor interface is at $x=0$.

High sensitivity, $N_0=10^{13} \text{ cm}^{-3}$: Fig.5.15 shows calculated voltage profiles $V(x)$, for a sample having 2mm spacing between metal contacts. All curves in Fig.5.15 are normalized to unity and the actual value of the voltage drop V_b across the 2mm sample is shown in the legend. One can see that as V_b is increased, a larger percentage of V_b appears in the region near the cathode. As one can see in Fig.5.15, the SC region near the cathode is very narrow, compared to the 2mm sample width. This is also shown in Fig.5.16, where the number density of positive space charge $N^+(x)$ is

plotted. One can see that the SC region is of the order of ten microns, for this particular choice of the sensitivity N_0 . This region increases with increasing V_b as one can see in Fig.5.16.

Low sensitivity, $N_0=10^{15} \text{ cm}^{-3}$: Increasing our choice of N_0 , thus assuming lower sensitivity of the sample to positive charge, results in much weaker effects of SC on the voltage profile $V(x)$. This is shown in Figs.5.17 and 5.18, where $V(x)$ is plotted for two values of the density $N^+(0)$. One can see that in this case, the voltage drop in the SC region is very low, as compared to that of fig.5.15, even if $N^+(0)$ is increased (fig.5.18). The voltage drop in the SC region is low because it extends only a few microns in the sample. This is demonstrated in fig.5.19, where $N^+(x)$ is plotted for the low sensitivity case $N_0=10^{15} \text{ cm}^{-3}$.

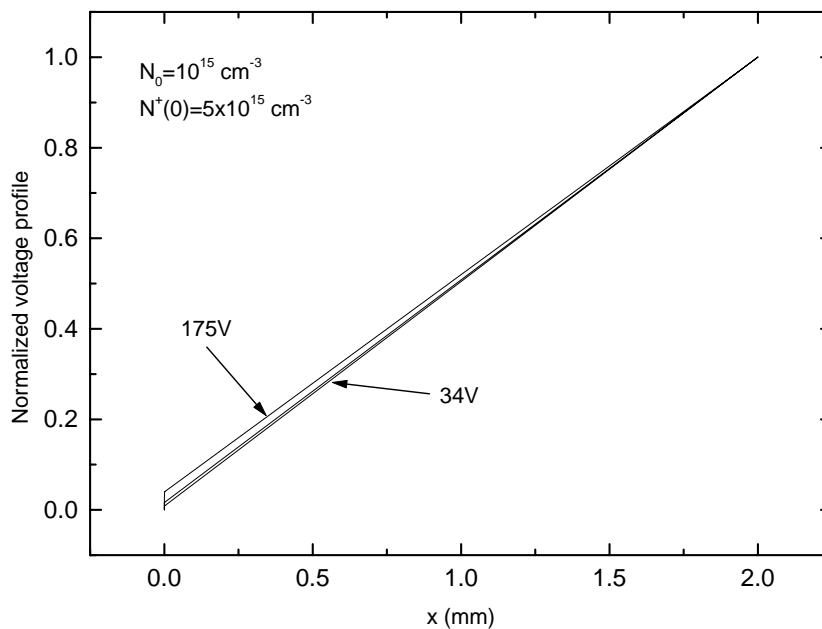


Figure 5.17. Calculated potential curves across the photocurrent path, for the low sensitivity case $N_0=10^{15} \text{ cm}^{-3}$. The curves are normalized to unity and the total potential drop across the 2mm sample is given separately. The cathode-semiconductor interface is at $x=0$.

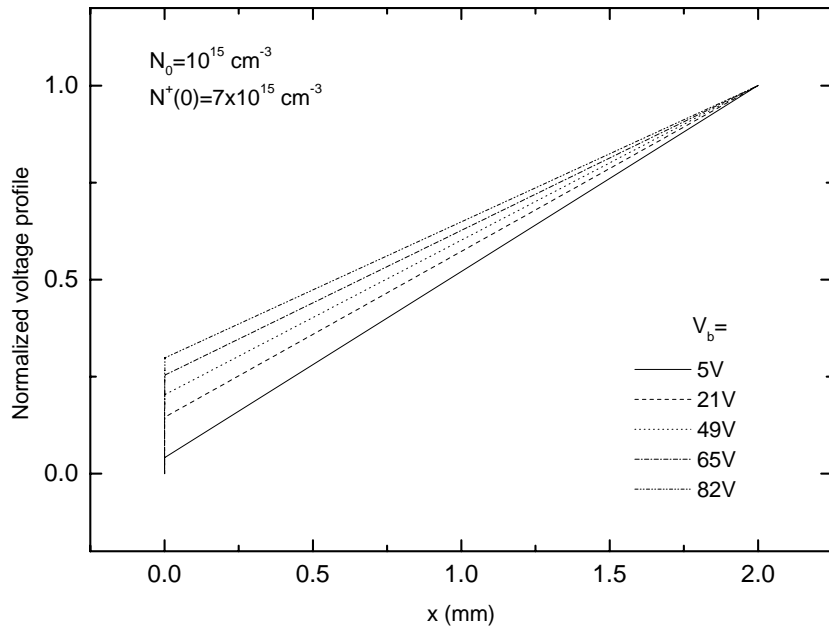


Figure 5.18. Same as in Fig.5.17, but for larger charge density $N^+(0)$.

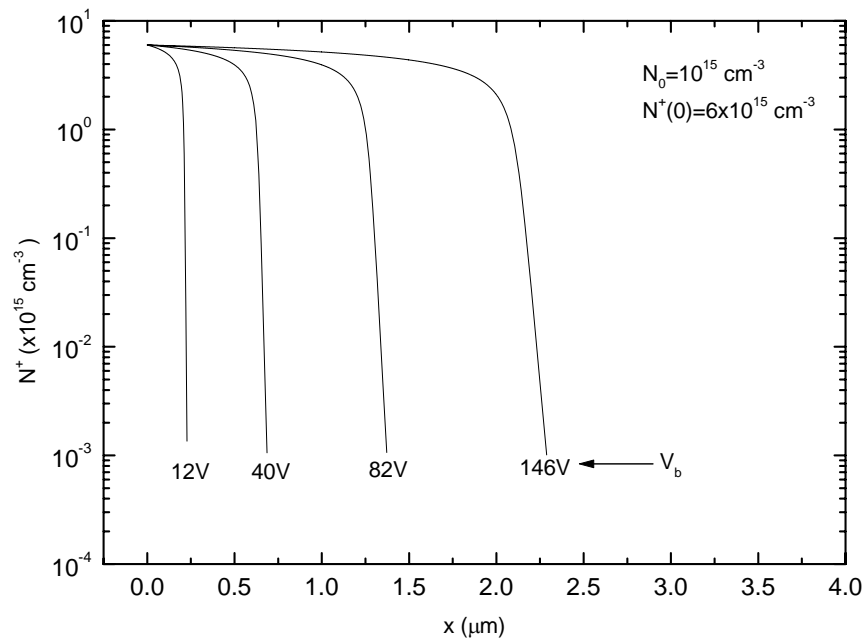


Figure 5.19. Calculated SC number density N^+ as a function of distance across the photocurrent path in the low sensitivity case. $x=0$ is the semiconductor-cathode interface.

5.4.3. Discussion:

First, we note once again that the model presented is based on the assumption that the photoconductivity σ varies with distance x only through the dependence $\sigma(\rho)$, where ρ is the space charge density. This assumption is reasonable for a homogenous sample under uniform illumination. Then, one needs the specific functional dependence of σ on ρ , in order to solve eq.(4). We take $\frac{d \ln \sigma}{d \rho} = \text{const.} = -\frac{1}{q_e N_0}$. N_0 is the number density of positive space charge density needed to reduce the photoconductivity by a factor $e=2.72$, which is a measure of the sensitivity of the photoconductivity to positive charge.

From the calculated $V(x)$ curves of figs.5.15, 5.17, 5.19 we see that in order to have a significant voltage drop in the SC region, as observed experimentally, the sensitivity of the sample must be surprisingly high, i.e. N_0 low. If we assume that the SC density ρ is created by the defect states in the band gap of a-Si:H, a choice of $N_0=10^{13} \text{cm}^{-3}$ means that if 0.5% of the defects become positively charged, the photoconductivity will drop by a factor of 2.7. This notion holds for a high quality sample with native defect density of the order of $5 \times 10^{15} \text{cm}^{-3}$. The appearance of a large voltage drop in the case of high sensitivity can be understood as follows. When the charge density is low, $5 \times 10^{13} \text{cm}^{-3}$ in figs.5.15, 5.16, the SC region extends over some tens of microns in the sample, see fig.5.16. The voltage drop in this region is a significant fraction of the total potential difference V_b across the 2mm sample. When the sensitivity is decreased, i.e. $N_0=10^{15} \text{cm}^{-3}$, the space charge density needed to affect the photoconductivity is high, $(5-7) \times 10^{15} \text{cm}^{-3}$ in figs.5.17, 5.18, 5.19. This high charge

density extends only a few microns in the sample, and thus there is no large voltage drop across this narrow SC region. The same total charge produces larger voltage drop across it when extending deeper into the semiconductor.

So far, the temperature T does not enter in our model. However, one can incorporate the effects of T implicitly as follows. In our discussion of Thermal Quenching (TQ) in §1.5, we noted that in the temperature region of TQ the sample is very sensitive to positive charge. Thus, if one is interested in this T-region, one assumes that N_0 is low. At low T , outside the TQ region, the sample is insensitive to positive charge, i.e. high N_0 . This argument implies that SC is present in the sample at low T , but does not affect significantly the transport properties, in agreement to our discussion of §5.2.3. The same argument holds under combined bandgap and Infra-Red (IR) illumination. IR light makes the sample insensitive to SC, as discussed in §5.1.2, thus N_0 becomes higher and the effect of SC is very weak, in agreement to the potential profile measurement of fig.5.9.

One surprising experimental observation was that the photocarrier generation rate has very little effect on non-Ohmic I-V curves, see §5.3.1. A nice feature of the model is that its results do not depend on G .

We conclude that this simple model provides some insight on the relation of the sensitivity of the sample to positive charge, with the width of the SC region and its effect on the potential across the sample. An important feature of the problem of non-Ohmicity in a-Si:H not incorporated in this model is the following. As already discussed, an onset of band bending causes SC creation near the cathode. This onset is

assumed to exist in our model, because we start the calculation with a certain nonzero $N^+(0)$. However, the experimental situation may be that at low voltages there is no bending to initiate SC creation. This may explain why I-V curves calculated with our model show gradual deviation of photocurrent from Ohmicity, and do not show the sharp transition to non-Ohmic photocurrent at a certain voltage observed in experiment. This is demonstrated in Fig. 5.20, where we compare an experimental I-V curve under uniform illumination, with a curve calculated with the model.

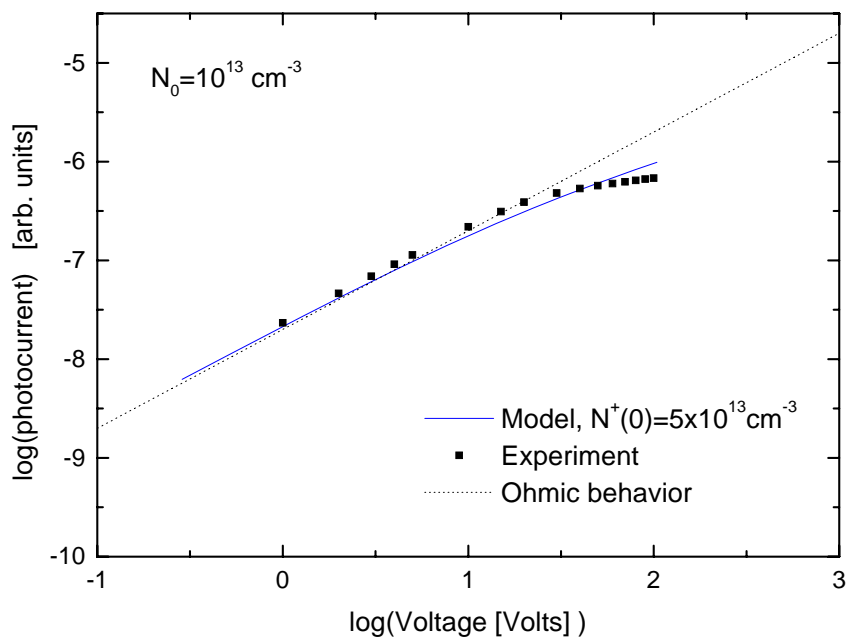


Figure 5.20. Calculated I-V curve (solid line), as compared to an experimental one (squares). The dotted line indicates Ohmic behavior.

The results of our simple model allow one to deduce some simple relations which govern the non-Ohmic effects in photoconducting a-Si:H. One can see in Figs. 5.16 and 5.19 that the SC density $N^+(x)$ is roughly constant from $x=0$ to $x=d$, and drops to zero for $x>d$, where d denotes the width of the SC region. Thus, we simplify the problem by assuming that there is a SC region with constant charge density $N^+ \approx N^+(0)$

for $0 < x < d$, and zero charge density for $x > d$. We denote the photoconductivity near the cathode as σ_C and that in charge-free region (bulk) as σ_B . At low T, σ_C corresponds to σ_h of eq.(5.2) and σ_B corresponds to σ_e of eq.(5.2). Current continuity requires, similar to eq.(5.2), that

$$\sigma_C E_C = \sigma_B E_B, \quad (5.7)$$

where E_C is the electric field at the cathode, and E_B that in the bulk. We thus have

$$\frac{\sigma_B}{\sigma_C} = \frac{E_C}{E_B}. \quad (5.8)$$

Having assumed that the SC density is constant one can write the total space charge

Q_{tot} per unit area S as

$$\frac{Q_{tot}}{S} = d \cdot q_e N^+(0) \quad (5.9),$$

which by Gauss's law, eq.(5.4), is equal to $\epsilon_s (E_C - E_B)$. One thus has for the width of the SC region:

$$d = \frac{\epsilon_s E_B \left(\frac{E_C}{E_B} - 1 \right)}{q_e N^+(0)} \quad (5.10).$$

Our assumption of the sensitivity of photoconductivity to SC reads

$$\frac{d \ln \sigma}{d N^+} = -\frac{1}{N_0} \quad \text{from which one has} \quad \frac{\ln \left(\frac{\sigma_B}{\sigma_C} \right)}{N^+(0)} = \frac{1}{N_0}. \quad \text{With the use of (5.8), the last}$$

equation becomes

$$\ln \left(\frac{E_C}{E_B} \right) = \frac{N^+(0)}{N_0} \quad (5.11).$$

The photoconductivity in the cathode region is lower by more than two orders of magnitude than that of the bulk, i.e. from eq.(5.8), the field at the cathode is higher much higher than that in the bulk. In this sense, one can simplify eq.(5.10) to

$$d \approx \frac{\varepsilon_s E_B}{q_e} \frac{E_C / E_B}{N_0 \ln\left(\frac{E_C}{E_B}\right)}. \quad (5.12)$$

From eq.(5.12), one can see that small N_0 and large ratio E_C/E_B , i.e. large $N^+(0)/N_0$ from eq.(5.11), give large d , in agreement to our calculations.

In similar manner, one can also calculate the onset voltage V_{ON} of non-Ohmicity. If we call V to total potential difference across a sample of length L , we have approximately

$$V = E_C d + (L - d)E_B = LE_B \left(1 + \frac{d E_C}{L E_B}\right). \quad (5.13)$$

The photocurrent I is equal to

$$I = \sigma_B \frac{V}{L} \frac{1}{\left(1 + \frac{d E_C}{L E_B}\right)} \quad (5.14).$$

The deviation from Ohmicity in (5.14) is included in the dependence of the SC width d on the applied voltage. If one defines V_{ON} as the voltage for which $\frac{d E_C}{L E_B} = 1$, we get

from (5.12)

$$V_{ON} = \frac{L^2 q_e N_0 \ln\left(\frac{E_C}{E_B}\right)}{\varepsilon_s \left(\frac{E_C}{E_B}\right)^2}. \quad (5.15)$$

Equation (5.15) agrees with our numerical calculations. From (5.15) one can see once more that V_{ON} is low, i.e. non-Ohmicity appears at small voltages, when N_0 is small, and when E_C/E_B is large.

The main features of non-Ohmic effects can now be understood in terms of eqs.(5.12) and (5.15). At low-T, the ratio σ_B/σ_c is small, of the order of 10 or less, i.e from (5.8) E_c/E_B is small. N_0 is large, because the photoconductivity is insensitive to positive charge. Thus, at low T the width d is very small, and the sample is Ohmic.

In the temperature region of thermal quenching (TQ) , σ_B/σ_c becomes larger, because σ_c does not change very much with T, while σ_B rises rapidly with T and is maximum in the temperature of TQ. Furthermore, N_0 is now smaller, because the sample is very sensitive to positive charge in this T-region. Thus, d becomes large, and V_{ON} small, and non-Ohmic effects appear.

In the dark, thermionic emission from the metal contacts is able to provide the very small current drawn by the semiconductor. In this case there is no space charge because there is no band bending near the contacts.

Appendix A. Sample characteristics

The a-Si:H samples used in this study were deposited on Corning-7059 glass substrates, by Plasma-Assisted CVD. Sample deposition was done in the University of Chicago. Sample thickness was around 1 μ m for all samples. Table I summarizes the characteristics of the samples.

The gas phase concentration of both PH₃ and B₂H₆ is given in the Table for compensated samples, and the concentration of B₂H₆ for the p-type sample.

Metal electrodes were deposited in the free surface of the semiconductor, for conductivity measurements. The metals used were NiCr and Cr. The spacing between metal contacts in this coplanar geometry was 0.2mm or 2mm.

Sample	Doping	Native defect density (cm ⁻³)	Contact metal/ spacing (mm)
i1	undoped	5x10 ¹⁵	NiCr / 0.2
i2	undoped	10 ¹⁶	NiCr / 0.2
c-20	compensated 20ppm	5x10 ¹⁵	NiCr / 0.2
c-100	compensated 100ppm	10 ¹⁶	NiCr / 0.2
p-20	p-type, 20-ppm	2.5x10 ¹⁶	NiCr / 0.2
#1 (Chapter 5)	undoped	5x10 ¹⁵	NiCr / 2mm
#2 (Chapter 5)	undoped	5x10 ¹⁵	Cr / 0.2mm

Table I: Sample characteristics.

Appendix B. Photoconductivity during 30ns pulses: measurement set-up.

In Chapter 4 we presented measurements of photoconductivity under the laser pulse, in nanosecond time scale. A basic constraint which must be fulfilled in order to have the frequency response needed for such a measurement is that a 50Ω line must be used all the way from the sample to the Digital Storage Oscilloscope (DSO).

The photocurrent of a-Si:H under the laser pulse was sufficiently high that one could use the simple set-up, demonstrated in Fig.B1. This does not contain any amplification, but is simply a 50Ω line from the cryostat in which the sample is mounted, to the DSO.

In order to be able to measure the photocurrent under attenuated laser pulse, reduction of the interference noise picked up by the sample holder was needed. This was achieved by mounting the sample in a smaller sample holder, which was shielded with a metallic box in such a way that the laser beam could still illuminate the sample. The small size of the sample holder and the shielding, reduce the action of the wires as antennas which pick-up electromagnetic noise. The shielding is demonstrated schematically in Fig.B.1 by the dashed rectangle around the sample holder.

The bias voltage V_b was 100V. We ensured that the photocurrent under the laser pulse was Ohmic at this voltage. The capacitor C was used in order to keep the bias voltage constant during the 30ns of large current flow through the sample.

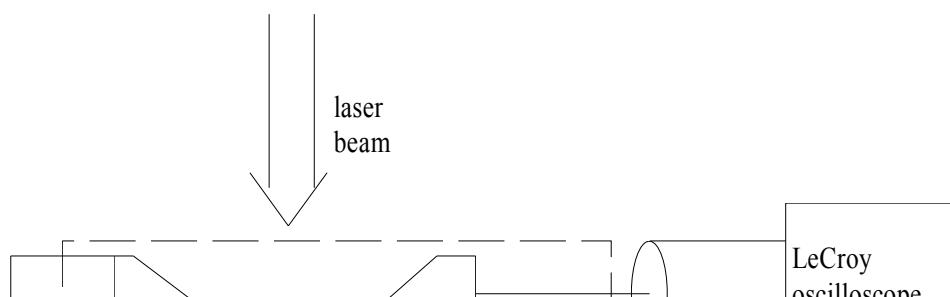


Figure B.1. Set-up for photoconductivity measurements under the laser pulse. The dashed rectangle represents the shielded part of the set-up.

Appendix C. Potential profile measurement set-up

Under steady state photoconductivity conditions a constant potential difference is applied between the metal contacts. Thus there is a variation of the potential V in the direction x of photocurrent flow in the sample, the total potential difference throughout the sample being the voltage applied on the contacts.

The form of the function $V(x)$ depends on the existence of space charge in the sample. The simplest case is a linear variation of V with x in the absence of space charge.

We developed an experimental set-up in order to actually measure this potential profile across the sample. Figure C.1 demonstrates the idea.

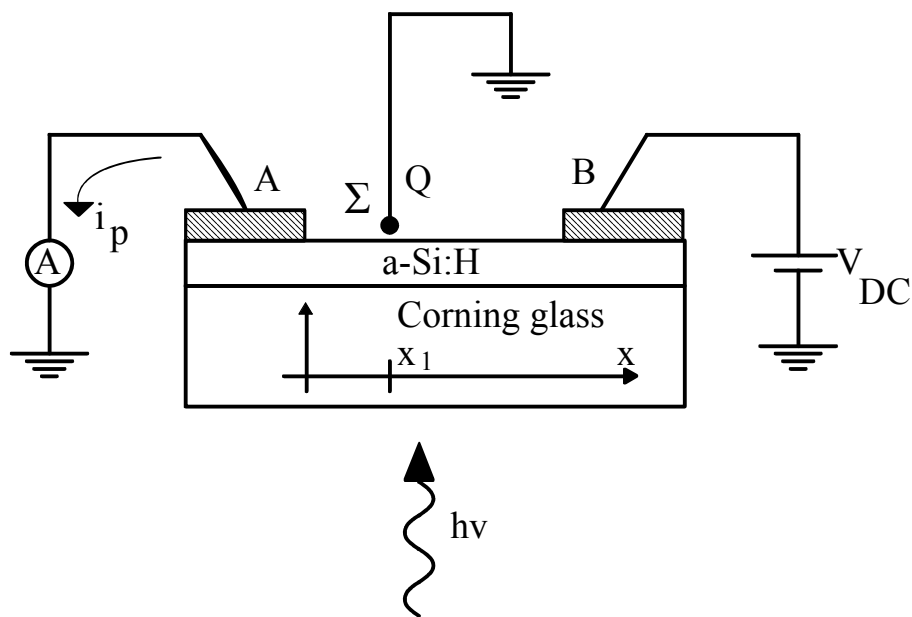


Figure C.1: Schematic of the potential profile measurement principle. Direction x is that of photocurrent (i_p) flow. Metal contacts are labelled A and B.

The sample is illuminated from the back in a simple steady state photoconductivity set-up. The metal contacts are labelled A and B, and the direction x of photocurrent

flow is shown. A potential profile $V(x)$ is established in the sample. To this set-up we add a thin wire (labelled Σ) stretched on top of the sample, perpendicular to the x -direction. A small strip of the sample around $x=x_1$ (see Fig.C.1) and the wire, form a capacitor. The charge induced on the wire is $Q=CV(x_1)$, $V(x_1)$ being the potential of the sample at $x=x_1$. The potential in the sample is of course measured having as reference the potential at the grounded contact A. Assuming that the capacitance C does not change when the wire moves along x , one can measure Q in each wire position and deduce $V(x)$ from x_A to x_B .

Taking advantage of the very high accuracy of lock-in detection methods, we improve the above idea as follows. We add to the constant voltage V_{DC} a small sinusoidally varying voltage $V_{AC}=V_0\sin\omega t$. V_{AC} is a time modulation of the potential profile established by the higher V_{DC} in the sample, allowing us to measure the current i_Σ through the wire at frequency ω with a lock-in amplifier. The amplitude of i_Σ is proportional to the amplitude of the time modulation induced by V_{AC} . If, for example, $V(x)$ is linear then the current i_Σ measured at arbitrary x_1 will depend linearly on x_1 , as shown in Fig.C.2. If on the other hand one measures a nonlinear dependence of i_Σ on x this implies nonlinear $V(x)$. The spatial resolution of this measurement is limited by the thickness of the probing wire, which was 0.15mm, allowing us to measure roughly 10 different wire positions in a sample with 2mm electrode spacing.

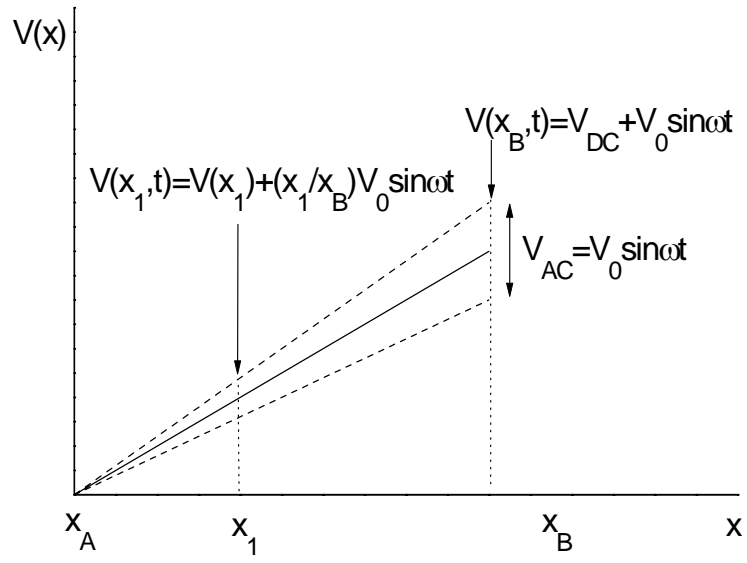


Figure C.2: Time modulation of linear potential profile V . The time dependence of V at arbitrary x_1 is shown.

The actual measurement set-up is shown in Fig.C.3.

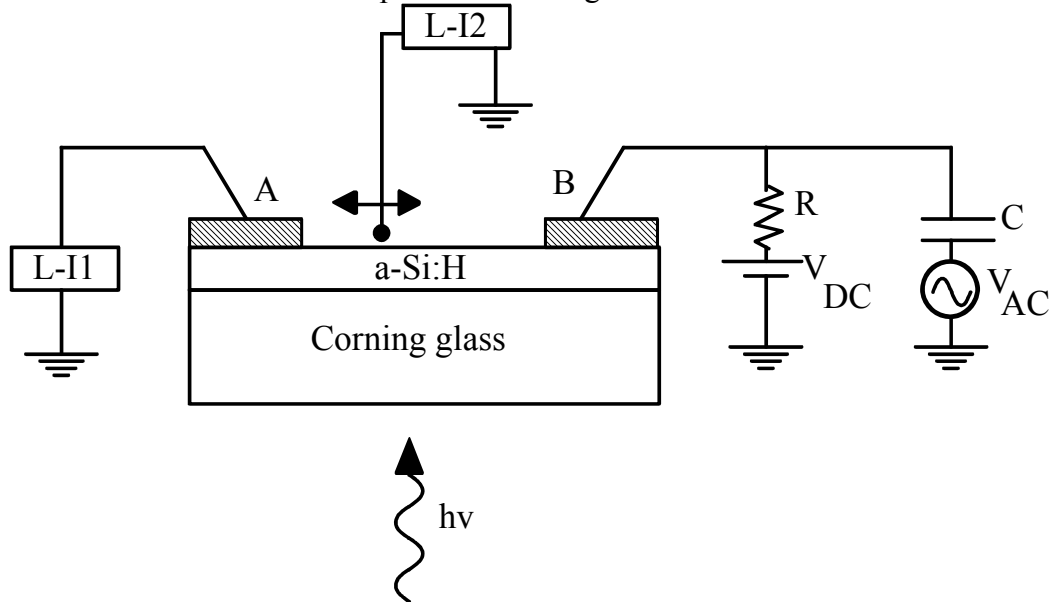


Figure C.3: Potential profile measurement set-up. Lock-In amplifiers are labelled L-I1,2. $R=400 \Omega$, $C=220\text{nF}$.

Care was taken in order to avoid direct leakage of current from the semiconductor to the wire. Furthermore, we confirmed that we measured capacitive coupling between wire and sample by monitoring the phase angle between the applied AC voltage and the current i_{Σ} .

References

- J.C.Phillips, *Phys.Rev.Lett.* **42** (1979), 1151
- S.T.Pantelides, *Phys. Rev. Lett.* **57** (1986), 2979.
- W.E. Spear and P.G.LeComber, *Solid State Commun.* **17** (1975), 1193.
- D.L.Staebler and C.R.Wronski, *Appl. Phys. Lett.* **26** (1977) 292.
- R.A. Street, *J.Non-Cryst.Solids*, **77** (1985) 1.
- H.Fritzsche, *MRS conf. proc.*, Vol. **467** (1997) 19.
- M.Tran, *Phil. Mag.* **B72** (1995) 35.
- A.Rose, "Concepts in Photoconductivity and Allied Problems", 1963, *Interscience publ. NY*.
- P.Stradins, H.Fritzsche and M.Tran, *MRS conf. proc.*, Vol. **377** (1995) 467.
- W. den Boer, M.J. Geerts, M.Ondris, H.M.Wentinick, *J.Non-Cryst.Solids*, **60** (1984) 268.
- H. Pfeleiderer, W. Kusian, W. Kruehler, *Solid State Commun.*, **49** (1984) 493.
- C. Wagner, S. Gangopadhyay, B. Schroeder, J. Geiger, *AIP Conf.Proc.* **157** (1987)46.
- M.Stutzmann, W.B.Jackson and C.C.Tsai, *Phys. Rev.* **B32** (1985), 23.
- T.Kamei, N.Hata, A.Matsuda, T.Uchiyama, S.Amano, K.Tsukamoto, Y.Yoshioka and T.Hirao, *Appl. Phys. Lett.* **68** (1996), 2380.
- H.Branz, *Solid State Commun.* **105** (1998), 387.
- M.Stutzmann, J.Nunnekamp, M.S.Brandt and A.Asano, *Phys. Rev. Lett.* **67** (1991), 2347.
- N.Hata, G.Ganguly, S.Wagner and A.Matsuda, *Appl. Phys. Lett.* **61** (1992), 1817.
- N.Hata, G.Ganguly and A.Matsuda, *Appl. Phys. Lett.* **62** (1993), 1791.
- R.Meudre, S.Vignoli, M.Meudre and L.Chanel, *Phil.Mag.Lett.* **68** (1993), 159.
- P.Stradins and H.Fritzsche, *Phil.Mag.* **B69** (1994), 121.

- P.Stradins and H.Fritzsche, *J.Non-Cryst.Solids* **198-200** (1996), 432.
- P.Tzanetakis, N.Kopidakis and H.Fritzsche, *J.Non-Cryst.Solids* **198-200** (1996), 276.
- P.Tzanetakis, H.Fritzsche, M.Tran, M.Androulidaki and E.Rynes, *J.Non-Cryst.Solids* **164-166** (1993), 607.
- P.Stradins, H.Fritzsche, P.Tzanetakis and N.Kopidakis, *MRS conf. proc.*, Vol. **420** (1996A) 729.
- P.Stradins, H.Fritzsche, N.Kopidakis and P.Tzanetakis, *MRS conf. proc.*, Vol. **420** (1996B) 765.
- P.Persans, *Phil.Mag.* **B46** (1982), 435.
- S.Heck, P.Stradins and H.Fritzsche, *MRS conf. proc.*, Vol. **467** (1997) 251.

Publications from this thesis

1. Light-induced degradation of a-Si:H - A comparison of short-laser-pulse and steady light degradation, P.Tzanetakakis, N.Kopidakis, M.Androulidaki, C.Kalpouzos, P.Stradins, H.Fritzsche, MRS Spring 1995 Conf. Proc.
2. Short-laser-pulse and steady light degradation of intrinsic, p-type and compensated a-Si:H, P.Tzanetakakis, N.Kopidakis, M.Androulidaki, C.Kalpouzos, P.Stradins, H.Fritzsche, J.Non-Cryst.Solids, 198-200 (1996), 458-461.
3. Photoconductivity during 30ns laser pulses in a-Si:H, P. Tzanetakakis, N.Kopidakis, H.Fritzsche, J.Non-Cryst.Solids, 198-200 (1996), 276-279.
4. Comparison of experiment and theory of the photoconductivity of a-Si:H up to a generation rate of $10^{28} \text{ cm}^{-3}\text{s}^{-1}$, P.Stradins, H.Fritzsche, P.Tzanetakakis, N.Kopidakis, MRS Spring 1996 Conf. Proc.
5. Photoconductivity of a-Si:H as a function of doping, temperature and photocarrier generation rates between 10^{13} and $10^{28} \text{ cm}^{-3}\text{s}^{-1}$, P.Stradins, H.Fritzsche, N.Kopidakis, P.Tzanetakakis, MRS Spring 1996 Conf. Proc.
6. Contact limitation of secondary photoconductivity in intrinsic a-Si:H, N.Kopidakis, P.Tzanetakakis, P.Stradins, H.Fritzsche, J.Non-Cryst.Solids (1997), in press.